Complex fluids dripped into a liquid bath : impact, relaxation and gelation dynamics

Julie Godefroid

PSL UNIVERSITÉ PARIS

THÈSE DE DOCTORAT
DE L'UNIVERSITÉ PSL

Préparée à ESPCI Paris

Gouttes de fluides complexes tombant dans un bain liquide: impact, relaxation et gélification

Complex fluids dripped into a liquid bath: impact, relaxation and gelation dynamics

Soutenue par

Julie GODEFROID

Le 13 décembre 2019

École doctorale n°397

Physique et Chimie des Matériaux

Spécialité

Physico-chimie

ESPCI PARIS | PSL

Composition du jury :

Etienne BARTHEL Directeur de recherche, CNRS / ESPCI Paris	*Président du Jury*
Cécile MONTEUX Chargé de recherche, CNRS / ESPCI Paris	*Directrice de thèse*
Laurence RAMOS Directeur de recherche, CNRS / Université de Montpellier	*Rapporteur*
Laurent DAVID Professeur des universités, Université Claude Bernard Lyon 1	*Rapporteur*
Jan VERMANT Professeur, ETH Zurich	*Examinateur*
Nicolas BREMOND Maître de conférences, ESPCI Paris	*Examinateur*

Remerciements

En premier lieu, je remercie Cécile Monteux de m'avoir donné l'opportunité de travailler au laboratoire SIMM en collaboration avec Saint-Gobain et de m'avoir encadrée durant ces trois années. J'ai pu bénéficier de conditions matérielles remarquables pour mener à bien mon projet de recherche.

Je tiens également à remercier chaleureusement Étienne Barthel pour son aide, ses conseils et l'intérêt qu'il a porté à mon sujet. Merci pour ton écoute et ta bienveillance qui m'ont été très précieuses durant ces trois ans. Merci pour le temps que tu m'as consacré, malgré ton agenda très chargé, et ce jusqu'à la fin. J'ai beaucoup apprécié nos discussions sur la "croûte" et le "cœur coulant" de mes billes, qui nous mettaient souvent en appétit, à en croire les chocolats du bureau !

Je remercie grandement David Bouttes, pour son rôle de tout premier plan dans l'encadrement de cette thèse. Merci pour la confiance que tu m'as accordée, ainsi que pour tes idées et tes conseils qui m'ont été très chers. Merci aussi pour toutes nos discussions non scientifiques, autour d'une bière ou de barquettes de frites belges.

Un grand merci à Magali Arnold et Laure Charmasson, qui ont suivi de près tous mes essais à SGR Provence. Merci pour votre disponibilité, votre enthousiasme et votre savoir-faire. C'est avec vous que j'ai commencé à mettre la main à la pâte et vos conseils et remarques m'ont toujours été d'une grande aide. Merci pour tous les bons moments que nous avons passés ensemble, autour d'un chocolat chaud, au restaurant ou même en dégustant d'excellentes tomates du jardin au bord de la piscine. J'ai vraiment apprécié travailler à vos côtés et je n'emporte avec moi que de très bons souvenirs.

Je tiens également à remercier Anne-Laure Beaudonnet pour tous les échanges que nous avons pu avoir durant ma thèse. Merci pour tes questions et remarques pertinentes, qui me tiraient vers le haut. Merci aussi et surtout pour ta gentillesse, tes mots d'encouragement et ton soutien jusqu'au jour J, qui m'ont été très précieux.

Je remercie ensuite Emmanuel Nonnet qui a supervisé les débuts de cette thèse. Merci

pour tous les échanges intéressants que nous avons eus. Je tiens aussi à remercier Jessica Delavoipière qui a suivi avec intérêt mes derniers résultats et qui a participé à plusieurs réunions. Enfin, un grand merci à tous ceux qui m'ont aidé, de près ou de loin, et avec qui j'ai échangé à SGR Provence ou SGR Paris : Marie Lamblet, Keyvan Piroir, Yves Boussant-Roux, Eric Lintingre, Ludivine Colmuto, Romain Cabanero, Nassira Benameur, Claire Duclaux-Roche, Anne Dagon, etc.

J'adresse un grand remerciement à Nicolas Bremond, Laurent David, Laurence Ramos et Jan Vermant qui ont accepté de juger mon travail. Merci pour l'intérêt que vous y avez porté, pour vos remarques, questions, critiques et retours. Merci pour la richesse de la discussion qui a suivi ma présentation et merci d'avoir fait le déplacement le jour J malgré les grèves.

Je remercie chaleureusement Anselmo Soeiro Pereira et Rudy Valette pour les discussions très fructueuses que nous avons eues. Nous avons tout d'abord échangé lors du congrès du GFR et lors des JJR, ce qui nous a ensuite amenés à travailler et réfléchir ensemble sur les problèmes d'impact de gouttes non Newtoniennes. Merci pour votre patience et votre aide dans la compréhension de mon système complexe. Je suis très heureuse d'avoir pu collaborer avec vous, c'était très enrichissant.

Je remercie grandement Michel Cloître du laboratoire MMC pour nos discussions tout au long de ma thèse. Merci pour votre disponibilité et vos conseils avisés. Que ce soit pour répondre à des questions sur la rhéologie des polyélectrolytes ou le gonflement des gels, vous avez toujours pu me consacrer du temps et je vous en suis extrêmement reconnaissante.

Merci également à Annie Colin du laboratoire CBI pour nos échanges très intéressants sur les interactions de déplétion ou de pontage dans les suspensions complexes.

Dans un second temps, j'aimerais prendre le temps de remercier quelques personnes du laboratoire SIMM.

Un immense merci à Alexandre Lantheaume et Ludovic Olanier de l'atelier mécanique, qui ont conçu le bâti de mon montage expérimental de dripping, ainsi que la pièce centrale, qui leur a donné du fil à retordre. Merci pour votre patience, vos conseils et votre pédagogie. J'ai réellement apprécié tous nos échanges, allant du dessin de pièces à la démonstration de leur fabrication. Merci aussi pour toutes les discussions matinales moins sérieuses autour d'un café, d'un thé, ou d'un pitch !

Je tiens également à remercier Bruno Bresson avec qui j'ai passé quelques matinées et après-midis devant le MEB. Merci pour ton expertise, ta patience et ton temps, c'était

toujours super intéressant de discuter avec toi. Merci également pour ta perpétuelle bonne humeur, qui met du baume au cœur tous les jours au labo.

Je remercie très chaleureusement Guylaine Ducouret, avec qui j'ai eu de nombreuses discussions autour de la rhéologie de mes suspensions. Merci pour ton expertise et tes conseils dans la réalisation des tests et l'analyse des résultats. Je te remercie aussi pour ta bienveillance et ta générosité.

J'adresse un grand merci à Alba Marcellan, qui m'a initié à la mécanique des gels. Merci pour ton aide dans la réalisation de la cuve et du mobile pour les tests de compression de billes immergées.

Un grand merci à toutes les personnes avec qui j'ai eu des échanges très enrichissants au cours de ces trois ans de thèse et qui m'ont aidée de près ou de loin : Nicolas Sanson, Dominique Hourdet, Patrick Perrin, Nadège Pantoustier, François Lequeux, Mohammed Hanafi, Armand Hakopian.

Je tiens à remercier mes trois stagiaires, Sandrine, Charlotte et Sihem qui ont travaillé avec moi. Merci pour votre motivation, votre bonne humeur et votre travail.

Un immense merci à mes co-bureaux de E005 : Paul, Louis et Pierre rejoints ensuite par Yuan-yuan et Malak. Cette thèse n'aurait pas été la même sans vous. Nos "vendredis gourmandie", nos discussions sur tout et rien, en particulier sur Aya Nakamura ou autres goûts musicaux douteux, nos fist-bumps, ainsi que vos blagues (drôles ou pas) et votre bonne humeur vont me manquer. Je n'aurais pas pu rêver d'un meilleur bureau (si ce n'est pour son odeur). Un merci tout particulier à Paul, mon Bibi et voisin de bureau, pour son aide précieuse et pour qui Matlab n'a aucun secret.

Je remercie aussi la E001, deuxième bureau du sous-sol de l'escalier C, Claire, Sandrine, Julien et Clément avec qui je partageais plein de bons moments en particulier aux pauses déjeuner. Nos discussions sur l'épluchage de pommes, les chansons des années 50 à 80 ou encore les chaussettes dépareillées faisaient de l'escalier C The Place To Be. Merci également à la G007, Christophe, Wilbert, Mickaël, Anaïs, Anh et Soufiane qui partageaient nos pauses déjeuner.

Un peu plus loin, je remercie également les non-permanents de l'escalier H, Ludovic, Juliette, Miléna, Xavier, Pascal, Franz, Nassim, Clotilde, Gaetan, Mehdi, Francisco, Heiva, Gabo, Lola, Julie... Pour certains, on se voyait moins souvent mais on a pu partager de bons moments lors des divers weekends labo, des beer/wine tasting, des soirées jeux ou encore des sorties à La Montagne ou au Confess' tous ensemble. Malgré notre grand nombre, il y a toujours eu une grande entente et un très bel esprit de groupe

et cela va réellement me manquer.

Cette thèse a surtout été pour moi de très belles rencontres. Merci aux filles #triathlètes, Jennifer, Mélanie, Raphaëlle, Valentine, Gaëlle et Claire pour votre amitié et votre soutien à toute épreuve. Merci pour les goûters Carl Marletti, les soirées jeux avec Docteur Pilule et vos talents de mimes, les weekends repos ou sportifs et les séances de piscine / yoga / hiit. On s'est bien amusées. Merci d'avoir été mes compagnons de route durant ces trois années, pour les bons moments mais aussi les plus difficiles et je ne doute pas que de prochaines aventures nous lieront dans le futur.

C'est la fin de ces 3 ans de thèse mais aussi la fin d'une grande aventure de 7 ans à l'ESPCI Paris. Une page se tourne mais je tiens à remercier tous mes professeurs, mes encadrants de stages ainsi que mes amis PCéens et ma famille PCéenne qui m'ont accompagnée dans cette formidable épopée.

Merci à tous mes amis qui ont suivi cette aventure de près ou de loin, Anne-Charlotte, Roxane, Gregoire, Anthony, Alexandra, Florence, Delphine, Steven... Merci d'avoir été quasiment tous présents le jour J.

Un immense merci à Julien, ma force tranquille. Merci pour ton soutien quotidien, ta confiance en moi et ton calme notamment pour la dernière ligne droite et la gestion du pot de thèse ! Merci pour les surprises, les rires, les découvertes des mille saveurs de Paris et nos aventures ici et ailleurs qui ont ponctué ces années de thèse. Merci pour tout l'amour que tu me donnes. J'ai beaucoup de chance de t'avoir.

Enfin je tiens à remercier ma famille, Thomas, Pauline, mes parents, tonton Sylvain, Maman Anne, Mamy et Pépé qui m'ont épaulée durant ces 9 dernières années. Je suis tellement heureuse que vous ayez pu être présents pour ce grand jour si important. Un immense merci à mes parents pour leur soutien et leur amour inconditionnel. Vous étiez toujours à des milliers de kilomètres mais vous avez toujours su être là pour moi et me re-booster dans les moments difficiles. Je vous aime. Merci à Pépé et Mamy qui m'ont accueillie plusieurs fois à Blankenberge pendant mes années de prépa et qui ont cru en moi. Merci pour les pauses café chez Loulou, les bons petits plats, les balades sur la digue, les magnifiques dessins et les blagues qui ponctuaient mes journées. Tous ces moments passés avec vous font partie de ma réussite et sont gravés à jamais dans ma mémoire. Pépé, toi qui m'avais convaincue d'aller à l'ESPCI pour suivre les traces de Marie Curie, tu n'as malheureusement pas pu être là pour célébrer l'aboutissement de mes études et l'obtention de mon doctorat, mais je suis certaine que tu aurais été fier de moi. C'est donc avec émotion que je te dédie mes travaux de thèse.

À Pépé,

"pour la Recherche du Bonheur"

Contents

Résumé en Français

Les billes de céramique sont utilisées dans de nombreux domaines et pour des applications diverses (support de catalyse, roulement à bille, charge minérale pour améliorer les propriétés mécaniques de certains matériaux, etc) et peuvent être fabriquées par différentes techniques (granulation, moulage, drip casting). Saint-Gobain cherche à produire des billes monodisperses et sphériques, c'est pourquoi le drip casting (technologie d'encapsulation par l'alginate) est apparu comme un procédé de choix.

Le processus d'encapsulation consiste à emprisonner une ou plusieurs substances au sein d'un matériau enrobant semi-perméable, donnant naissance à une bille ou une capsule. Depuis les années 1930, ces objets ont connu un essor important dans de nombreux domaines (pharmaceutique, cosmétique, textile, agroalimentaire, biologie). Il existe un grand nombre de polymères adaptés à l'encapsulation, mais l'alginate représente un candidat idéal pour toutes les applications citées ci-dessus. En effet, c'est un polysaccharide naturel et biocompatible particulièrement abondant dans les algues brunes marines. C'est un copolymère à blocs composé de deux monomères: le β-D-mannuronate (bloc M) et le α-L-guluronate (bloc G). De par la présence de groupements carboxylates - COO^-, l'alginate est un polyélectrolyte capable de former un gel physique en présence d'ions divalents tels que les ions Ca^{2+}. Deux blocs G de chaînes polymères différentes peuvent s'associer par interactions électrostatiques entre les groupements carboxylates du polymère et les cations Ca^{2+}.

Lors du procédé de drip casting, une goutte de solution d'alginate tombe dans un bain contenant des ions calcium et commence aussitôt à gélifier, permettant ainsi d'encapsuler la/les substance(s) présente(s) initialement dans la solution. La Figure 0.1 illustre ce procédé de dripping. De nombreux articles étudient empiriquement l'influence de la composition de la solution et de certains paramètres d'expérience sur la forme finale des billes d'alginate. En revanche, les dynamiques d'impact et de relaxation pour ces systèmes ne sont, à notre connaissance, pas étudiées dans la littérature. De fait, lorsque

la goutte rencontre le bain, elle s'étale puis relaxe sa forme tout en se solidifiant.

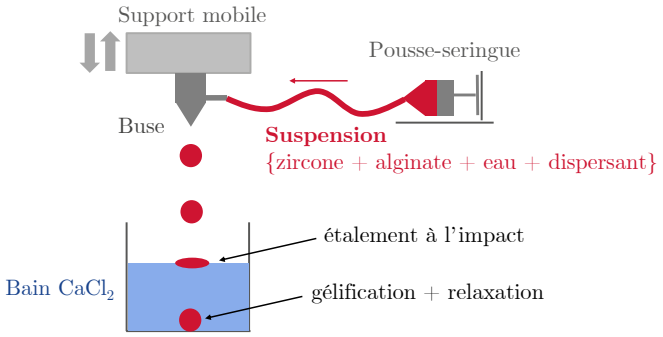

Figure 0.1 *Procédé de dripping.*

Pour produire des billes de céramique, il faut ajouter des particules à la solution initiale de dripping, ce qui complique davantage le système. L'objectif de cette thèse est de déterminer et de comprendre les mécanismes intervenant tout au long du procédé (depuis la formation des gouttes jusqu'à l'obtention d'une bille totalement gélifiée), afin de contrôler la forme finale des billes. Pour ce faire, nous avons étudié séparément les comportements des gouttes à l'impact et pendant la relaxation afin d'identifier les paramètres influençant l'évolution de la forme des capsules.

La caractérisation rhéologique de ces suspensions est cruciale car tout au long du procédé, la suspension est sollicitée de différentes manières. D'abord, elle est cisaillée lors de son passage à travers une fine buse pour former une goutte, puis cette goutte relaxe lors de sa chute dans l'air. Ensuite, au moment de l'impact, celle-ci se déforme et subit à nouveau des taux de cisaillement élevés. Enfin, pour finir, après avoir traversé l'interface, le cœur de la capsule se retrouve au repos.

Tout d'abord, en rajoutant des particules de céramique (zircone ici) dans la solution d'alginate, nous changeons ses propriétés rhéologiques. En effet, la solution d'alginate seule est un fluide Newtonien alors que la suspension contenant de la zircone montre un comportement rhéofluidifiant : sa viscosité diminue fortement avec le taux de déformation imposé (voir Figure 0.2). De plus la suspension présente un seuil d'écoulement σ_0 qui peut être caractérisé par le modèle de Herschel-Bulkley : $\sigma = \sigma_0 + K\dot{\gamma}^m$ (où σ désigne la contrainte et $\dot{\gamma}$ le taux de cisaillement). En augmentant la concentration d'alginate dans la suspension, celle-ci devient plus visqueuse et possède un seuil de plus en plus important. Nous pouvons également changer la taille des chaînes d'alginate en leur imposant un traitement thermique, ce qui permet de passer d'une masse molaire d'environ 250 kg/mol à 60 kg/mol. Dans ce cas, le comportement rhéologique de la

suspension est radicalement différent et devient newtonien. Nous étudions quatre compositions principales dont les propriétés sont inscrites dans le Tableau 0.1 et les courbes d'écoulement représentées dans la Figure 0.3. En résumé, **les supensions A, B et C sont des fluides à seuil alors que la suspension D a un comportement quasi-newtonien**. Dans le premier cas, le seuil vient du fait que les particules de zircone s'agglomèrent pour former un gel colloïdal à cause d'interactions de déplétion lorsque les longues chaînes d'alginate sont ajoutées. Dans le deuxième cas, le comportement newtonien apparaît au bout de 48 heures de repos. Une explication possible pour ce changement de comportement est que les petites chaînes d'alginate prennent place dans un équilibre d'adsorption/désorption avec le dispersant (un acide polyacrylique, PAA). Ainsi, au lieu de s'agglomérer, les particules de zircone se retrouvent protégées par l'alginate et donc bien dispersées dans la matrice enchevêtrée d'alginate.

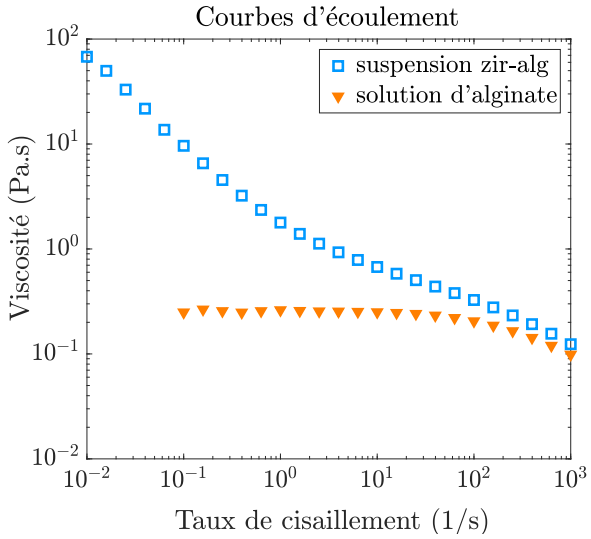

Figure 0.2 *Comparaison des courbes d'écoulement d'une solution d'alginate (à 13.1 g/L) et d'une suspension zircone-alginate (suspension A: 40%m de zircone et 13.1 g/L d'alginate).*

Une fois formulées, les suspensions sont introduites dans le procédé de dripping afin de former des billes de gel alginate-zircone. Nous avons tout d'abord analysé leur comportement à l'impact. Pour cela, nous visualisons à l'aide d'une caméra rapide l'entrée de la goutte dans le bain (voir Figure 0.4). L'analyse des images nous permet par la suite d'obtenir la dynamique d'évolution du diamètre horizontal D de la goutte tout au long de l'impact et d'extraire la déformation maximale D_{max}/D_0. Dans la littérature, cette grandeur est la plus couramment utilisée pour décrire l'impact de gouttes sur des

Suspension	Alginate M_w (en kg/mol)	[Alginate] dans la susp. (en %m)	[Alginate] dans phase aq. (en g/L)	[Zircone] dans la susp. (en %m)
A	250	0.8	13.1	40
B	250	0.4	6.6	40
C	250	1.6	26.2	40
D	60	5	82.0	40

Table 0.1 *Tableau récapitulatif de la composition des 4 suspensions principales étudiées.*

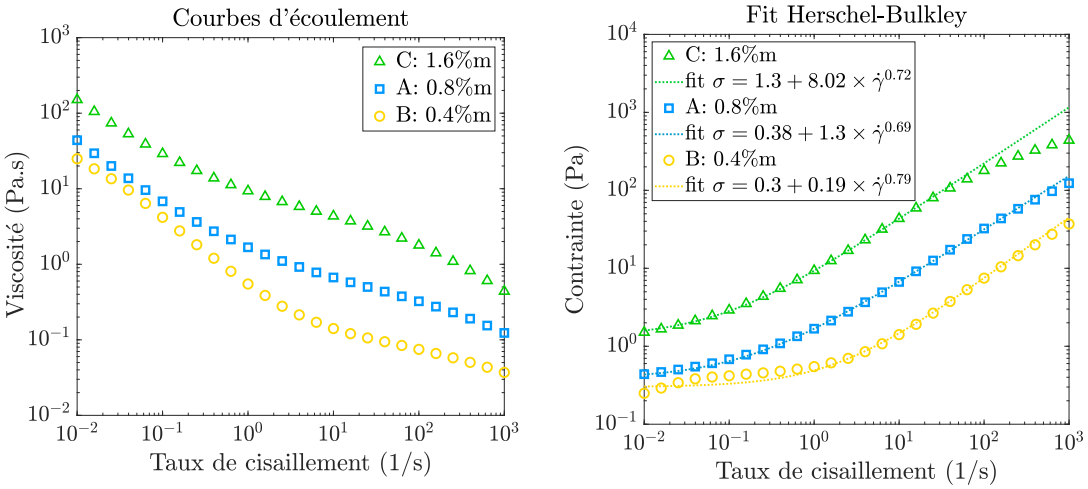

(a) (b)

Figure 0.3 *Courbes d'écoulement des 4 principales suspensions étudiées dans ce manuscrit. (a) Viscosité en fonction du taux de cisaillement. (b) Contrainte en fonction du taux de cisaillement et modèles de Herschel-Bulkley associés* $\sigma = \sigma_0 + K\dot{\gamma}^m$ *aux trois fluides à seuil.*

surfaces solides ou liquides.

Plusieurs paramètres influencent l'étalement de la goutte à l'impact. Le plus évident est la **vitesse d'impact**. Plus celle-ci est grande, plus la goutte s'étale d'après la Figure 0.5. En effet, au moment de l'impact, l'énergie cinétique de la goutte se transforme en énergie de surface et s'accompagne de pertes visqueuses. Plus l'énergie cinétique initiale est importante, plus la goutte s'étale et ce phénomène est accentué pour les suspensions rhéofluidifiantes qui voient leur viscosité baisser dû au cisaillement élevé appliqué à l'impact. La Figure 0.5 montre également que la déformation maximale dépend de la suspension étudiée, et donc de leurs **propriétés rhéologiques**. D'après la littérature, l'impact de gouttes liquides newtoniennes sur une surface solide peut être séparé en deux régimes : inertiel et visqueux. Dans le premier régime, l'énergie cinétique

s'équilibre avec l'énergie de surface pour aboutir à la loi de proportionnalité $D_{\max}/D_0 \propto We^{1/4}$ où le nombre de Weber (We) désigne le rapport entre les forces inertielles et surfaciques. Dans le deuxième régime, le bilan énergétique s'établit entre l'énergie cinétique et les dissipations visqueuses pour donner la loi $D_{\max}/D_0 \propto Re^{1/5}$ où le nombre de Reynolds (Re) décrit le rapport entre les forces inertielles et visqueuses. Pour des fluides non-newtoniens ayant une viscosité non négligeable, on utilise la dernière équation en définissant un nombre de Reynolds généralisé $Re_m = \frac{\rho U_0^{2-m} D_0^m}{K}$ obtenu en considérant la viscosité obtenue par le modèle de Herschel-Bulkley $\eta = K\dot{\gamma}^{m-1}$, à un taux de cisaillement effectif $\dot{\gamma} \sim U_0/h$ (où U_0 est la vitesse d'impact, et h la hauteur de la goutte après son étalement maximal). La déformation maximale est alors prédite par la loi $D_{\max}/D_0 \propto Re_m^{\frac{1}{2m+3}}$. Nous appliquons cette loi à notre cas de figure pour les suspensions A, B et C rhéofluidifiantes ainsi que la loi $D_{\max}/D_0 \propto Re^{1/5}$ pour les fluides newtoniens comme la suspension D et les solutions d'alginate sans particules. Nous pouvons alors rassembler l'ensemble de nos données d'expériences sur un seul graphique représenté dans la Figure 0.6. On y retrouve l'impact de gouttes de tailles différentes dans des bains de calcium de concentrations différentes, avec diverses vitesses d'impact pour toutes les suspensions/solutions étudiées ainsi que les impacts de gouttes sur une surface solide en PMMA (polyméthacrylate de méthyle). Ce graphique montre que l'on peut déduire l'étalement maximal des gouttes à partir de leurs propriétés rhéologiques. De plus, il est possible de prédire le comportement des gouttes à l'impact avec un bain de calcium en observant leur comportement à l'impact sur un solide, ce qui est pratique d'un point de vue industriel.

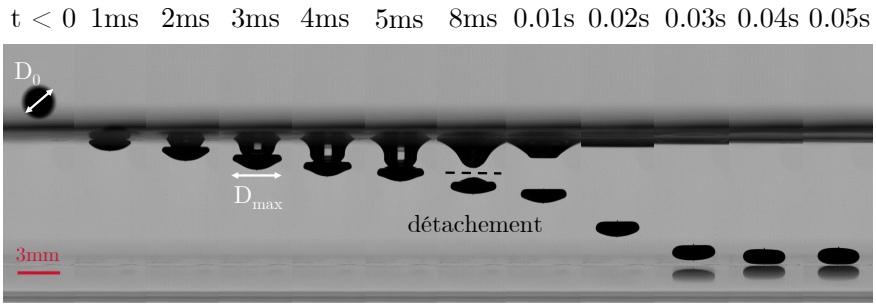

Figure 0.4 *Séquence d'images : goutte de suspension A impactant un bain de calcium de concentration 158 g/L à une vitesse d'impact 1.4 m/s.*

Après l'étape d'étalement à l'impact, nous observons une phase de relaxation. Ce phénomène est bien connu dans la littérature pour le cas d'impacts de gouttes sur une

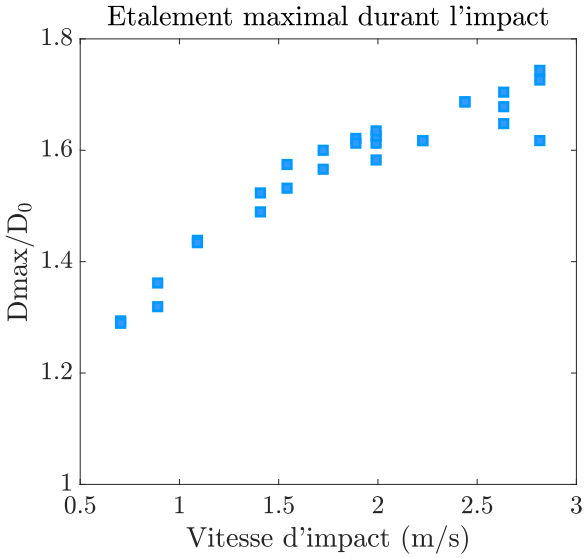

Figure 0.5 *Evolution de la déformation maximale D_{max}/D_0 en fonction de la vitesse d'impact pour une goutte de suspension A ([alginate] = 0.8%m).*

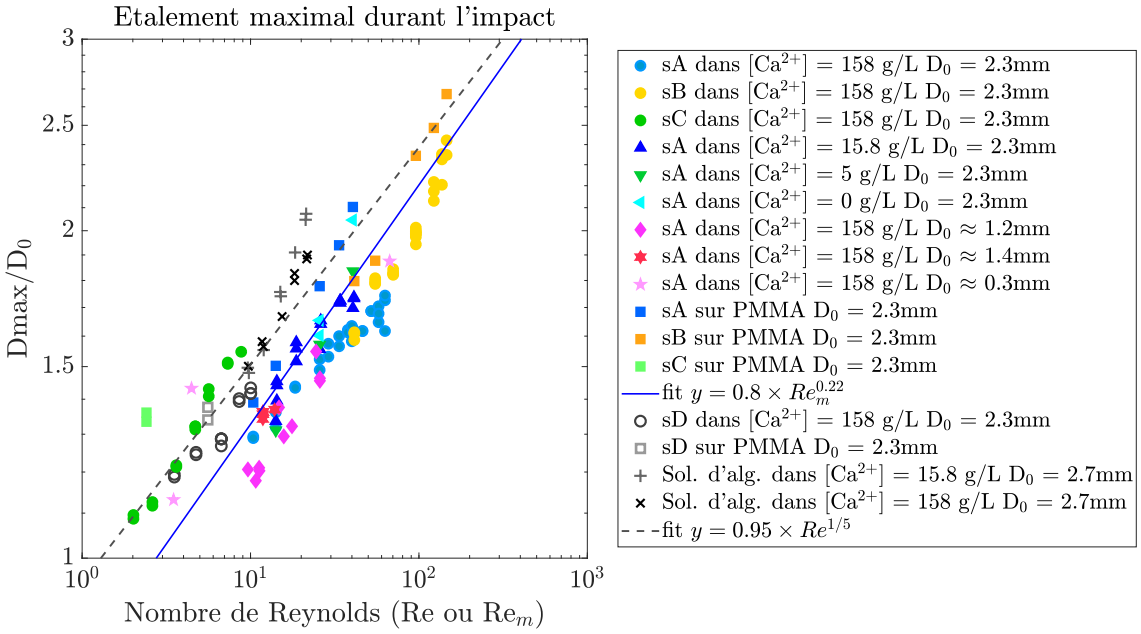

Figure 0.6 *Déformation maximale à l'impact (D_{max}/D_0) en fonction du nombre de Reynolds (Re_m pour les fluides à seuil ou Re pour les fluides newtoniens).*

surface solide ou pour la déformation de gouttes dans un fluide non miscible. Dans les deux cas, la tension de surface, ainsi que le gradient de courbure à l'interface de la goutte sont responsables de la relaxation de la goutte vers une forme sphérique. En général, pour une goutte liquide immergée dans un autre liquide, cette rétraction suit une loi exponentielle avec un temps caractéristique proportionnel au temps capillaire τ_{cap} dépendant du rapport des viscosités de la goutte et du fluide, de la taille de la goutte et de sa tension de surface. Dans notre cas, la tension de surface entre la goutte et le bain est négligeable. Ceci est visible sur la Figure 0.7 (a) où nous observons que lorsqu'il n'y a pas de calcium dans le bain, la goutte ne relaxe pas et finit par se dissoudre. A l'inverse, quand on met la goutte en présence d'ions calcium, celle-ci relaxe vers une forme plus sphérique, et cette rétraction est d'autant plus rapide que la concentration en Ca^{2+} est élevée (Figures 0.7 (b) à (e)). Nous pouvons donc conclure que la relaxation des gouttes n'est pas dictée par la tension de surface et qu'elle est étroitement liée à la quantité d'ions calcium Ca^{2+} dans le bain.

Pour comprendre ce phénomène de relaxation, il faut s'intéresser plus précisément au mécanisme de gélification de l'alginate. Expérimentalement, nous avons mis en évidence que la gélification des gouttes s'accompagne d'un phénomène connu sous le nom de **synérèse** désignant l'expulsion de solvant (l'eau ici) par le gel en formation. Ce processus a été identifié dans plusieurs systèmes agroalimentaires mais n'a pas, à notre connaissance, été étudié en profondeur de manière quantitative. Dans ce travail, nous avons montré par analyse d'images et par suivi de masse au cours du temps que les capsules gélifient tout en perdant de l'eau (i.e. en diminuant de volume). Plus précisément, à l'échelle microscopique, lorsque les chaînes d'alginate sont en contact avec des ions divalents, ceux-ci réticulent aussitôt les chaînes qu'ils rencontrent. Ensuite, les chaînes réticulées se rassemblent du fait de leur affinité préférentielle, ce qui provoque l'expulsion de l'eau de la membrane de gel en formation. Ainsi, lorsqu'une goutte de suspension arrive dans le bain, elle se déforme et commence à gélifier. Une membrane de gel se forme tout autour de la goutte. Cette membrane expulse de l'eau par synérèse et diminue donc de volume alors que le cœur liquide peut être considéré comme incompressible. Par conséquent, toute la membrane se retrouve en tension. Cette **tension d'origine élastique** a le même effet qu'une tension de surface : elle cherche à diminuer le gradient de courbure à l'interface de la goutte en la rendant plus sphérique. La capsule relaxe donc pour passer d'une ellipse déformée à un sphéroïde (voir le dessin explicatif de la Figure 0.8).

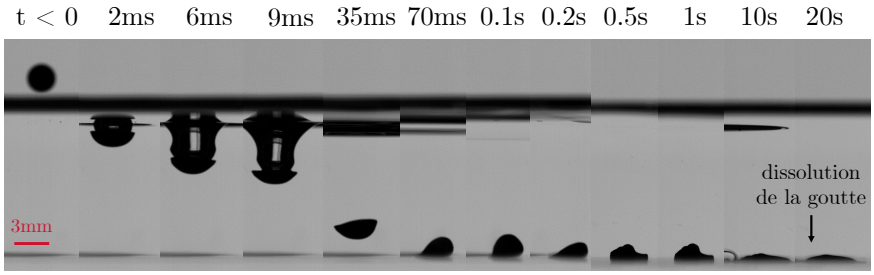

(a) *[$CaCl_2$] = 0 g/L.*

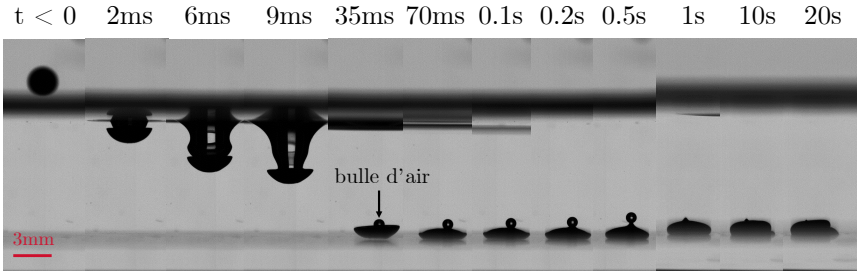

(b) *[$CaCl_2$] = 1.58 g/L.*

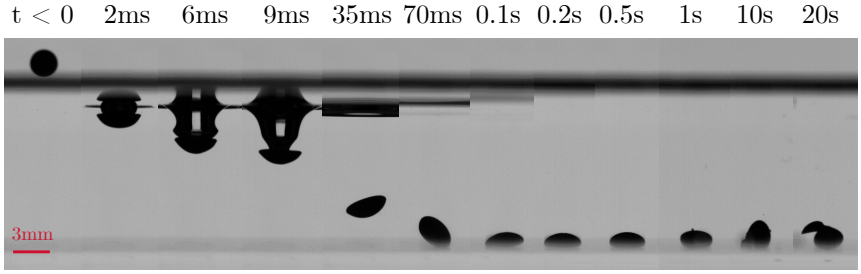

(c) *[$CaCl_2$] = 5 g/L.*

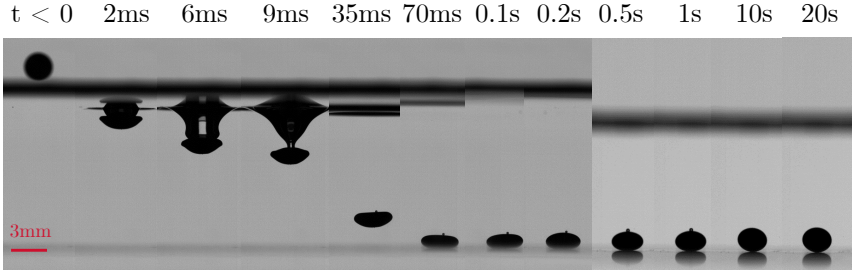

(d) *[$CaCl_2$] = 15.8 g/L.*

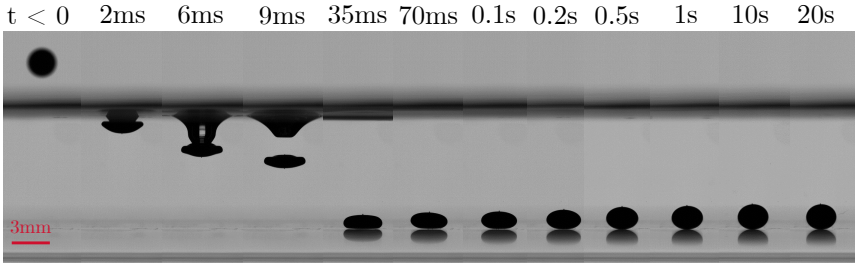

(e) *[$CaCl_2$] = 158 g/L.*

Figure 0.7 *Séquence d'images d'une goutte de suspension A (0.8%m d'alginate) impactant des bains de calcium de concentrations différentes à v = 1.4 m/s.*

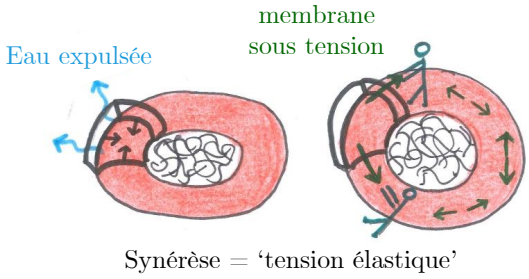

Figure 0.8 *Dessin expliquant le phénomène de synérèse sur une goutte en train de gélifier.*

Nous filmons par caméra rapide la relaxation de la capsule sur une vingtaine de secondes. Ensuite, par analyse d'images nous pouvons tracer l'évolution du rapport d'aspect (AR = grand axe/petit axe) de la goutte en fonction du temps. Ces courbes de relaxation sont établies pour les formulations principales (suspensions A, B, C, D et solution d'alginate sans particule) dans des conditions expérimentales différentes (bains de concentrations variables, vitesses d'impact différentes, taille de la goutte initiale, etc). Nous observons tout d'abord un effet de la quantité de calcium : d'après la Figure 0.7, plus le bain est concentré en ions calcium, plus la relaxation est rapide. Dans la Figure 0.9 (a), nous traçons l'évolution du rapport d'aspect d'une goutte de suspension A impactant trois bains de concentrations différentes. En parallèle, dans la Figure 0.9 (b), nous suivons par pesée la masse de gouttes de suspension A gélifiant dans ces trois bains différents. Il est notable que plus il y a de calcium, plus la synérèse est rapide. En parallèle, nous avons mesuré l'épaisseur de gel au cours du temps et nous avons vu que plus le bain est concentré en Ca^{2+}, plus le front de gélification est rapide, et donc plus l'expulsion d'eau par synérèse est rapide. La synérèse étant la force motrice de la relaxation, plus celle-ci est accentuée, plus la capsule relaxe vite. Cependant, nous remarquons que la forme finale de la bille n'est jamais totalement sphérique (le rapport d'aspect final est $AR_f \approx 1.1$), contrairement aux problèmes de relaxation habituellement étudiés dans la littérature. Cette observation nous conduit à prendre en compte les limites du phénomène de relaxation.

Deux principaux freins à la relaxation peuvent être identifiés : un frein visqueux et un frein mécanique. Le premier est lié aux propriétés rhéologiques du cœur liquide de la capsule. Dans la littérature, il est connu que plus le rapport des viscosités goutte/bain est élevé, plus le temps caractéristique de rétraction est grand (i.e. plus la relaxation est lente). De plus, dans le cas de fluides à seuil, un second frein visqueux entre en jeu : le

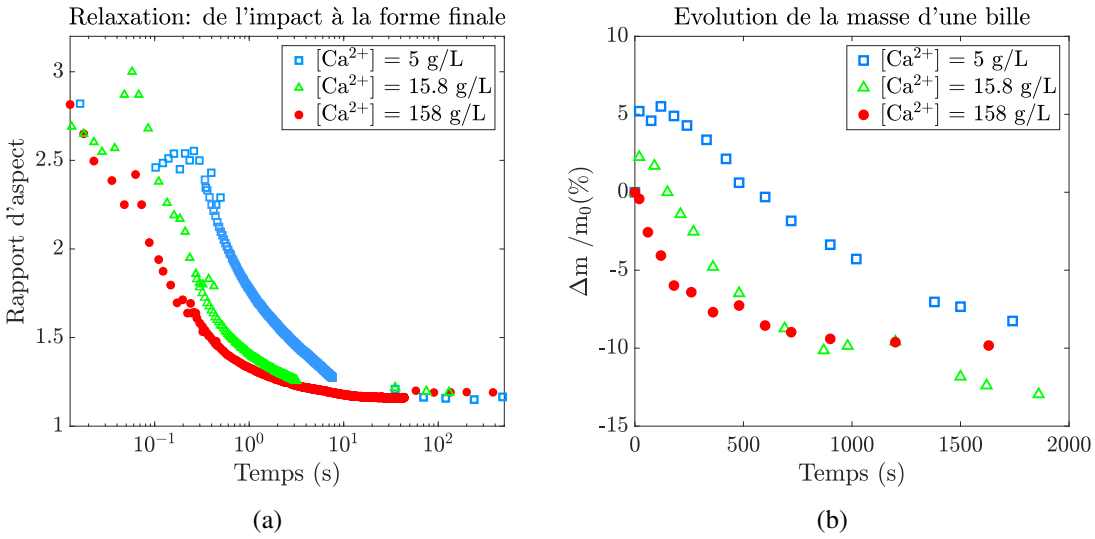

(a) (b)

Figure 0.9 *Effet de la concentration en calcium sur (a) la relaxation et (b) la perte de volume d'une goutte de suspension A (250 kg/mol alginate à 0.8%m) impactant 3 bains de concentrations différentes [Ca^{2+}] = 158 g/L, 15.8 g/L et 5 g/L.*

seuil d'écoulement. Si celui-ci est suffisamment élevé par rapport à la contrainte motrice de relaxation, alors la goutte peut se retrouver bloquée dans sa configuration déformée.

Le deuxième frein est lié aux propriétés mécaniques de la membrane gélifiée de la capsule. En effet, en augmentant la concentration en calcium dans le bain, l'épaisseur de la membrane gélifiée croît plus rapidement, ce qui a pour effet d'accélérer le moteur de la relaxation mais aussi son frein. De fait, plus la coque gélifiée est épaisse et/ou rigide, plus l'énergie requise pour la courber est grande. A partir d'une certaine épaisseur critique (environ 155 μm pour la suspension A), la capsule se retrouve alors figée avant d'atteindre une forme parfaitement sphérique (i.e. rapport d'aspect égal à 1).

Un troisième obstacle de la relaxation peut-être identifié dans notre cas : la gravité. Effectivement, nos suspensions contiennent de la zircone, très dense, ce qui peut avoir un impact non négligeable sur la relaxation de gouttes millimétriques.

Nous pouvons estimer, pour la suspension A de référence, les contraintes associées au moteur et aux freins de la relaxation. En ordre de grandeur, la tension élastique due au phénomène de synérèse est estimée grâce au module élastique du gel final, au volume d'eau expulsé par synérèse pour atteindre l'équilibre, ainsi qu'à l'épaisseur de la membrane gélifiée au début de la relaxation. On trouve $T \approx 1 - 50$ mN/m, qui est du même ordre de grandeur qu'une tension de surface d'un liquide. Cette tension élastique induit un gradient de pression ΔP à l'intérieur de la goutte qui est responsable

de la rétraction de celle-ci. On trouve $\Delta P \approx 1 - 10$ Pa. En analysant la dynamique de relaxation à temps très courts, on en déduit le taux de cisaillement auquel est soumis la goutte ($\dot{\gamma_{eff}} \approx 0.5\ s^{-1}$), ainsi que sa viscosité, ce qui nous permet d'estimer la contrainte associée aux pertes visqueuses : $\sigma_{visq} \approx 1 - 10$ Pa. La contrainte seuil est négligeable : $\sigma_y \approx 0.3$ Pa. La contrainte associée au frein mécanique est obtenue à partir de l'énergie de flexion d'une membrane fine (en 2D). On trouve, pour une épaisseur critique de membrane gélifiée égale à 155 μm : $\sigma_{bend} \approx 3 - 30$ Pa, du même ordre de grandeur que la contrainte motrice de relaxation. Enfin, nous estimons la contrainte liée à la différence de densités entre la goutte et le bain : $\sigma_g \approx 4$ Pa. Ces valeurs diffèrent selon la suspension (quantité d'alginate et de zircone) et la concentration du bain. Néanmoins nous pouvons conclure que le phénomène de relaxation est actionné par la synérèse et freiné par un certain nombre d'obstacles.

Pour conclure, afin de limiter la déformation des gouttes à l'impact, nous pouvons augmenter la viscosité de la suspension. Cependant, en faisant cela, les pertes visqueuses durant la relaxation sont plus importantes et le module élastique du gel est plus élevé, ce qui freine la relaxation et favorise son blocage. De même, pour accélérer la relaxation, nous pouvons augmenter la concentration en calcium du bain. Mais de cette façon, la gélification est accélérée et la contrainte associée à la flexion de la membrane gélifiée, proportionnelle à h^3, devient plus importante, ce qui entraîne le blocage de la relaxation. Les étapes clés du procédé de drip casting, accompagnées des mécanismes physico-chimiques en jeu sont résumé dans la Figure 0.10.

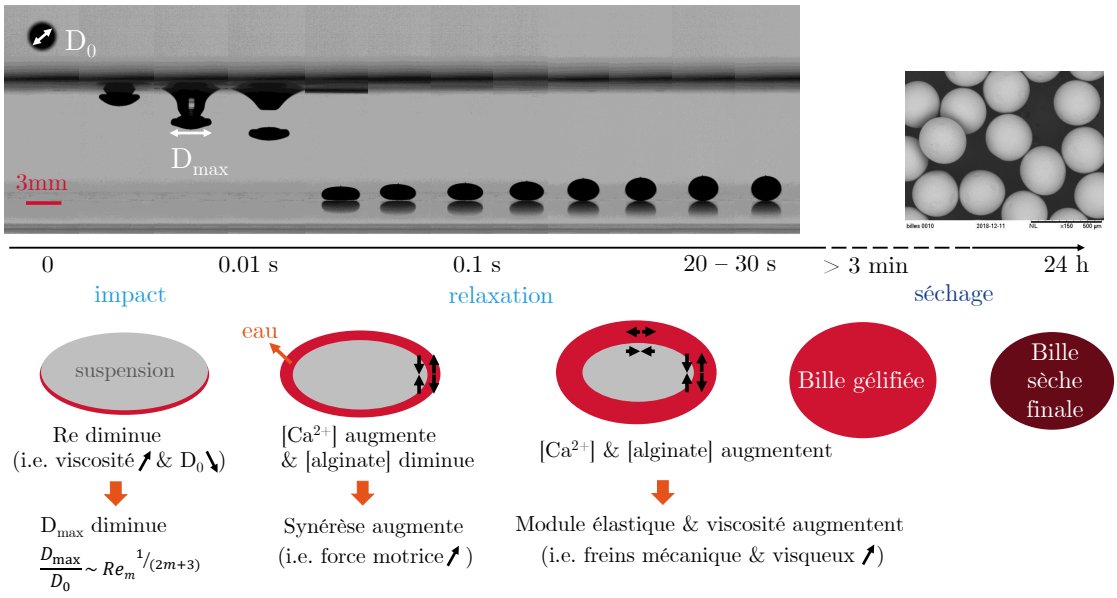

Figure 0.10 *Schéma résumé des étapes clés du procédé de drip casting.*

Chapter 1

Introduction

1.1 Industrial context

1.1.1 Ceramic beads applications

Ceramic beads are largely used in a wide range of industrial fields from ball bearing to catalyst support. The spherical shape ensures a good mobility and a geometrical organization of the objects. The material composition is selected depending on the desired application, leading to beads with good mechanical (hardness, stiffness), electrical or thermal properties and/or good chemical reactivity. Some examples include:

- Ball bearings.
- Surface treatment applications, where ceramic beads are projected at high speed on a substrate for cleaning purposes, cosmetic finishing (by changing the surface aspect), or enhancing the mechanical properties of the substrate (shot peening).
- Catalyst supports: ceramic balls are widely used as catalyst or adsorbent bed support media in refining, petrochemical, and gas processing applications due to their resistance to erosion and attrition as well as high pressure and temperature. The ceramic itself can also be chosen for its chemical activity.
- Milling media: ceramic beads are used in dry or wet milling for the comminution of various materials, from mineral ores to pharmaceutical ingredients.
- Fillers in polymeric matrices: the ceramic beads can improve mechanical, electrical and/or thermal properties of such composite materials.

There are two main types of ceramic beads: **fused beads** (formed at high temperature directly from melted ceramic raw material) and **sintered beads** formed at lower temperature before being consolidated by sintering at a temperature generally higher than 1000°C. Some applications require the use of aggregated ceramic grains in spherical shapes, without sintering.

1.1.2 Ceramic beads manufacturing

Fused beads are produced by **electric arc fusion** or **plasma fusion**. In the first case, the ceramic powder is melted at very high temperature using electric current through graphite electrodes, and then the liquid is atomized, resulting in the formation of droplets which harden during their fall as they are cooled down. In the second case, the initial ceramic powder is fed into a plasma torch, thus consequently melts and forms spherical liquid droplets which solidify.

As for sintered beads, different manufacturing processes are used. In all cases, the ceramic powder is formed at low temperature in a spherical shape, generally with organic binders, and is then subsequently treated at high temperature for consolidation. The **granulation process** uses the technique of particle enlargement by agglomeration technique: ceramic powders are transformed into granules that can be consolidated by sintering. Granulation can either be done by a dry process where the ceramic powders are compressed together to form granules, or by a wet process using a liquid binder (a polymer solution for instance) ensuring capillary bridges between ceramic particles. **Spray-drying** is another manufacturing process, where a suspension jet is fragmented into a spray (droplets into a gas phase) and then dried by hot air blowing in the chamber. **Powder injection-molding** identical to plastic injection-molding, can also be used to manufacture ceramic balls: the powder is mixed with a binder and injected into a mold before being sintered. Another way to produce ceramic beads is through **Drip-casting** process. It uses the encapsulation technique with alginate, a natural polymer able to form a gel when in contact with divalent cations (see Chapter 3). A suspension containing ceramic particles (zirconia) and alginate is prepared and then dripped into a bath containing gelation agents (calcium ions for example), resulting in the formation of gelled alginate-ceramic beads. This last process is of great interest to Saint-Gobain as it ensures a production of monodisperse beads with good mechanical properties and gives flexibility regarding the manufacturing volume. In this work, we will focus exclusively on drip-casting process, schematized in Figure 1.1.

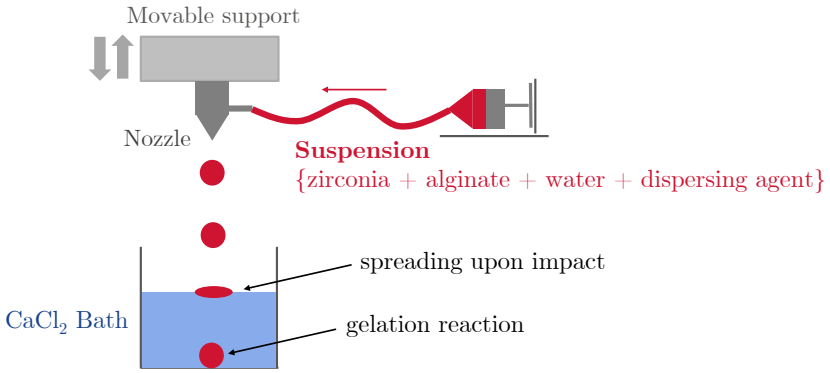

Figure 1.1 *Drip-casting process.*

1.2 Scientific questions and challenges to overcome

Although drip-casting process is robust way to produce monodisperse ceramic beads, it raises issues concerning their final shape and size. Indeed, the final beads are often slightly flattened, which is unacceptable for certain applications. As a matter of fact, during the process, droplets fall down into a gelling bath, so they spread upon impact with the liquid bath. Moreover, as soon as the droplets enter the $CaCl_2$ bath, they start to solidify because of the gelation reaction between alginate and Ca^{2+} ions. Therefore, the major issue of this process is that the droplets are deformed during impact and start to gel in their elongated shape, resulting in non-spherical beads.

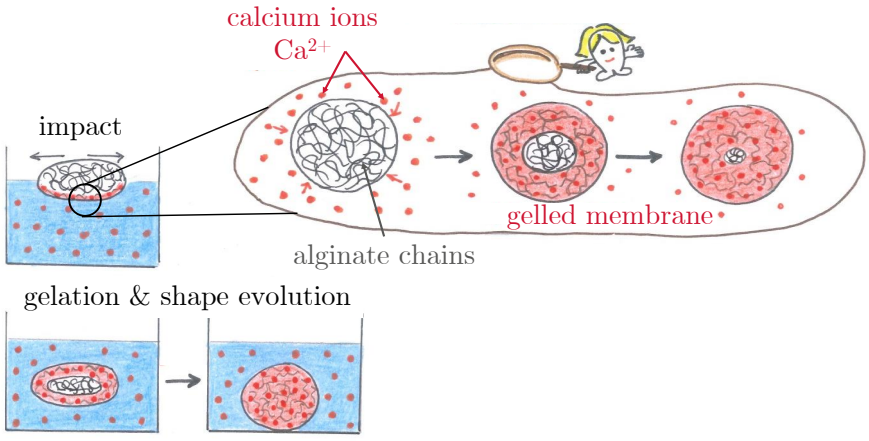

Figure 1.2 *Dripping process involves deformation upon impact and a gelation process at the same time.*

The aim of this work is to answer these following questions:

- What are the mechanisms governing the final shape of the beads?
- Which formulation or process parameters can we tune to have more spherical beads?

Different challenges were faced in this thesis, they are mentioned hereafter.

Droplet composition The suspension used for dripping purposes has a non-Newtonian shear-thinning behavior due to the interaction between ceramic particles and alginate chains. Thus, the suspension viscosity varies at each step of the process (inside the nozzle, upon impact and during the gelation step). That is why we need to characterize and control precisely the rheological properties of the alginate-ceramic suspensions. This will be done in Chapter 2.

Droplet gelation Once in the calcium bath, the droplets start to gel so it is necessary to understand the interaction between the suspension and the Ca^{2+} ions, i.e. the kinetics of the gelation reaction and the effect of calcium concentration or suspension composition on the gelation process. This will be studied in Chapter 3.

Droplet shape evolution We have developed a set-up to visualize the capsule shape at each stage of the process (during impact and penetration in the calcium bath and during the gelation until reaching its final shape) with a high-speed camera. Despite a lot of literature on alginate capusles, there are very few studies on the dynamics of the bead shape in situ. We mainly find post-process shape analyses. The major difficulty is to link our observations with the physico-chemical mechanisms involved in the process. This will be discussed in Chapters 4 and 5.

Part I

Alginate solutions and suspensions: rheology and gelation

Introduction of Part I

As mentioned earlier, in the drip-casting process, rheology plays an important part as the suspension is sheared inside the nozzle and upon impact with the gelling bath. Later in the manuscript, we will exhibit the influence of rheology on the droplets shape. Moreover, in our case, the droplet is not a simple polymer solution (as it is generally the case for encapsulation purposes) but a complex fluid composed of alginate and zirconia particles. That is why, in this first part, we seek to characterize, understand and control the rheological properties of the droplet.

On the other hand, when the droplet reaches the calcium bath, it starts to gel. Later in Chapter 5, we will show that the gelation reaction modifies the shape evolution dynamics of the droplet. Consequently, in this part, we will also study the gelation of the suspensions in the presence of Ca^{2+} ions in order to understand the gelation mechanism as well as the final mechanical properties of the gelled beads.

Chapter 2

Suspension preparation & rheological properties

During the drip-casting process, the alginate-ceramic suspension undergoes shearing in the nozzle and elongation upon impact so it is very important to characterize their rheological behavior in order to predict and control the state of the suspension at each step of the dripping process. In fact, the suspensions used are complex fluids, composed of polyelectrolytes (alginate) and particles (zirconia), so we expect the polymer chains and the particles to interact. In this chapter, after giving a state of the art on polyelectrolyte solutions and particle suspensions, we will present our system and investigate on the interactions between zirconia particles and both polymers used in our study, sodium alginate and poly(acrylic acid ammonium salt), through rheological characterization.

2.1 Polyelectrolytes solutions & particle suspensions: state of the art

2.1.1 Alginate, a natural polyelectrolyte

Alginate is a natural polysaccharide extracted from brown seaweed and its basic structure consists of an alternation of D-Mannuronic acid (M-block) monomers and L-Guluronic acid (G-block) monomers (see Figure 2.1). With carboxylate functions -COO^-, alginate is a polyelectrolyte. Its molecular weight can range from 50 g/mol to 10^6 g/mol. The alternation and length of G-blocks and M-blocks depend on the geographical origin of alginates and can be determined by ^{1}H-NMR spectroscopy (see Section 2.2.4.a)). Penman and Sanderson [1] reported that brittle gels are obtained from alginates with low M/G ratio while elastic gels are formed from alginates with high M/G ratio. However, it must be noted that the gel properties are also related to the presence of homopolymeric block structures (F_{GG} or F_{MM}) and alternating blocks (F_{MG}).

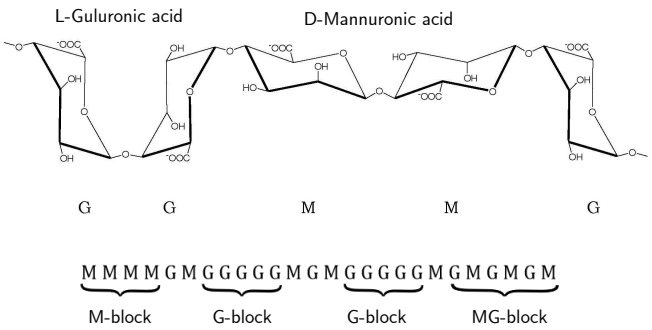

Figure 2.1 *Alginate structure and composition: M-blocks and G-blocks.*

2.1.2 Rheology of polyelectrolytes

Definition and conformational properties Polyelectrolytes are polymers with ionizable groups. In solution they are dissociated into polyvalent macro-ions (ions on the polymeric chain) and counterions of opposite charge. The high charge of the polyion induces a strong electric field which attracts these counterions, resulting in their partial condensation onto the polymer backbone. This phenomenon is referred to as the Manning-Oosawa counterion condensation [2, 3] and is illustrated in Figure 2.2.

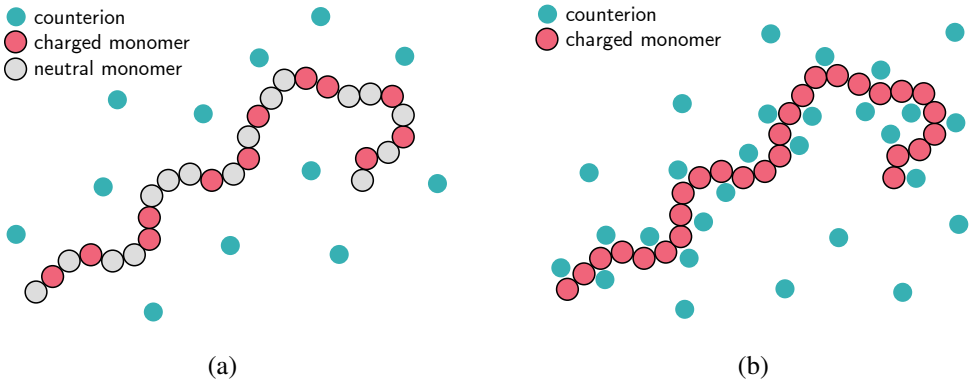

Figure 2.2 *Schematic representation of a polyelectrolyte solution: Manning-Oosawa counterion condensation. (a) Weakly charged polyelectrolyte. (b) Strongly charged polyelectrolyte and condensation phenomenon.*

This interaction between the polyvalent macro-ion and counterions is the origin of characteristic properties of polyelectrolytes remarkably different from solutions of uncharged polymers. Most of the polyelectrolyte chains are long and flexible but their conformation depends on their charge and interaction with counterions [3].

In **dilute salt-free solution**, the counterions are homogeneously distributed in the solution volume and so the charges on the polymer chains interact via the unscreened Coulom potential. De Gennes et al. [4] implemented the concept of "blobs" to polyelectrolytes: the polyion can be separated into parts called 'blobs' of characteristic size D. For length scales smaller than D, the polymer conformation is similar to the one of a neutral polymer in solution. Therefore, within a blob, the statistics of the chain is determined by the thermodynamic interaction between the neutral polymer and the solvent. This means that the total energy of the electrostatic interaction between charges inside the blob is of the order of the thermal energy kT [4–6]. On larger length scales (l > D), the blobs are subjected to electrostatic repulsion so they tend to align thus forming a fully extended chain of electrostatic blobs of length L as illustrated in Figure 2.3 (a).

In **semi-dilute solution** we can define a correlation length ξ [7]. For length scales smaller than ξ, the dilute solution scaling applies. On larger length scales (l > ξ), the chain can be described by a random walk of correlation blobs as shown in Figure 2.3 (b).

With increasing charge or concentration, the flexible polymer chain changes its shape from a contracted random coil to a fully extended conformation. Therefore, when studying the rheology of polyelectrolyte solutions, we need to distinguish between the case of a solution without salt and the case where the polyelectrolyte is in the presence of salt.

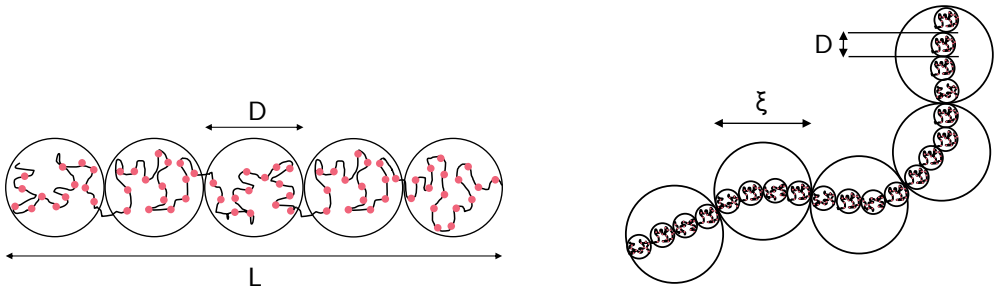

(a) (b)

Figure 2.3 *Conformation of polyelectrolyte chains: the concept of blobs. The red filled circles are charged groups. (a) Polyelectrolyte chain in* ***dilute*** *solution: an extended chain of electrostatic blobs. (b) Polyelectrolyte chain in* ***semi-dilute*** *solution: a random-walk of correlation blobs, each of which is an extended configuration of electrostatic blobs.*

The electrical effect of the highly charged polymer chain is expected to be screened when a high concentration of small ions is introduced (i.e. by addition of small electrolytes).

Rheological properties Chain conformation controls the rheology. The particular conformation of polyelectrolytes due to the presence of charges is the reason why polyelectrolytes have different rheological properties from neutral polymers. To characterize them, the specific viscosity is generally used. It is defined as $\eta_{sp} = \frac{\eta_0 - \eta_w}{\eta_w}$ with η_0 the zero-shear plateau viscosity of the polymer solution and η_w the viscosity of water (the solvent).

At low concentrations, Fuoss and Strauss [8] were the first ones to examine the slower increase of the specific viscosity with concentration in polyelectrolyte semi-dilute solutions ($\eta_{sp} \sim c^{1/2}$) while for solutions of uncharged polymers at the same concentration, viscosity is proportional to concentration ($\eta_{sp} \sim c^1$).

Later, the scaling theory of polyelectrolyte solutions has been extended and generalized to both unentangled and entangled regimes by Dobrynin, Colby and Rubinstein [6, 9]. They studied the rheological behavior of solutions of salt-free polyelectrolytes and determined the overlap concentration c^*, the entanglement concentration c_e and the electrostatic blob overlap concentration c^{**} from the curve plotting the specific viscosity against concentration (see red curve in Figure 2.4). Lopez et al. [10] investigated the concentration and molecular weight dependence of viscosity of semi-flexible sodium carboxymethylcellulose in aqueous salt-free and NaCl solutions. As expected, the solution viscosity decreases with increasing salt amount, the effect being more pronounced

at lower polymer concentrations (in the semi-dilute unentangled regime, $c^* > c > c_e$). In this regime, the viscosity evolution obeys the scaling law $\eta_{sp} \sim c^{1.3}$ at high salt concentration (instead of $\eta_{sp} \sim c^{1/2}$ in salt-free solutions). Above a certain salt content (0.1 M), the effect of added salt appears to saturate. As a matter of fact, at 0.1 M, the Debye-Hückel screening length is approximately 1 nm corresponding to the distance between dissociated charges along the chain. Therefore, the charges are fully screened from each other at a salt concentration above 0.1 M. At higher polymer concentrations, the presence of salt has no effect on the sample viscosity.

In the entangled regime ($c > c_e$), the scaling law of uncharged polymers is predicted to be $\eta_{sp} \sim c^{15/4}$ in good solvents. For polyelectrolyte solutions, the situation is more complex. For $c_e > c > c^{**}$, the concentration dependence of viscosity is much weaker: $\eta_{sp} \sim c^{3/2}$. Then, for higher concentrations, electrostatic blobs begin to overlap and we expect the solution dynamics to be similar to that of neutral polymers. In practice, c^{**} is defined as the crossover concentration to a viscosity power law $\eta_{sp} \sim c^{3-4}$ [11]. Overall, the behavior of polyelectrolytes at high salt concentrations is comparable to the one of neutral polymers because salt ions strongly screen the Coulomb interaction between charged monomers [9, 12]. A summary of the scaling theory for polyelectrolytes is shown in Figure 2.4.

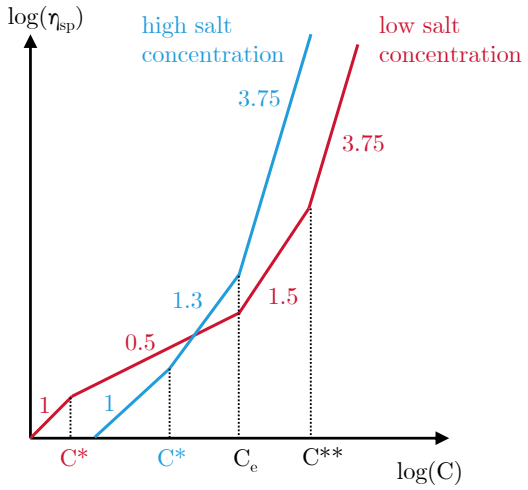

Figure 2.4 *Predicted power laws from scaling theory showing the concentration dependence of specific viscosity for polyelectrolyte solutions at low salt concentration (in red) and high salt concentration (in blue). Adapted from [11] and [13].*

2.1.3 Osmotic pressure in polyelectrolytes

Another important property of polyelectrolytes which is remarkably different from neutral polymers is the osmotic pressure. In fact, the osmotic pressure of a semi-dilute solution of neutral polymers is essentially the thermal energy kT per correlation volume (ξ^3):

$$\frac{\Pi_p}{kT} \approx \frac{1}{\xi^3} \qquad \mathrm{c} > c^*$$

Polyelectrolyte solutions have an additional contribution to their osmotic pressure because of ions Π_i, such that the total osmotic pressure is $\Pi \approx \Pi_p + \Pi_i$. Donnan equilibrium [14] requires charge neutrality on both sides of the membrane separating the polyelectrolyte solution from pure solvent. To calculate the ion contribution, we must take into account the counterions (of concentration c in number density) and the salt ions (of concentration c_s in number density) [6]. In the case of polyelectrolyte solutions with many more counterions than salt ions (i.e. $\mathrm{c} >> 2Ac_s$, A being the number of monomers between uncondensed charges), the ion contribution can be written as:

$$\frac{\Pi_i}{kT} \approx \frac{c}{A} \qquad \mathrm{c} >> 2Ac_s \tag{2.1}$$

In the other limit, where salt concentration is high, the counterions are almost uniformly distributed on both sides of the membrane and the salt redistributes to maintain charge neutrality. This redistribution gives a contribution to osmotic pressure and can be expressed as follows:

$$\frac{\Pi_i}{kT} \approx \frac{c^2}{4\,A^2\,c_s} \qquad \mathrm{c} << 2Ac_s \tag{2.2}$$

By combining Equations (2.1) and (2.2), we obtain a single expression for Π_i, extrapolating between the two limit behaviors:

$$\frac{\Pi_i}{kT} \approx \frac{c^2}{4\,A^2\,c_s + Ac} \tag{2.3}$$

For the large majority of systems studied to date [6], the osmotic pressure of polyelectrolyte solutions is dominated by the ionic contribution, so Equation (2.3) is always valid and the polymer contribution is negligible.

2.1.4 Interaction with particles

Adding polylectrolytes in a suspension containing particles affects greatly the rheological properties as well as the stability of such suspensions [15, 16]. Two cases must be considered: either the macromolecules adsorb onto the particles surface, or they do not. The polymer adsorption depends on its charge density, its molecular weight and its concentration as well as the particles size and surface energy [17].

If the added polyelectrolyte is non-adsorptive to the colloid surface, we can observe the flocculation of the colloidal particles by depletion [18, 19]. In fact, since the polymer do not adsorb onto the particle surface, we can define an excluded volume around each colloid. When the concentration of added polymer increases, the system will tend to decrease the excluded volume by bringing the particles together in order to increase the entropy. Figure 2.5 (a) illustrates this depletion phenomenon.

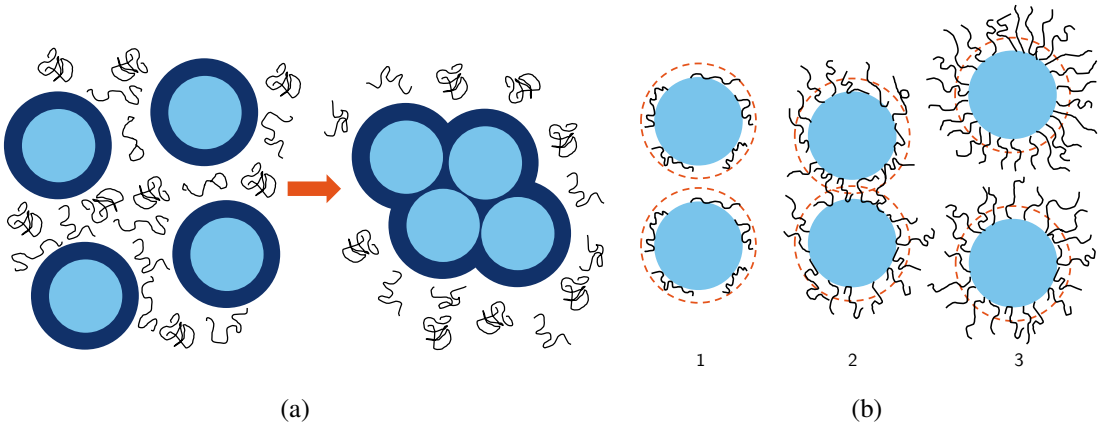

Figure 2.5 *Flocculation of colloidal suspensions induced by addition of polyelectrolytes. (a) Flocculation by depletion. The dark blue circles represent the excluded volume. (b) Flocculation by bridging. The dashed circles represent the electric double layer.*

If the polyelectrolytes adsorb onto the particles surface, three possible cases can be observed depending on their concentration [20–22]. Let us consider a colloidal suspension electrostatically stabilized in which we add polymer chains of radius of gyration $R_g > \lambda_D$, the Debye length defining the electric double layer around the charged colloidal particles. For low polymer concentrations, the macromolecules will adsorb onto the particles and adopt a flat configuration, smaller than λ_D, keeping the system stabilized by electrostatic repulsion. When we increase the concentration of added polymers, more chains will adsorb onto the colloids, forming a thicker adsorption layer (larger than λ_D).

In that case, polymer chains can adsorb onto different particles, creating bridges between them and resulting in their flocculation. For even higher polymer concentrations, the particles surface is saturated and bridging is not possible anymore. Consequently, the adsorbed polymer chains act like stabilizers because of steric repulsion between them. For low molecular weight polymers, bridging is not possible and the adsorption always leads to steric stabilization. A summary is shown in Figure 2.5 (b).

Blijdenstein et al. [23] described an experimental rheological comparison between bridging-flocculated and depletion-flocculated oil-in-water emulsions. In the case of non-adsorbing polysaccharides, depletion of polymers around oil droplets induces a weak attraction. In protein-stabilized emulsions, this depletion attraction adds up to van der Waals and electrostatic forces leading to flexible droplet - droplet bonds. Last, in the case of strong adsorption of polysaccharides onto the protein layer at the oil droplet surface, individual polysaccharide molecules can adsorb on different droplets which results in strong and stiff polymer bridges between the droplets. Dynamic rheological measurements (strainsweep at 1 Hz) were performed on the different emulsion types, giving rise to the evolution of elastic modulus (G') as a function of droplet volume fraction Φ. They found that bridging-flocculated emulsions gave a steeper slope n (typically $n = 5.1 \pm 0.3$) than depletion-flocculated emulsions where $n = 2.9 \pm 0.1$.

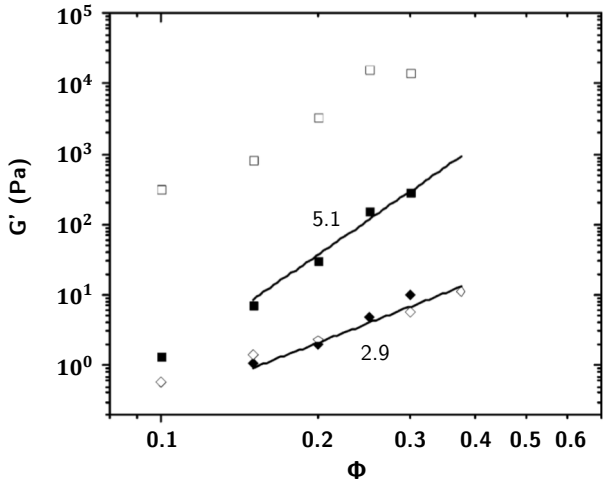

Figure 2.6 *Log-log plot of elastic modulus G' against the volume fraction Φ of dispersed particles (emulsion droplets here) for depletion-flocculated emulsions (♦) and bridging-flocculated emulsions (■). Data determined by rheology at 1 Hz (filled symbols) and by DWS (open symbols). Adapted from [23].*

Similarly, the flocculation of particles induced by the addition of polymers can arise from these two different mechanisms (depletion or bridging). Zhao et al. [24] studied

the aggregation of microspheres by addition of microgels. As in [23, 25], the elastic exponent n resulting from $G' \propto \phi^n$ has been reported to be $n \approx 2-3$ for depletion gels and much larger $n \approx 4-5$ for bridging gels.

2.2 Materials

2.2.1 Calcium chloride

Calcium chloride hexahydrate 98% is used to prepare gelling baths of different concentrations: 1.58 g/L, 5 g/L, 15.8 g/L, 158 g/L and 374 g/L. These values explore a large range of concentrations above and below the one typically used in the industrial process.

2.2.2 Zirconia

A batch of zirconia powder is provided by Saint-Gobain Zirpro, HanDan (China) with the following physico-chemical characteristics: a **specific surface area** of 11 m^2/g and a mean particle median diameter of 200 nm. All these analyses were previously done internally by ICP-AES (Inductively Coupled Plasma - Atomic Emission Spectrometry), laser granulometry and BET method to obtain the powder's mass composition, its size distribution and specific surface area repectively. The same batch is used throughout all the PhD to ensure reproducibility.

Particle size is verified in the laboratory using Dynamic Light Scatering (DLS). To do so, we dilute a sample of pre-milled zirconia suspension in a large amount of deionized water. We measure a mean radius of 150 nm is obtained for an angle of 90°. To confirm the grain size (since they are not spherical), we perform Scanning Electron Microscopy (SEM) observation on a dried micro-droplet of 2000 times diluted suspension. The picture is taken under a 13 pA current and a 5 kV voltage.

Zeta potential measurements are also performed on diluted zirconia suspensions (0.1 g/L) at different pH (adding formic acid or ammonia solution) using a Malvern Zetasizer Nano ZS90. As illustrated in Figure 2.8, zeta potential variations with pH give rise to an isoelectric point of 7.5 for our zirconia powder. This value is consistent with previous studies measuring a point of zero charge between 6 and 8 [26, 27].

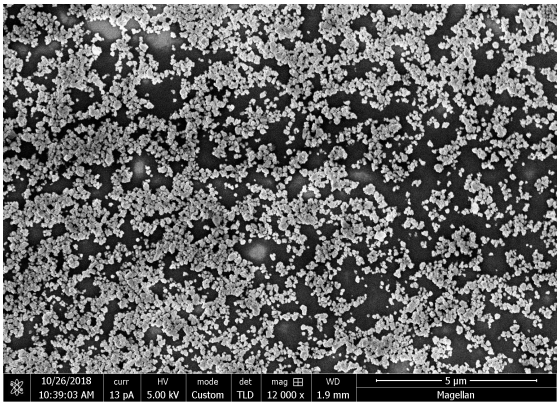

Figure 2.7 *SEM picture of a diluted droplet suspension after the grinding process.*

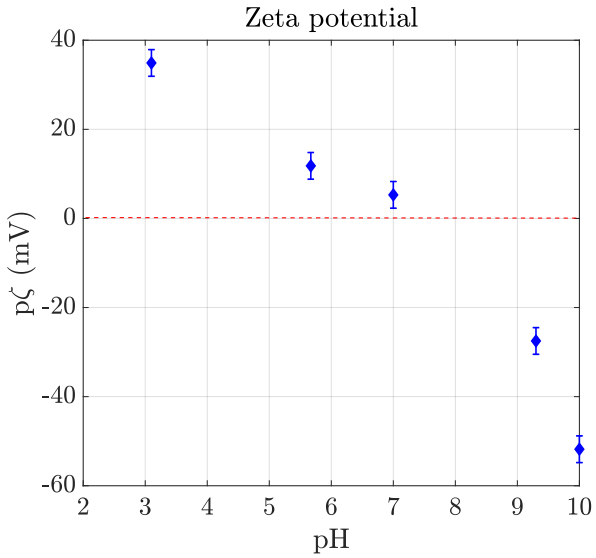

Figure 2.8 *Zirconia zeta potential measurements.*

2.2.3 Dispersing agent (PAA)

The dispersing agent used industrially to prevent zirconia grains to sediment or agglomerate is a commercial product (confidential). It appears as a yellow liquid of density 1.09 and a pH equal to 8.6. We can give its approximate chemical description: the product is a solution of 25%wt poly(acrylic acid) ammonium salt (PAA, NH^{4+}) of small molecular weight (4500 g/mol). When added to the zirconia suspension, it stabilizes the pH around 8.6. From now on, we refer to it as PAA.

2.2.4 Alginates

All sodium alginates used during this study are purchased from AGI company. We mainly focus on one batch in the entire manuscript which we characterize below.

a) Chemical characterization

M/G ratio determination ^{1}H-NMR spectroscopy is performed on 1 g/L sodium alginate solution in D_2O. In order to increase the signal-to-noise ratio, the analyses are achieved at a temperature of 80°C with a Bruker Avance III 600 MHz. The NMR experiments are recorded with a spectral width of 6009 Hz, a relaxation delay of 20 s and a number of scans of 64.

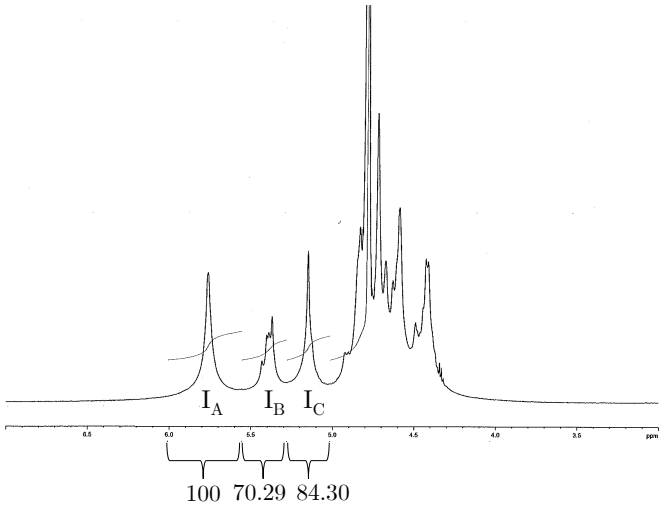

Figure 2.9 *NMR spectrum on alginate solution at 1 g/L in D_2O.*

The NMR spectrum can give us access to the chemical composition (fraction of G-blocks and M-blocks) by comparison of signal areas I_A, I_B and I_C using the equations proposed by Gasdalen et al. [28]:

$$F_G = \frac{I_A}{I_B + I_C}$$
$$F_M = 1 - F_G$$
$$M/G = \frac{F_M}{F_G}$$

For sake of consistency, our NRM spectrum is compared with other data collected by Fertah et al. [29] and Fenoradosoa et al. [30]. We obtain $F_G = 0.65$ and a M/G ratio equal to 0.55. This ratio is quite low, which is characteristic of strong and brittle gels according to [1].

Molecular weight determination Size exclusion chromatography (SEC) is performed on alginate samples to determine their average molecular weight. Solutions of sodium alginate are prepared at 2 mg/mL in $NaNO_3$ 0.2 M. The measurements give an average molecular weight of M_w = 250 kg/mol and M_n = 125 kg/mol which results in a polydispersity index of 1.7 ± 0.3.

b) Experimental protocol to reduce alginate M_w

We have decided to reduce the chain molecular weight (M_w) in order to be able to add more alginate in the suspension without increasing considerably its viscosity while ensuring a larger bead stiffness after gelation, to prevent its deformation at the end of the drip-casting process.

Holme et al. [31] studied the thermal depolymerization of alginates in the solid state. Following this idea, we manage to have a robust and reproducible potocol to cut the alginate chains. We use a glass container (20 mL) in which we put sodium alginate powder (5 g), close it and put it in a drying oven at 120°C for 24 hours. After this heating step, the container is transferred in an iced bath for several minutes and then stored in the fridge.

We analyze the resulting powder by size exclusion chromatography and ^{1}H-NMR, giving a molecular weight of M_w = 60 kg/mol and a polydispersity index of 1.7 ± 0.3. Whenever this protocol is used to reduce the sodium alginate chain size, a SEC analysis is performed to be sure we obtain the same molecular weight value of 60 kg/mol.

2.3 Suspension preparation

2.3.1 Zirconia milling

The first step of the formulation is **Powder dispersion**. In order to redisperse and deagglomerate zirconia powder, a "home-made" attrition grinding set-up is made with the help of the lab's workshop. The principle is as follows: the suspension (zirconia

+ water + PAA) is placed in the milling reservoir along side sintered zirconia beads of diameter 0.8 mm. The vane rotates with an imposed torque (1000 rpm), causing the zirconia agglomerates to break by collision and shear force of the beads. The beads are retained in the white chamber thanks to a 0.5 mm mesh sieve. The grinded suspension flows down the container where it is agitated and extracted to be reinjected in the milling reservoir with a recirculation tube using a peristaltic pump (see Figure 2.10).

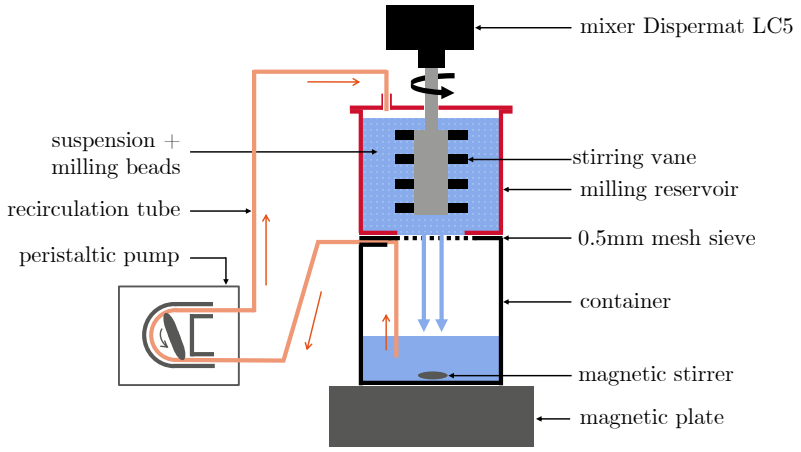

Figure 2.10 *Principle of the wet milling set-up.*

The following protocol is adjusted to obtain a grain size distribution comparable to the one used for industrial tests at Saint-Gobain Research Provence. A suspension containing 1323 g of water, 27 g of PAA and 900 g of zirconia powder is agitated for 12 h with a rotating blade. Then, the suspension is transferred in the milling reservoir with 1.5 kg of grinding beads and the attrition grinding process starts and usually lasts 4 hours. Throughout this grinding step, DLS measures are carried out until the desired size is obtained (mean radius of 150 nm for an angle of 90°). Once the suspension has been grinded, it is stored on a orbital shaker (IKA KS 501) to prevent sedimentation.

2.3.2 Addition of alginate and suspensions studied

The next step of the formulation is the **addition of alginate**. To do so, a small quantity (50 g - 300 g) of the previous suspension is collected and alginate powder is added under agitation at 1000 - 1500 rpm for 30 minutes. After this 30 min step, the zirconia - alginate suspension is characterized by rheometry and used in the dripping process.

For instance, the reference suspension (A) is made by adding 0.8 g of alginate powder to 100 g of zirconia suspension (containing 40 g of zirconia and 60 g of water). Thus, the alginate concentration is 0.8%wt but in volume in the aqueous phase, the concentration is 0.8/60 = 13.1 g/L. We are interested in the volumic concentrations because it will enable us to determine the polymer regime (semi-dilute? entangled?). Throughout this thesis, four main suspensions are studied. Their composition is summarized in the following Table 2.1.

Suspension	Alginate M_w (in kg/mol)	Alginate conc. in the susp. (in %wt)	Alginate conc. in water phase (in g/L)	Zirconia conc. (in %wt)
A	250	0.8	13.1	40
B	250	0.4	6.6	40
C	250	1.6	26.2	40
D	60	5	82.0	40

Table 2.1 *Summary table of suspensions composition.*

2.4 Zirconia - PAA (dispersant) interaction

2.4.1 Total Organic Carbon (TOC) principle

In order to investigate on the interactions between the components of the suspension, we use a Total Organic Carbon analyzer (TOC-V CSH from Shimadzu). The principle is the following: samples are combusted at high temperature (700°C) in an oxygen-rich atmosphere. All carbon present is converted into carbon dioxide which flows through scrubber tubes. The amount of carbon dioxide is measured using an Infrared Detector, resulting in a measured area. A calibration curve must be done to translate the corresponding areas to the desired specie concentrations.

Thanks to the calibration curve, the data collected allow us to calculate Γ, the surface coverage using Equation (2.4). The resulting adsorption isotherm can be plotted.

$$\Gamma = \frac{[\mathrm{PAA}]_{\mathrm{initial}} - [\mathrm{PAA}]_{\mathrm{measured}}}{[\mathrm{Zir}] \times \mathrm{SSA}} \tag{2.4}$$

with $[\mathrm{PAA}]_{\mathrm{initial}}$ the initial dispersant concentration (in g/L) in the tube, $[\mathrm{PAA}]_{\mathrm{measured}}$ the final free PAA concentration (in g/L) in the supernatent, measured by the TOC analyzer,

[Zir] the concentration of zirconia particles (in g/L) and SSA the specific surface area of the zirconia powder (11 m^2/g, see Section 2.2).

2.4.2 Results

Adsorption of the dispersing agent PAA on zirconia particles is investigated. First, we prepare different solutions of PAA only (with concentrations from 0 g/L to 5 g/L) and obtain a calibration curve. Then, a grinding step is performed on a suspension containing water and zirconia alone, which allows us to prepare several tubes adding varying amounts of PAA. These tubes are kept on a rotating shaker for 48 hours. Then, the tubes are spun in a centrifuge to separate the zirconia particles (with their adsorbed polymer layer) from the rest of the solution. We carefully withdraw the supernatant, dilute it with water and analyze it in the TOC analyzer.

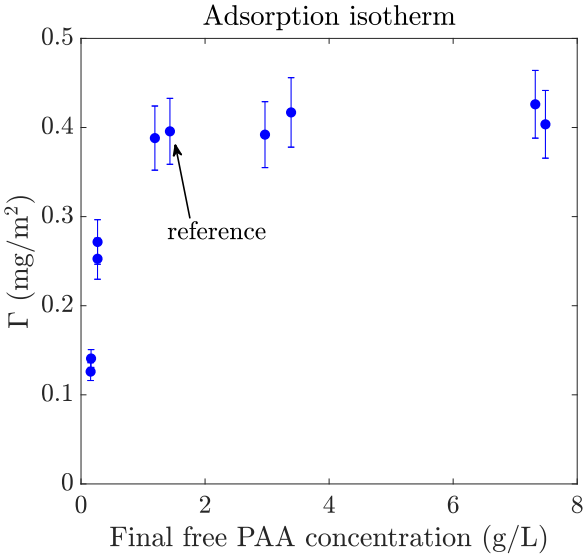

Figure 2.11 *Adsorption isotherm. The "reference" is the data point corresponding to the ratio [PAA]/[Zir] chosen for our usual dripping suspensions*

The adsorption isotherm presented in Figure 2.11 confirms the adsorption of small dispersant polymer chains (PAA) on the surface of zirconia particles, even though both are negatively charged according to the isoelectric point of zirconia (= 7.5) and the suspension pH (= 8.6). This appears to be a general feature of many ceramic powders: earlier studies on alumina [32] and zirconia [33] also measured a detectable adsorption of anionic polyelectrolytes on a negative ceramic surface. It is possible to enhance this adsorption while keeping the same pH value (for which both the polyelectrolyte and the

ceramic particles are negatively charged), by increasing the ionic strength of the solution (i.e. adding NaCl for example) [34]. By doing so, NaCl screens the repulsive interactions between the negatively charged surfaces and the negatively charged maromolecules. In our particular case, the dispersing agent used (PAA) has a very high conductivity, which suggests the presence of a large quantity of ions, screening electrostatic interactions and enabling PAA to adsorb onto the negatively charged zirconia surface.

The curve shows a plateau meaning that above a certain PAA concentration, the surface of zirconia is saturated. The ratio [PAA]/[Zir] chosen in our reference formulation corresponds to the beginning of the plateau in order to ensure maximal protection of the zirconia grains. In a previous atomic force microscopy (AFM) study on the interactions between polyacrylic acid coated zirconia surfaces, Biggs and Healy [35] were able to quantify the adsorption of low molecular weight PAA (2000 g/mol) on zirconia particles close to pH = 7 - 8 and showed that the adsorbed layer thickness was around 5 nm. Pedersen et al [33] reported a thickness of 10 - 20 nm in the case of a polyacrylic acid of average molecular weight M_w = 10 kg/mol adsorbed on a zirconia surface at high pH. In our case, pH = 8.5 and PAA's molecular weight is M_w = 4500 g/mol so we can estimate the thickness of the adsorbed polymer layer to be in between the previous measurements, i.e. 5 - 10 nm.

Zirconia - alginate interactions without dispersing agent (PAA) was impossible to study. Indeed, the zirconia suspension without dispersant is completely flocculated, and the dissolution of alginate, even at low concentration, is too difficult. We could not get a homogeneous suspension easily separated by centrifugation. The analysis of zirconia - alginate interactions in the presence of PAA requires time-consuming experiments of TOC coupled with dialysis in order to separate long polymer chains (alginate) and short ones (PAA). We decided to focus on rheological measurements to make assumptions concerning zirconia - polymer interactions.

2.5 Rheometry

Rheology plays a crucial part in the dripping process because the suspension is sheared in the nozzle, then relaxes in the air before being sheared once again upon impact. As a consequence, we need to characterize the droplet rheological properties under a wide range of conditions in order to understand and control its behavior throughout each step of the drip-casting process.

That is why, in this part, we focus on the rheological characterization of zirconia-alginate suspensions.

2.5.1 Apparatus and protocol

The rheological measurements are performed on a AR-G2 rheometer from TA Instruments, using a cone-plane geometry with a steel cone of 40 mm diameter and 2° angle.

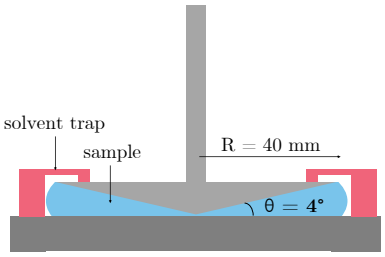

Figure 2.12 *Geometry used for all the rheological measurements.*

The main experiments carried on are continuous rotation tests to characterize the suspensions behavior under different shearing rates as well as oscillation tests to obtain information on the fluids elasticity and relaxation time. The protocols used in this work are described hereafter. Due to history dependence of the response, for all protocols, a rejuvenation step is performed first: an intense pre-shear step at 1000 s^{-1} is applied for 60 s to all samples prior to oscillation or rotational tests.

- **The flow protocol** used for all samples is the following: we impose an increasing shear rate from 0.01 s^{-1} to 1000 s^{-1}. In some cases, we also perform the reverse curve: with a decreasing shear rate from 1000 s^{-1} to 0.01 s^{-1}.

- **The strain sweep protocol** used is: we fix the frequency at 1 Hz or 1 rad/s (both were used) and the strain is varied from 0.1% to 100%.

- **The frequency sweep protocol** used is as follows: we fix the strain at 0.1% or 1% corresponding to the linear regime, and we impose a varying frequency from 100 rad/s to 0.1 - 1 rad/s.

2.5.2 Alginate solutions

First, the behavior of alginate chains (of both sizes 250 kg/mol and 60 kg/mol) in the presence of the dispersing agent PAA must be studied to identify the polymer concen-

tration regime. In fact, as seen in Section 2.2.3, PAA is a dispersing agent with high ionic strength and a pH value of 8.6. Alginate is a polyelectrolyte so its behavior is sensitive to changes in pH or ionic strength. That is why we prepare alginate solutions at different concentrations to which we add PAA (with a final concentration of 0.02 g/L, representative of the real PAA concentration in the final suspensions A, B, C and D.)

a) Long alginate chains (M_w = 250 kg/mol)

Flow curves $\eta = f(\dot{\gamma})$ are established as described in the previous section for alginate solutions of varying concentrations c. In Figure 2.13, we can see that increasing the alginate concentration induces an overall increase of the solution viscosity. Moreover, we notice that for high concentrations, the flow curves show a shear-thinning behavior at high shear rates $\dot{\gamma} \geq 100\ s^{-1}$. In fact, in the entangled state, the microstructure of the solution is like a network: the entanglements act like physical nodes restricting the motion of polymer chains resulting in a high viscosity of the solution. However, upon shearing, the chains tend to disentangle and align along the flow which consequently reduces the viscosity.

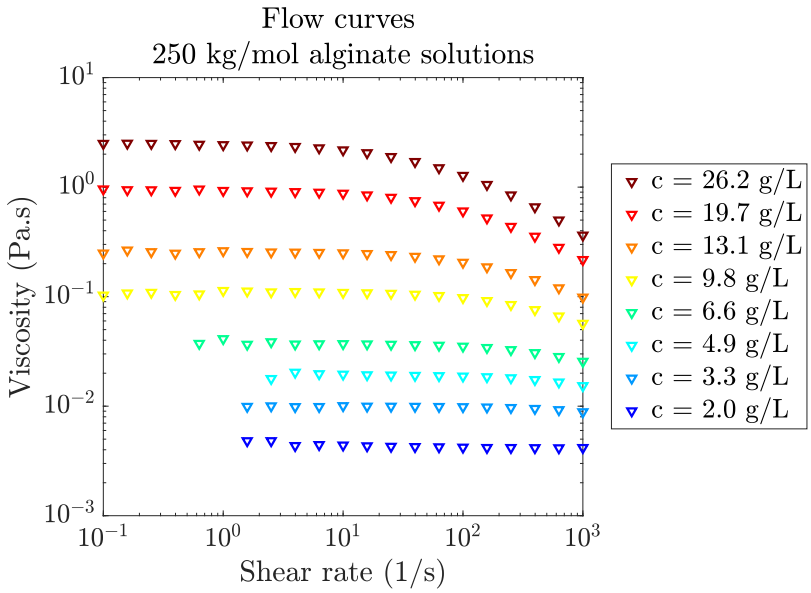

Figure 2.13 *Flow curves: evolution of viscosity as a function of shear rates for different 250 kg/mol alginate solutions in the presence of PAA.*

For the highest concentration studied (c = 26.2 g/L), the viscosity starts to decrease at a critical shear rate of $\dot{\gamma}_c \approx 20\ s^{-1}$, giving access to a relaxation time of the entangled

polymer chains: $\tau_0 = 1/\dot{\gamma}_c \approx 0.05$ s. As alginate concentration decreases, the relaxation time decreases. For low alginate concentrations (c < 5 g/L), we cannot deduce the relaxation time from the flow curves because the shear-thinning effect is decayed towards higher shear rates, meaning that the relaxation time is lower than 0.001 s. As for the solution of interest (c = 13.1 g/L), looking at the flow curve we can estimate the relaxation time to be $\tau_0 = 1/50 \approx 0.02$ s, consistent with the one obtained from oscillatory measurements. In fact, a frequency sweep test at 1% strain is performed on the alginate solution at 13.1 g/L and is shown in Figure 2.14. At low angular frequencies, the loss modulus is higher than the elastic modulus, meaning that the solution has mainly a viscous behavior. At $\omega_c \approx 40$ rad/s, G' and G" meet, giving rise to the relaxation time of the solution: $\tau_0 = 1/\omega_c \approx 0.025$ s, similar to the previous value. At frequencies higher than ω_c, the solution is elastic as G' is higher than G".

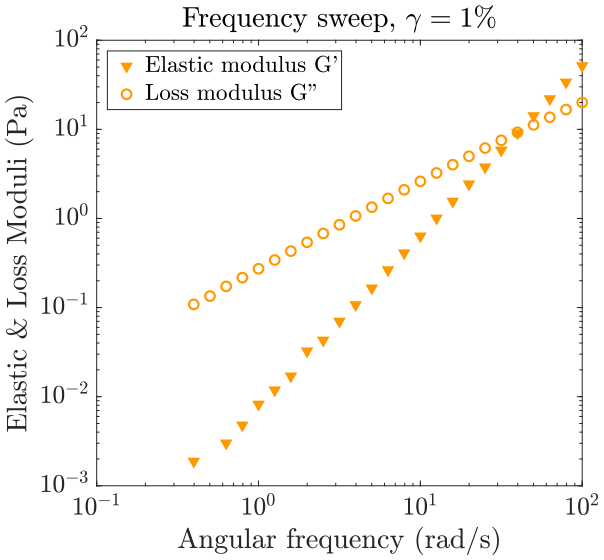

Figure 2.14 *Frequency sweep tests on alginate solution (M_w = 250 kg/mol, [alginate] = 13.1 g/L): elastic (G') and loss (G") moduli against angular frequency ω.*

For each solution, the specific viscosity is obtained with $\eta_w = 10^{-3}$ Pa.s (water viscosity) and η_0, the zero-shear plateau viscosity from the flow curves in Figure 2.13. The specific viscosity is then plotted against alginate concentration and the result is shown in Figure 2.15. A change of slope is observed, as predicted in the literature (see Figure 2.4). According to the theory values, for low-salt samples, the crossover between the semi-dilute entangled regime ($\eta_{sp} \sim c^{1.5}$) and the concentrated regime ($\eta_{sp} \sim c^{3.75}$) defines the overlap concentration c^{**} of electrostatic blobs. Above this concentration, the

electrostatic interactions no longer disturb the conformation of the chains, and polyelectrolytes in good solvent behave like entangled neutral polymers in good solvent for which $\eta_{sp} \sim c^{15/4}$ [6, 11].

For our solutions of long chain alginates, the data show a slope going from a value of 1.8 (which is a little bit higher than 1.5 predicted by theory) to 3.75, we can thus determine the crossover concentration to be $c^{**} \approx 6.6\ g/L$ (see Figure 2.15). In fact, for low concentrations, conductivity measurements lead us to believe that alginates are weakly charged hence the comparison with the scaling theory for weakly charged polyelectrolytes. The observed difference between the exponents (1.8 and 1.5) can be due to alginate's high polydispersity. In fact, a large polydispersity can yield a higher apparent exponent due to the coexistence of chains in the dilute and semi-dilute regions [10].

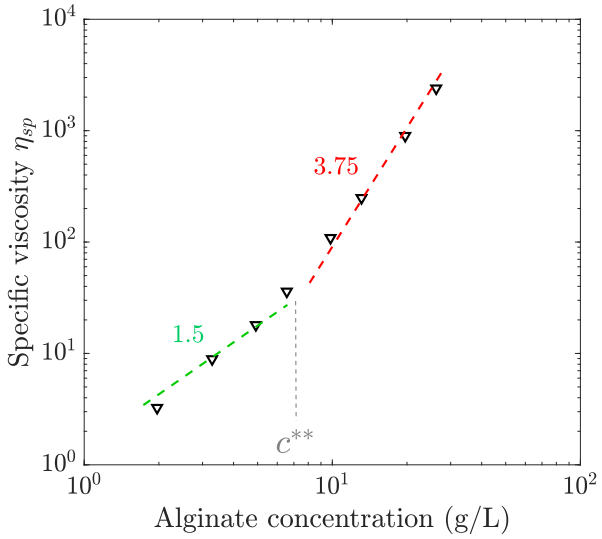

Figure 2.15 *Specific viscosity against 250 kDa alginate concentration (in g/L).*

b) Shorter alginate chains (M_w = 60 kg/mol)

This same analysis is then done on shorter alginate chains (60 kg/mol), which we obtain by applying a thermal treatment to long alginate chains (see Section 2.2.4). In that case, the concentration range studied is larger: from 2 g/L to approximately 115 g/L. Flow curves are shown in Figure 2.16.

We observe that all the flow curves show a viscosity plateau, without shear thinning. This is due to the fact that alginate chains are smaller, so they disentangle and re-entangle

rapidly upon shearing, which means that for each solution, the relaxation time is very small ($\tau_0 < 10^{-3}$ s) and inaccessible from the flow curves.

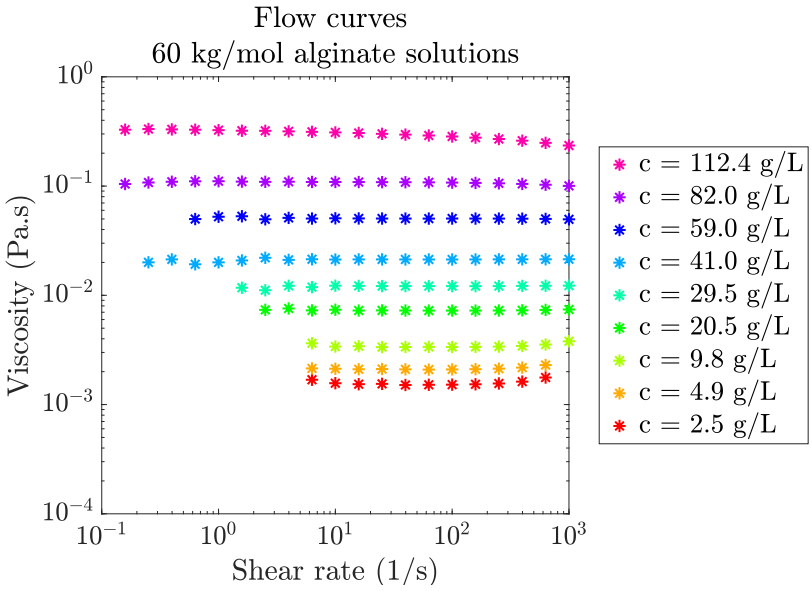

Figure 2.16 *Flow curves: evolution of viscosity as a function of shear rates for different 60 kg/mol alginate solutions in the presence of PAA.*

The specific viscosity is plotted against alginate concentration in Figure 2.17. From this curve, we can determine the overlap concentration $c^* \approx 5\ g/L$, at the intersection between the slope values of 1.0 and 1.3. This value is consistent with the one obtained from the measure of intrinsic viscosity (IV) by SEC in Section 2.2.4.a) : IV = 1.85 dl/g giving $c^* \approx 1/IV \approx 5.4\ g/L$. The next change of slope determines the entanglement concentration $c_e \approx 55\ g/L$ at the crossover of $\eta_{sp} \sim c^{1.3}$ and $\eta_{sp} \sim c^{3.75}$. These values are consistent with the ones predicted by Lopez et al. [10] for highly charged polyelectrolytes. In fact, at high concentrations, the solutions of short alginate chains show high conductivity values (not shown), justifying the use of scaling theory for high salt concentration.

These results highlight that in the main suspensions studied (described in Table 2.1), the alginate chains are in the entangled regime (c > c_e for suspension D) and over the blob overlap concentration c^{**} for M_w = 250 kg/mol (i.e. suspensions A, B and C). Knowing that, we need to characterize the behavior of these solutions in the presence of zirconia particles.

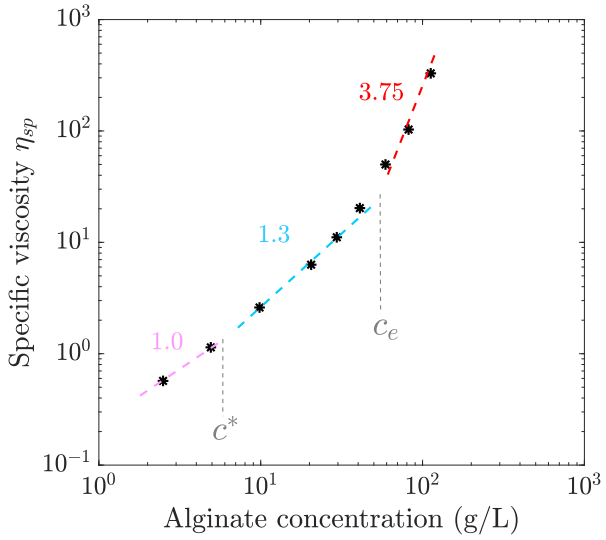

Figure 2.17 *Specific viscosity against 60 kDa alginate concentration (in g/L).*

2.5.3 Zirconia - alginate suspensions

a) Influence of alginate concentration on flow behavior

As mentioned earlier in Table 2.1, three main suspensions are formulated with sodium alginate of molecular weight M_w = 250 kg/mol, keeping the zirconia fraction constant ($\phi_{w,Zir}$ = 40%*wt*). The reference suspension (A) has an alginate concentration of 13.1 g/L (i.e. $\phi_{w,Alg}$ = 0.8%*wt*). Two other suspensions were made with half and double the alginate content. As shown in Figure 2.18 (a), they all exhibit a similar shear-thinning behavior with a growing overall viscosity as the alginate concentration increases.

By plotting the shear stress against the shear rate, the data at low shear rate values can be fitted by a Herschel-Bulkley model (see Equation (2.5)), showing a yield-stress value σ_0. As illustrated in Figure 2.18 (b), the suspensions have very low yield-stress values, which is interesting for the droplets shape evolution as we will discuss later in Chapter 5.

$$\begin{aligned} \sigma &= \sigma_0 + K\,\dot{\gamma}^m \\ \eta &= K\,\dot{\gamma}^{m-1} \end{aligned} \tag{2.5}$$

where σ represents the shear stress, η the viscosity, K is the fluid consistency and m the flow index.

To verify the yield-stress value given by the flow curves and the Herschel-Bulkley fit, we perform oscillatory rheological measurements (strain sweep at 1 rad/s) on these

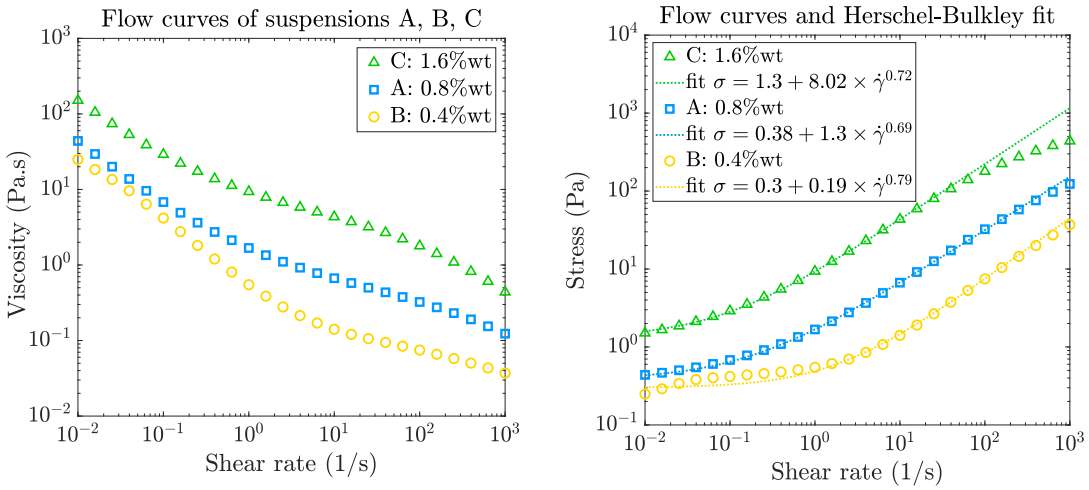

Figure 2.18 *Flow curves for the three main suspensions A, B and C containing 250 kg/mol alginate at 0.4%wt, 0.8%wt and 1.6%wt respectively. (a) Viscosity against shear rate. (b) Stress against shear rate. Experimental data at low shear rates fitted with Herschel-Bulkley model* $\sigma = \sigma_0 + K\dot{\gamma}^m$.

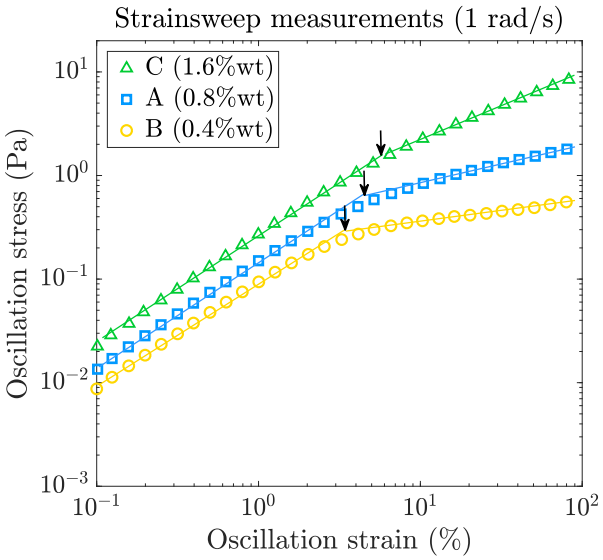

Figure 2.19 *Strain sweep measurements on suspensions A, B and C: oscillation at 1 rad/s with a varying strain amplitude from 0.1% to 100%.*

suspensions. We then plot the resulting oscillatory stress against the oscillatory strain and the change of slope gives access to the yield-stress value σ_0 as illustrated by the black arrows in Figure 2.19. We obtain very similar yield-stress values as the ones from the previous fit. The Herschel-Bulkley parameters are summarized in Table 2.2.

Name	Suspension	Yield-stress σ_0	Consistency K	H-B exponent m
A	0.8%wt	0.38	1.3	0.69
B	0.4%wt	0.3	0.19	0.79
C	1.6%wt	1.3	8.02	0.72

Table 2.2 *Summary table of Herschel-Bukley parameters for the three main suspensions A, B and C (with M_w = 250 kg/mol): $\sigma = \sigma_0 + K\dot{\gamma}^m$.*

b) Understanding the yield-stress behavior

We have shown that alginate solutions behave like Newtonian fluids, with a constant viscosity upon shearing, while zirconia suspensions behave like yield-stress fluids. In Figure 2.20, we exhibit the comparison between suspension A containing 40%wt zironia, PAA and 0.8%wt alginate (i.e. 13.1 g/L) and a solution containing only alginate (at 13.1 g/L) and PAA. As discussed previously, the entangled alginate solution shows a shear thinning behavior at high shear rates when the chains disentangle and align with the flow. But adding zirconia particles increases tremendously the viscosity at low shear rates.

This points out an interaction between zirconia particles and the alginate matrix. We suggest that adding alginate into the grinded suspension leads to an attraction between zirconia grains to form a **colloidal gel**, resulting in an increase of viscosity. At rest, the suspension is viscous whereas under high shear rates, the viscosity decreases strongly. We notice that the two curves superimpose at very high shear rates which can be explained by the fact that at these deformation rates the gel structure is totally broken and the grains are not in contact anymore, hence the alginate chains control the rheological measurements. There are two possible cases for the flocculation of zirconia particles with the addition of alginate:

- **Bridging**: one alginate chain adsorbs on several zirconia particles, making bridges between them.
- **Depletion interactions**: assuming that the alginate chains don't adsorb on the zirconia particles (since they are already protected by PAA), they can create depletion

forces leading to the formation of zirconia aggregates.

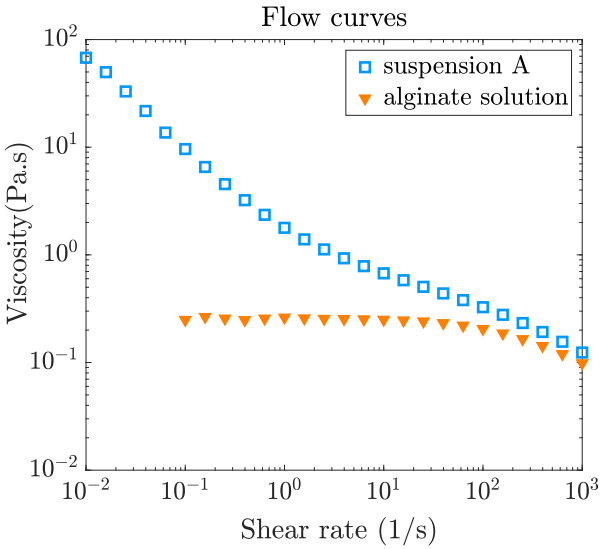

Figure 2.20 *Comparison between the flow behaviors of an alginate solution at 13.1 g/L and the suspension A ([zirconia] = 40%wt, [alginate] = 13.1 g/L).*

To determine which type of interaction exists between zirconia particles and alginate, we perform shear rate increments on a sample of suspension A and we measure the viscosity during each shear rate step. These experiments were performed with varying shear rate increments and different rest time (from 0 to 60 s) between the two shear steps. One of these experiments is shown in Figure 2.21 as an example. We observe that for a given shear rate, the viscosity reaches quickly (in 0.1 s) its equilibrium value (identical to the one of the flow curve studied before in Figure 2.20 and independent of the rest time). We expect more reversible and rapid restructuring in the case of depletion interactions thus suggesting such depletion forces in our alginate-zirconia suspensions.

Another way to verify our hypothesis is to perform rheological oscillatory measurements on suspensions with different zirconia volume fractions (while keeping the same alginate concentration 13.1 g/L). The result is presented in Figure 2.22 where the elastic modulus G' is plotted against zirconia volume fraction ϕ. The log-log scale gives us a slope $n = 2.93$ which corresponds to a depletion-flocculated system according to the literature [23–25]. Therefore, when we add alginate in the system, zirconia particles probably form a colloidal gel by depletion interactions. Upon shearing, the flocculated structure breaks, zirconia particles align with the flow and the alginate chains disentangle, leading to a decrease of viscosity as seen in Figure 2.20.

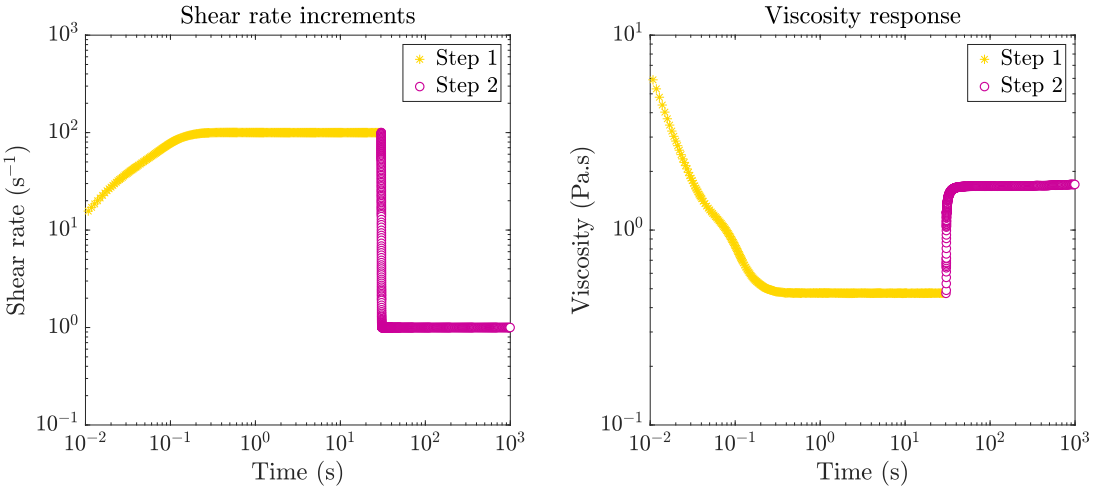

Figure 2.21 *Successive shear rate steps (step 1: $\dot{\gamma}$ = 100 s^{-1} and step 2: $\dot{\gamma}$ = 1 s^{-1}) applied on the suspension A (0.8%wt alginate). (a) Shear rate increments applied. (b) Viscosity response.*

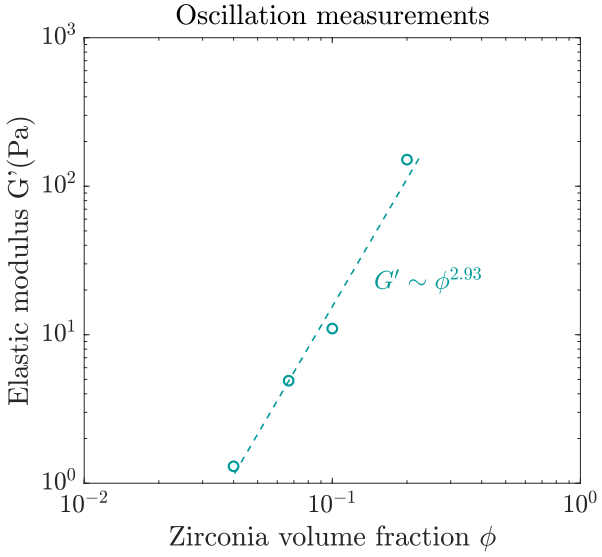

Figure 2.22 *Oscillatory measurements: strainsweep protocol at 1 Hz on suspensions with varying zirconia volume fraction ϕ.*

c) Controling the yield-stress behavior with alginate M_w

Another way to change the suspension rheological behavior is to reduce the molecular weight of sodium alginate by thermal treatment as explained in Section 2.2.4. Several suspensions are made with varying alginate concentrations but the main one on which we will focus is suspension D containing 5%wt of 60 kg/mol alginate (i.e. a volumic concentration $c \approx 82\ g/L$) and the same zirconia content of 40%wt. Interestingly, this suspension (D) has a rheological behavior evolving with time as shown in Figure 2.23 (a). When it is freshly formulated, the suspension exhibits a shear-thinning behavior with a small yield-stress value similarly to the suspensions A, B and C studied previously. So, in the same way, when we add alginate in the suspension, we suggest that the zirconia particles are depleted and form a colloidal gel structure. But after 48 hours, the suspension D shows a completely different behavior: it becomes quasi-Newtonian, with a flow curve very similar to those of alginate solutions without particles.

The same phenomenon is observed for suspensions containing alginate concentrations of 4%wt, 3.5%wt and 3%wt (at M_w = 60 kg/mol) as seen in Figure 2.23 (b - d). To describe this evolution, we suggest that at long time scales, a desorption / adsorption equilibrium of PAA and small alginate chains at the interface of zirconia particles is reached. Therefore, some of the alginate chains may play a dispersing role, as well as PAA, to deagglomerate zirconia grains and redisperse them in the entangled alginate network [17]. This hypothesis was not tested experimentally, as mentioned earlier, by lack of time and due to the difficulty of the experiments required (adsorption isotherms by TOC coupled with dialysis to separate PAA from alginate).

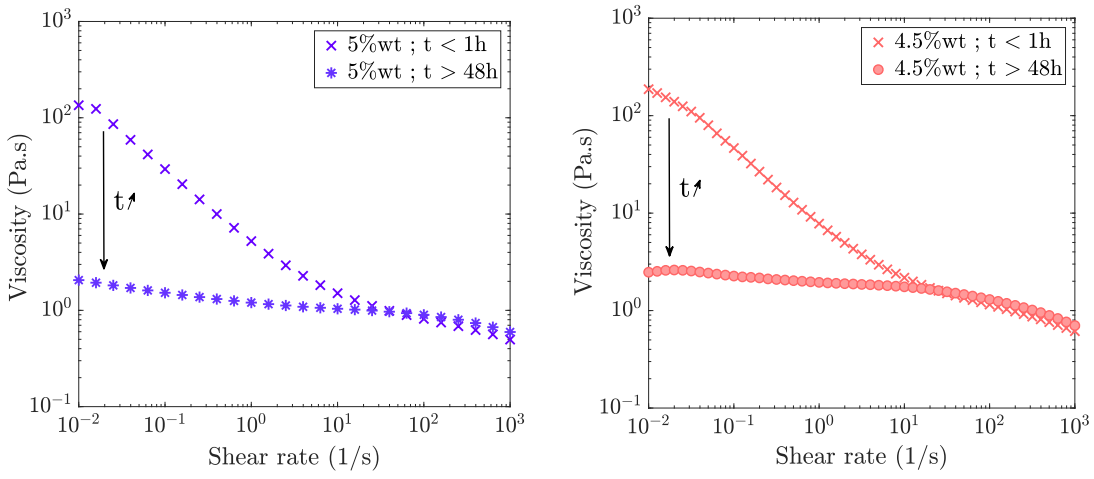

(a) (b)

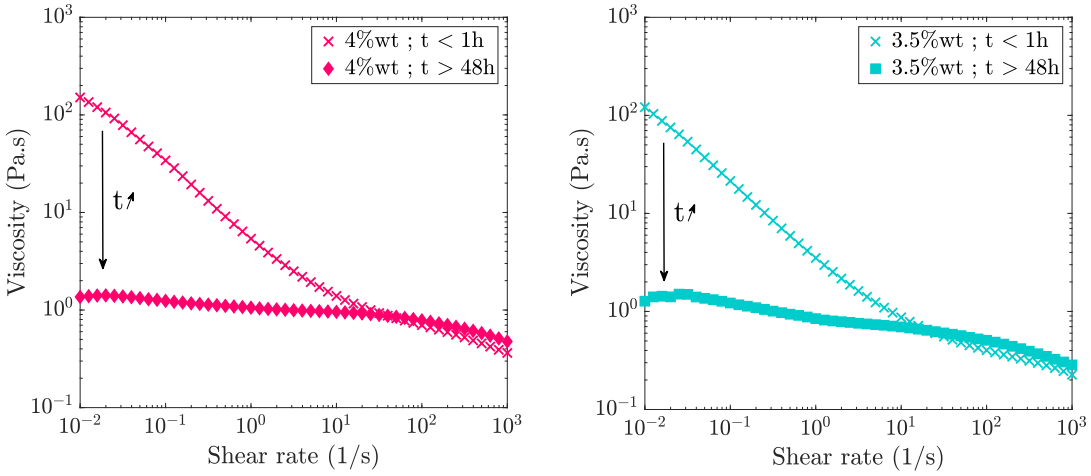

Figure 2.23 *Evolution of flow curves with time: viscosity against shear rate for fresh suspensions (t < 1 h) and older ones (t > 48 h) with varying alginate concentrations: (a) 5%wt ; (b) 4.5%wt ; (c) 4%wt ; (d) 3.5%wt. In all cases, M_w = 60 kg/mol.*

2.6 Conclusion

This chapter was dedicated to the rheological characterization of alginate solutions and alginate-zirconia suspensions. In fact, during the drip-casting process, the suspension undergoes different states as it is sheared at various rates from the syringe to the nozzle and through its impact on the liquid bath.

In order to cover a wide range of rheological properties, four main suspensions have been formulated and characterized, each containing the dispersing agent PAA, covering entirely the surface of zirconia particles to ensure their stabilization. Suspensions A, B and C contain 40%wt zirconia and sodium alginate of molecular weight M_w = 250 kg/mol at different concentrations: 0.8%wt, 0.4%wt and 1.6%wt respectively. They all exhibit a shear-thinning behavior and a low yield-stress, probably due to the depletion-induced formation of zirconia aggregates in the entangled alginate matrix. When the applied shear rate increases, the colloidal gel structure breaks, resulting in the decrease of viscosity.

The last suspension (D) contains the same amount of zirconia (40%wt) but a lower molecular weight alginate (M_w = 60 kg/mol) of concentration 5%wt. The resulting suspension has a totally different rheological behavior. Indeed, it shows a shear-thinning behavior just after formulation, similarly to the previous suspensions, but after 48 h, it

becomes almost Newtonian. This may be due to the adsorption of small alginate chains onto the surface of zirconia, leading to the formation of a stabilization layer preventing the particles from flocculating.

By changing the alginate concentration or molecular weight, we are able to cover a wide range of rheological properties, from yield-stress fluids to Newtonian behaviors. This will enable us to determine how the rheological properties control the impact and relaxation behaviors of the droplets.

Take-home messages of chapter 2

- Alginate solutions without particles behave like Newtonian fluids.
- Zirconia suspensions without alginate have a very low viscosity, similarly to water.
- Suspensions A, B and C containing long alginate chains (M_w = 250 kg/mol) at a concentration of 0.8%wt, 0.4%wt and 1.6%wt respectively exhibit a yield-stress σ_0 = 0.4, 0.3 and 1.3 Pa respectively. This shear-thinning rheological behavior suggests that adding long alginate chains to zirconia suspensions probably causes the particles to agglomerate due to depletion interactions.
- Adding alginate chains of molecular weight M_w = 60 kg/mol to zirconia suspensions also leads to a yield-stress. But after a rest time of 48 h, the resulting suspension behaves like a Newtonian fluid. We suggest that this change of behavior is due to a stabilization of zirconia particles by the adsorption of small alginate chains onto their surface.

Chapter 3

Gelation mechanism & bead characterization

During the drip-casting process, once the suspension is formulated, it is dripped into a calcium bath where it starts to gel. In this chapter, we study the gelation of alginate solutions and zirconia suspensions, which, as will be explained in Chapter 5, is key to understand the shape evolution of droplets. First, the gelation reaction as well as the evolution of the gelled membrane thickness are examined and quantified regarding different parameters. Then, the mechanical properties of the gelled beads are studied.

3.1 Polyelectrolyte gels: state of the art

3.1.1 Alginate beads

Alginate-calcium gels in the shape of capsules are widely used in cosmetics, pharmaceutics, food industry and biology for diverse applications [36–47]:

- Immobilization and isolation: for instance, two reactive compounds can be separated and stored in alginate capsules and put in contact when the capsules break.
- Protection: the encapsulated compounds can be isolated from the environment and thus stabilized preventing their oxidation or evaporation for example.
- Control the release of active compounds: once inside a capsule, they can be released by mechanical or chemical degradation of the coating matrix. These objects can be used as transport vectors for active substances in cosmetics or pharmaceutics.
- Cell culture: cells can be immobilized within a semi-permeable alginate membrane allowing the bidirectional diffusion of molecules such as oxygen, nutrients and growth factors essential for cell metabolism as well as the outward diffusion of waste products and/or therapeutic proteins. The 3-dimensional cell culture through alginate encapsulation provides a good tool to reproduce the observed behaviors in vivo while the conventional cell culture techniques (in Petri dish) only form bi-dimensional structures, far from reality.

The simplest way to obtain alginate beads is to use the dripping process. A drop of alginate solution falls down into a liquid bath containing divalent cations such as Ca^{2+} ions. Alginate chains react with these cations to form a hydrogel.

3.1.2 Alginate gelation properties

Egg-box model In the presence of divalent cations such as Ca^{2+} ions, ionic bonds can be formed between the carboxylate groups and the calcium ions. Thanks to their conformation, G-blocks of different alginate chains form negative cavities in which calcium ions can accommodate as illustrated in Figure 3.1. This intermolecular cross-linking in the shape of "egg-box" structures [48, 49] give rise to a physical ionotropic gel. There

are two types of alginate gelation. The first one, **internal gelation**, consists in delaying the gelling reaction: $CaCO_3$ and D-glucono-δ-lactone (GDL) are added to the alginate solution. The GDL hydrolysis starts slowly, which reduces the pH and favors the in-situ release of Ca^{2+} ions. In that case, the gelation is slow and controlled by the amount of $CaCO_3$ and GDL. In the literature, the internal gelation is more commonly used as it leads to more homogeneous gels with a precise quantity of Ca^{2+} inside. The other method, **external gelation**, is used in the encapsulation process: the alginate solution is directly put in contact with an excess of Ca^{2+} and the gelation is very rapid. In fact, as soon as a droplet of alginate reaches the $CaCl_2$ bath, a gelled membrane is formed at its surface. This extremely rapid cross-linking is usually accompanied by a deswelling of the gelled bead. This phenomenon is known as syneresis.

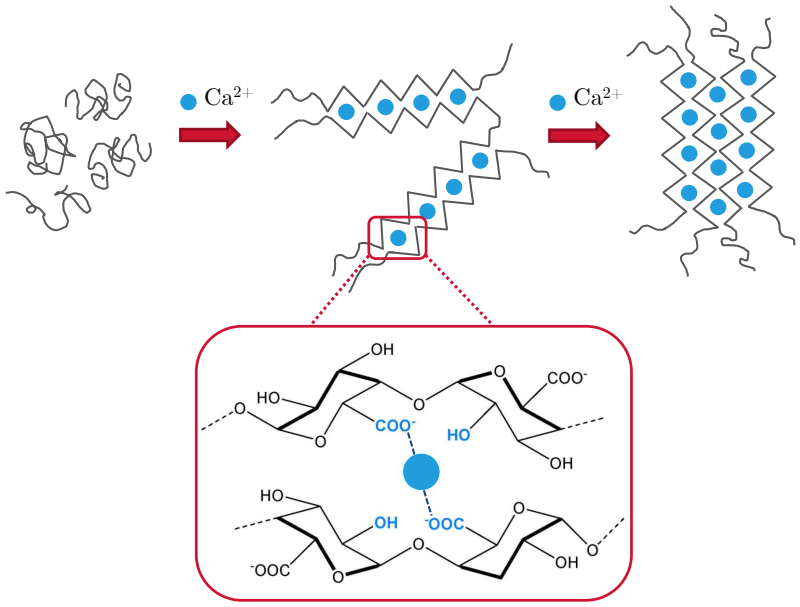

Figure 3.1 *Alginate gelation: the egg-box model.*

Syneresis Syneresis is a process during which the network of the gel contracts and expels the interstitial liquid [50, 51]. It is a phenomenon commonly observed over time in various systems undergoing a sol-gel transition and often represents a challenge in the manufacturing of food gels [52]. Syneresis is produced by osmotic forces arising from the difference in affinity between the polymer chains and the solvent. In particulate gels, the structure is controlled by the balance between electrostatic repulsion and attractive van der Waals forces, so the extent of shrinking is controlled by the presence of electrolytes.

In our case, a droplet containing particles (zirconia) and polyelectrolytes (alginate and PAA) is immersed into a bath containing an excess of calcium ions. As Ca^{2+} ions diffuse inside the capsule, alginate chains are bonded two-by-two creating egg-box structures as explained in the previous paragraph. Then, these dimers combine with each other to form multimers [53] and so on. This gelation reaction thus consumes hydrophilic monomers and by reducing the distance between the alginate chains, there is less space for water molecules which therefore need to diffuse out of the gelling structure. More generally, syneresis occurs via reorganization of the micron-size aggregates in the gel [52]. There are very few studies on the quantification of this phenomenon in alginate gels and even less on alginate beads. However it has been reported that in the case of internal gelation, the degree of syneresis is strongly related to the amount of Ca^{2+} ions present in the system [54]. Draget et al. [51] showed that the gel contraction is also related to the chemical structure (M/G ratio) and size (molecular weight) of alginate chains. The higher the amount of G-blocks and the higher the molecular weight M_w, the greater the gel deswelling. This will further be discussed in the next part.

3.2 Experimental investigation of the gelation process

3.2.1 Preliminary observations of syneresis

In order to observe the syneresis, the experiment illustrated in Figure 3.2 is conducted. Approximately 6.5 g of suspension is placed in a small beaker and 20 mL of calcium chloride solution (at 158 g/L) is poured on top of it. As the suspension solidifies, we see wrinkles on its surface, suggesting that the gel contracts and looses volume. In the end, the gel cylinder is detached from the sides: its section is smaller than the beaker's, proving the overall contraction. To confirm this volume loss, we perform weight measurements on these macroscopic gels (not shown).

To visualize this phenomenon at the bead scale during the drip-casting process, we change the lighting and the camera diaphragm opening. Thanks to the difference of refractive index between the expelled water and the highly concentrated calcium bath, we are able to observe the rejected pure water as shown in Figure 3.3. Indeed, as the capsule starts to gel, water is expelled and rises to the surface of the bath because of its lower density (1 versus 1.1 the density of the highly concentrated calcium bath).

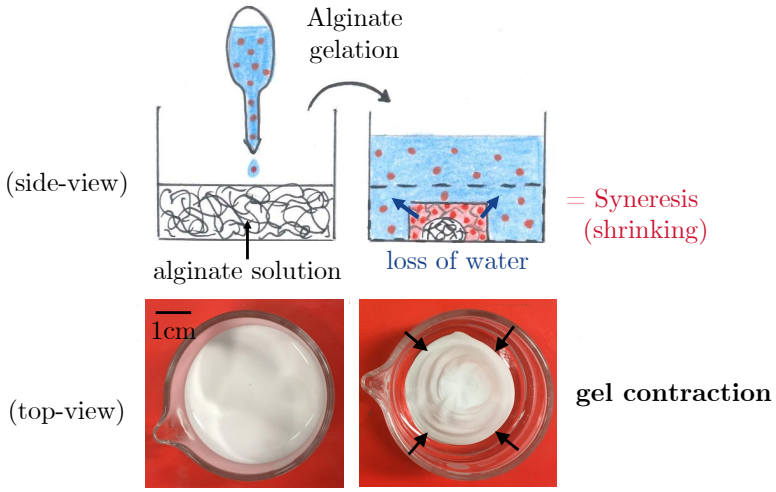

Figure 3.2 *Experiments revealing the syneresis phenomenon. 6 g of reference suspension is placed in a small beaker and 20 mL of calcium bath is poured on top of it. The gel contraction is visible.*

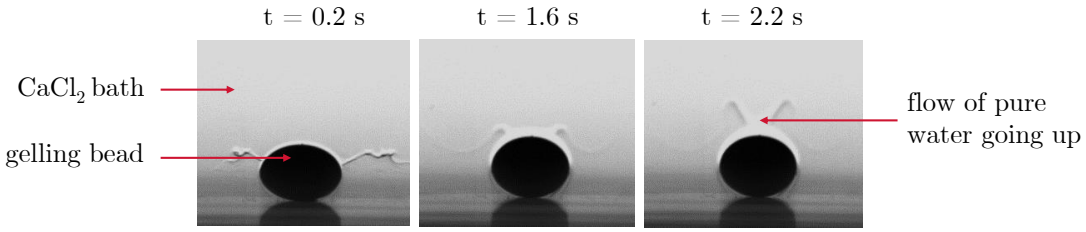

Figure 3.3 *Image sequence of a gelling bead: reference suspension (0.8%wt alginate) gelling in a calcium bath at [$CaCl_2$] = 158 g/L.*

3.2.2 Quantification of syneresis

As mentioned in Section 3.1.2, the shrinkage is controlled by the presence of ions (counterions or added salt), inorganic particles and alginate as well as their concentrations. Palluault [53] observed the syneresis phenomenon but did not quantify it. He drew a phase diagram describing the visual aspect of the gel (continuus or phase separated) as a function of alginate and Ca^{2+} concentrations for internal gelation. Very few articles [51, 54, 55] studied quantitatively the gel contraction by measuring the final gel weight with respect to the initial weight of the alginate solution. All these studies were made on internally prepared Ca-alginate gels (with a homogeneous slow gelation process according to the method of Skjak-Braek et al. [56]). However, there are no dynamic measurements of syneresis phenomenon on fast gelling (out of equilibrium) alginate

beads exposed to a surplux of Ca^{2+} (i.e. external gelation).

To quantify the gel contraction in our case, we perform weight measurements over time on gelling beads under different conditions. To do so, a droplet of zirconia-alginate suspension (or alginate suspension without particles) of initial weight m_0 is dripped into a $CaCl_2$ bath. At different gelling times, we take the capsule out of the bath and weigh it after having gently wiped off the excess of water around it. We then put it back into the gelling bath and repeat the operation in order to follow the bead's weight evolution with time.

Overall, the weight loss measurements that will be presented in the following pages seemed counter-intuitive at first. They led us to build a qualitative frame for the interpretations, that we explain now. Then, we will discuss our results within this frame. Due to the large amount of ions present in our system (in the bath and inside the capsule), we suggest that the bead weight measurements are a result of the **competition between different flows**, as depicted in Figure 3.4. The first one is the osmotic water expulsion from the gelling membrane due to the bridging of alginate chains (i.e. syneresis). The second one is another osmotic flow, inward or outward, due to the difference of ion concentration between the capsule core (Na^+ and NH_4^+) and the outside bath (Ca^{2+}). In fact, as soon as the droplet reaches the calcium bath, a thin gelled membrane is formed around the liquid core. This gel crust is semi-permeable and plays the part of a dialysis membrane allowing the flow of water and ions through it [6, 57] to redistribute the charges on both sides of the membrane.

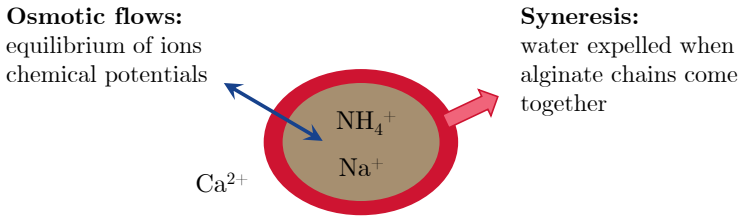

Figure 3.4 *Schematics of the two main osmotic flows. On the left, water entry / exit due to a difference of ion concentration between the capsule core and the bath. On the right, syneresis: water expulsion due to gel contraction when the egg-box structures are forming.*

Dobrynin et al. [6] gave a scaling model for the osmotic pressure of polyelectrolytes by expressing the total osmotic pressure as the sum of the ionic and polymeric contributions: $\Pi = \Pi_i + \Pi_p$ where $\Pi_p \approx \frac{kT}{\xi^3}$ (ξ^3 being the correlation volume in semi-dilute polymer

solutions). But, as explained in Section 2.1.3, for the vast majority of systems studied, the ionic contribution dominates the osmotic pressure of polyelectrolytes. Therefore, in the rest of the manuscript, we will only consider the osmotic pressure to be $\Pi = \Pi_i$ and using Equation (2.1), we can write:

$$\Pi = RT \times (c_{in} - c_{out})$$

where R is the gas constant, c_{in} and c_{out} are the ions concentrations (in mol/L) inside and outside the capsule. For each case, we need to calculate the effective concentrations by adding the contributions of all ions in the system. Inside, there are mainly the alginate and dispersant PAA counterions, respectively Na^+ and NH_4^+, whereas outside, there are the calcium ions of the bath Ca^{2+}. To summarize, the weight loss measurements are the result of the addition of a volume loss due to syneresis (from the membrane to the bath) and a swelling or deswelling of the liquid core due to the ion concentration difference between the inside and the oustide of the capsule.

a) Effect of alginate concentration

First, we study the influence of alginate concentration by measuring the weight loss of approximately 3 mm droplets containing only alginate, PAA and water (without zirconia particles to simplify) as they fall into a highly concentrated calcium bath ($[CaCl_2]$ = 158 g/L). As illustrated in Figure 3.5, the gelation of the capsule is accompanied by a slow, time-dependent deswelling (weight loss). Taking the equilibrium value at t $\approx$ 1500 *s*, we observe that the lower the alginate content, the higher the gel contraction.

This result can be explained taking into account both osmotic flows mentioned previously. First, in terms of syneresis, if the capsule is more diluted, there is initially more water to expel in order to form a dense gel structure (where all the polymer chains come together and form the "egg-box" multimers). Thus, a higher amount of water can be expelled by syneresis. Then, we can calculate the ion concentrations inside and outside the gelling drop. Outside, we have $[Ca^{2+}]$ = 158 g/L = 1.4 mol/L. Inside, the PAA (i.e. NH_4^+) concentration is kept constant equal to 0.06 mol/L whereas the alginate (i.e. Na^+) concentration varies from $[Na^+]$ = 4.9 g/L = 0.025 mol/L to $[Na^+]$ = 26.2 g/L = 0.13 mol/L. Consequently there is an excess of ions outside the capsule, which leads to an outward flow of water. The lower the ion concentration inside, the higher the osmotic pressure and so the greater the outward flow, resulting in a greater water loss, which

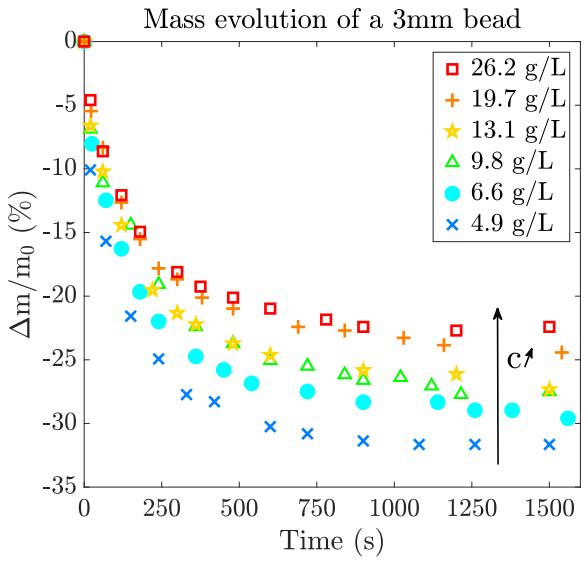

Figure 3.5 *Weight loss measurements on 3 mm gelling beads with varying alginate (250 kg/mol) concentrations (from 5 g/L to 27 g/L) without zirconia particles in a calcium bath of concentration 158 g/L.*

is summarized in Figure 3.6. Therefore, combining both flows, we understand that the beads experience an overall weight loss, and the higher the alginate concentration, the lower this weight loss.

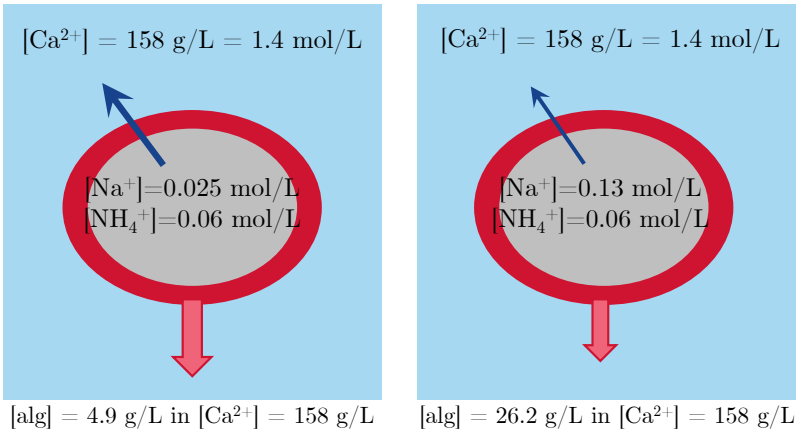

Figure 3.6 *Osmotic flow competition for an alginate bead of concentration 4.9 g/L (on the left) and 26.2 g/L (on the right) in a bath of concentration* $[Ca^{2+}] = 158$ *g/L.*

b) Effect of zirconia addition

Adding particles changes the deswelling of the beads (see Figure 3.7). We compare beads of same alginate concentration, 6.6 g/L (a) or 13.1 g/L (b), to which we add (or not) 40%wt zirconia particles. We observe a greater weight loss in the alginate beads without particles. If we calculate the ion concentration inside and outside the capsule, it does not change with the addition of zirconia and neither does the outward flow of water. The extent of syneresis, however, seems to be smaller by the addition of zirconia particles. The first possible explanation is linked to the amount of water initially present in the capsule. Quantitatively, knowing the zirconia content in the suspension (40%wt, i.e. approximately 15%vol), we can admit that there is 15%vol less water in the suspension compared to the alginate solution of same concentration. Consistently to the weight loss measurements, we find that the zirconia-alginate gels loose approximately 15% less water than the pure alginate gels. We suggest another plausible interpretation for the decrease of syneresis, taking into account the capsule microstructure: the gel bead may be limited in its contraction by the presence of the flocculated network of zirconia particles, resulting in a smaller syneresis flow.

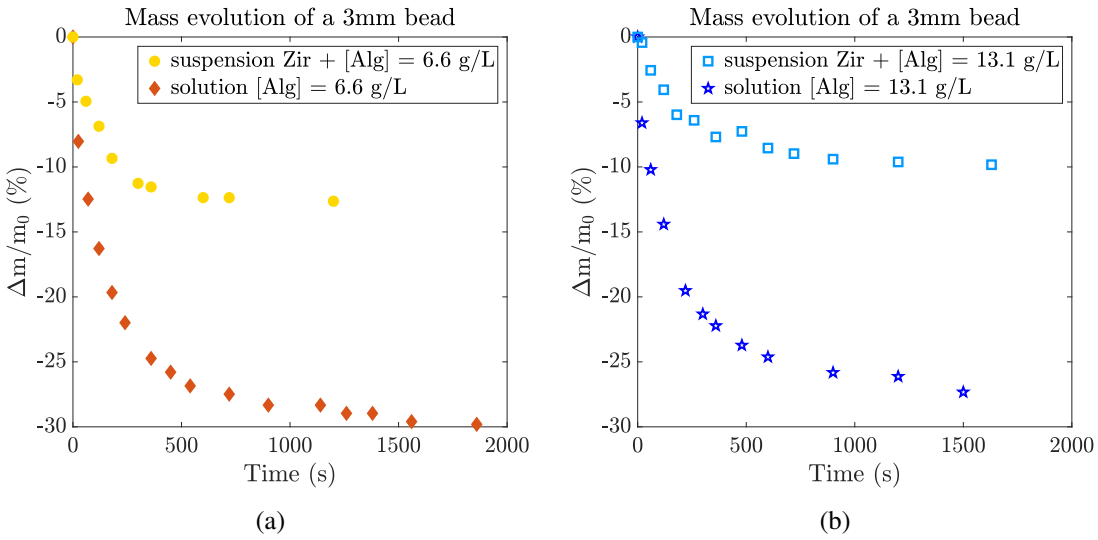

Figure 3.7 *Weight loss measurements on 3 mm gelling beads in a calcium bath of concentration 158 g/L. Influence of particle content on syneresis. (a) [alginate] = 6.6 g/L. (b) [alginate] = 13.1 g/L. In all cases, M_w = 250 kg/mol.*

c) Effect of calcium concentration

Referring to literature [50, 51, 53], the syneresis phenomenon strongly depends on the electrolyte concentration (mostly calcium ions in our case) because it is a consequence of chain bridging (egg-box formation) by calcium ions. We conduct weight loss measurements on zirconia suspension beads (with 60 kg/mol and 250 kg/mol sodium alginate) in several baths to quantify the effect of calcium concentration on osmotic flows.

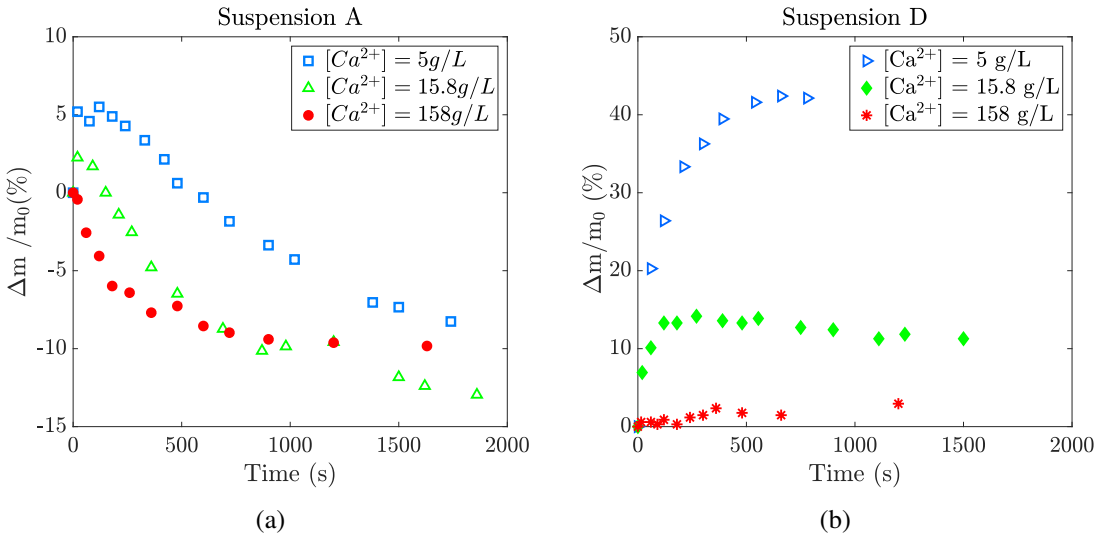

Figure 3.8 *Weight loss measurements on beads of alginate - zirconia suspensions gelling in different calcium baths. (a) Suspension A: [alginate] = 0.8%wt, M_w = 250 kg/mol. (b) Suspension D: [alginate] = 5%wt, M_w = 60 kg/mol.*

In Figure 3.8, we follow the weight evolution of gelling zirconia-alginate beads with different alginate concentration and molecular weight, in varying calcium baths [Ca^{2+}] = 158 g/L, 15.8 g/L and 5 g/L (i.e. 1.4 mol/L, 0.14 mol/L and 0.045 mol/L respectively). Knowing the concentrations of all the components, we can calculate the ions concentration inside (c_{in}) and outside the capsule (c_{out}) for each case and draw the direction of the resulting osmotic flow. Combining it with the syneresis flow, we aim at explaining the observed deswelling or swelling of the beads.

First, we consider a bead of suspension A (containing 40%wt zirconia and 0.8%wt of 250 kg/mol alginate). Looking at Figure 3.8 (a), we observe that the higher the calcium concentration, the sooner the weight loss. For the bath at 5 g/L, the capsule exhibits a weak swelling at short time scales, before deswelling at longer time scales. However, the overall weight loss in the end is similar for the three cases. In order to explain these

curves, let us first calculate the ions concentration inside and outside the gelling drop. We have $[NH_4^+]$ = 0.06 mol/L and $[Na^+]$ = 0.07 mol/L so the effective ion concentration inside is $c_{in} \approx$ 0.13 mol/L (see Figure 3.9).

- Bath $[CaCl_2]$ = 158 g/L = 1.4 mol/L: in that case, the ion concentration inside the capsule is lower than the one of the bath so there is a flow of water diffusing out the liquid core of the capsule. Moreover, the gelation is very fast at this high calcium concentration so the syneresis is also rapid. Both flows add up which results in a global weight loss of the bead.

- Bath $[CaCl_2]$ = 15.8 g/L = 0.14 mol/L: the ion concentrations inside and outside the droplet are equivalent so the main flow into consideration is the syneresis due to the gelation of the membrane. Since Ca^{2+} concentration is lower than in the previous case, the syneresis is slower because the gel crust grows slower. That is why, at the bead scale, we see a global weight loss decayed from the previous curve.

- Bath $[CaCl_2]$ = 5 g/L = 0.045 mol/L: in that case, the liquid core swells because of its higher ion concentration while the syneresis flow is too small to be competitive because the gelling membrane grows much slower, which results in an overall swelling of the bead. But after 500 s, we suggest that the membrane is thick enough to ensure a sufficient gel contraction, and the syneresis flow becomes predominant so the bead looses weight.

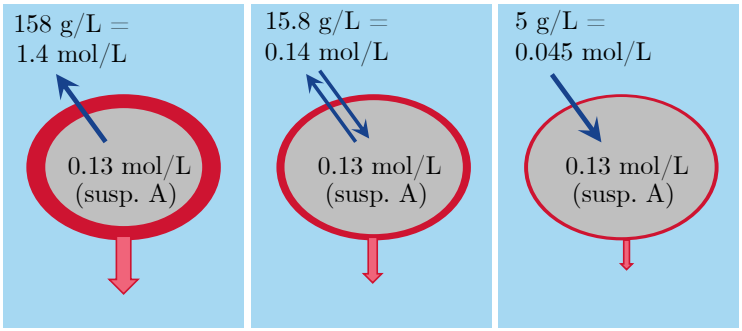

Figure 3.9 *Suspension A ([alg] = 13.1 g/L, M_w = 250 kg/mol) gelling in different baths. Competition between syneresis flow (gel membrane) and osmotic flow (liquid core).*

Then, the same experiments are performed on beads of suspension D containing 60 kg/mol alginate at 82.0 g/L and the resulting curves are totally different as shown in Figure 3.8 (b). The beads swell enormously at low calcium concentration (5 g/L) whereas at high calcium content (158 g/L) they swell very slightly. In all cases, the beads swell rather than loosing water. This raises our attention, and lead us to believe that syneresis is lower (and negligible?) compared to osmotic effects due to ion concentration difference. With this composition, $[NH_4^+]$ = 0.06 mol/L and $[Na^+]$ = 0.42 mol/L so the effective ion concentration inside is $c_{in} \approx 0.48$ mol/L (see Figure 3.10).

- Bath $[CaCl_2]$ = 5 g/L = 0.045 mol/L: in that case, the ion concentration outside is much lower than the one inside, resulting in a very important swelling of the capsule, consistent with the weight increase observed.
- Bath $[CaCl_2]$ = 15.8 g/L = 0.14 mol/L: the ion concentration inside the droplet is still higher, explaining the water entry and the overall increase of the bead volume.
- Bath $[CaCl_2]$ = 158 g/L = 1.4 mol/L: in that case, the ion concentration inside the capsule is lower than the one of the bath so we expect a flow of water diffusing out the liquid core of the capsule. However, as there are many alginate chains, the calcium is rapidly consumed in the droplet, which creates a depletion zone around the droplet where Ca^{2+} concentration is much lower (represented in light blue). So, in reality the ion concentration just outside the capsule may be lower than the one inside, which could explain the slight overall swelling of the bead.

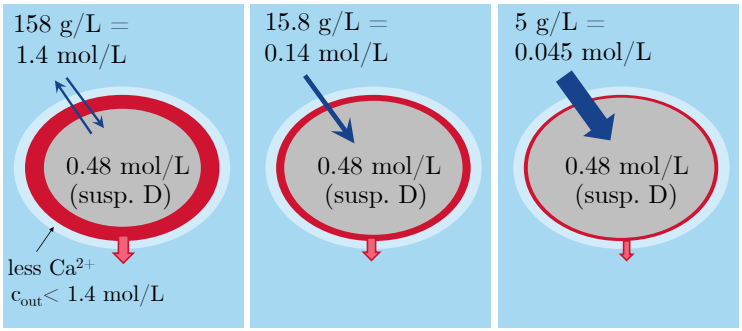

Figure 3.10 *Suspension D ([alg] = 82.0 g/L, M_w = 60 kg/mol) gelling in different baths. Competition between syneresis flow (gel membrane) and osmotic flow (liquid core).*

These last results seem to emphasize that in the case of suspension D (low M_w alginate and high concentration), the main contribution to weight loss measurements is the water

entry / exit due to the difference of ion concentrations inside and outside the capsule. In order to verify this assumption, we perform other experiments on beads containing 60 kg/mol sodium alginate.

d) Effect of alginate molecular weight

First, to simplify the problem, we consider alginate solutions (M_w = 60 kg/mol) without particles. According to Figure 3.11, the beads with lower alginate molecular weight do not loose as much water as the beads with long alginate chains. This result has also been established by Draget et al. [51]. They observed that the degree of syneresis (obtained 24 hours after gelation) is reduced by a factor 2 when alginate molecular weight is reduced from 320 kg/mol to 50 kg/mol.

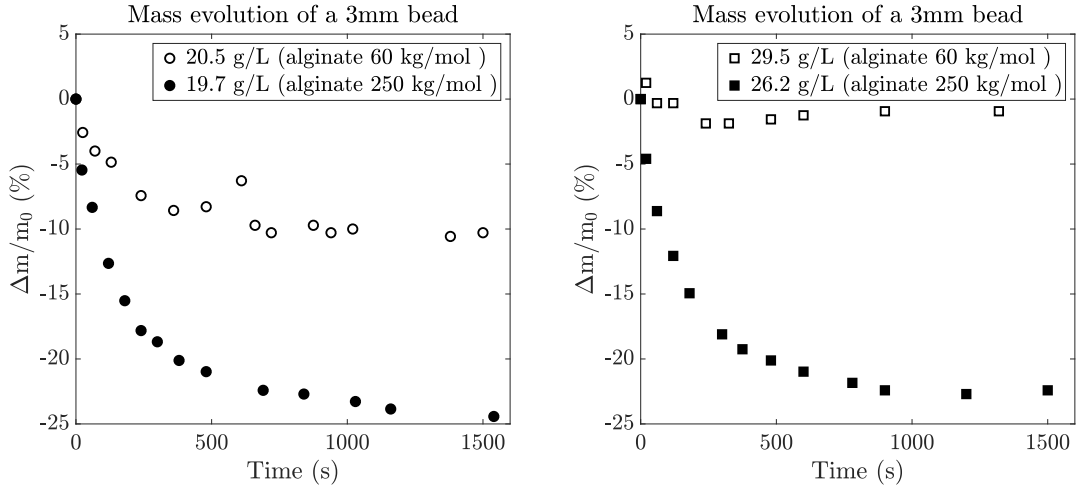

Figure 3.11 *Effect of alginate molecular weight on bead weight loss measurements. Open symbols: M_w = 60 kg/mol and filled symbols: M_w = 250 kg/mol. (a) [alginate] ≈ 20 g/L. (b) [alginate] ≈ 28 g/L.*

Figure 3.12 gathers the weight loss measurements obtained for beads containing 60 kg/mol alginate at different concentrations. We observe that the preceding result in paragraph a) linking volume loss and alginate concentration is still valid: the higher the alginate concentration, the lower the weight loss. However, it is notable that some of the beads tend to gain weight or stay unchanged rather than loosing weight, which is completely different than what we measured in Figure 3.5 for high M_w alginate solutions.

If the gelling beads contain zirconia particles, interesting results are obtained. In fact, similarly to paragraph b), we compare the swelling behavior of beads of same alginate concentration with or without zirconia particles. Figure 3.13 exhibits the resulting weight measurements. We notice that contrary to the previous observations in paragraph b), the presence of zirconia does not affect the overall bead swelling or deswelling behavior. This may be due to the fact that, as established in Chapter 2, the zirconia particles are not flocculated but well dispersed in the suspension, giving a Newtonian-like flow curve, thus less hindering the bead movement upon swelling or deswelling.

If we want to make a gelled bead (rather than a precipitate) using sodium alginate of molecular weight M_w = 60 kg/mol, we need to increase the alginate concentration (c > 20 g/L) otherwise the droplet disintegrates upon impact due to its very low viscosity. Consequently, referring to the previous observations, in our case for dripping suspensions containing low molecular weight alginate at high concentrations (suspension D for example), we expect the syneresis to be very low and therefore negligible. Indeed, this is what we observe experimentally in Figure 3.8 (b): the swelling behavior of a bead of suspension D is mostly controlled by the osmotic flow rising from the ion concentration difference between the inside and the outside of the capsule.

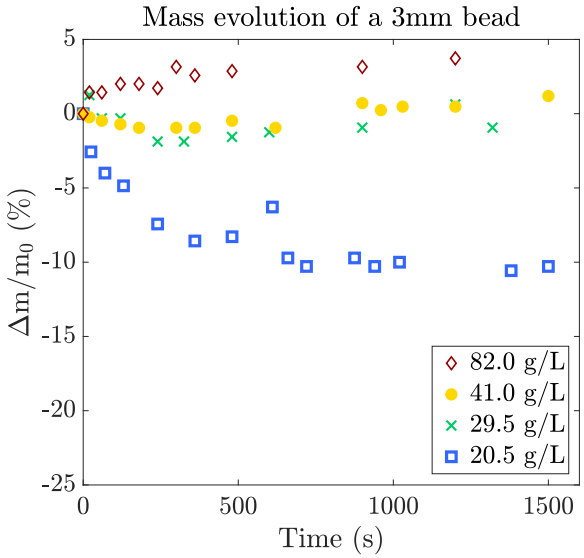

Figure 3.12 *Weight loss measurements on 3 mm gelling beads with varying alginate (60 kg/mol) concentrations (from 20 g/L to 82 g/L) without zirconia particles in a calcium bath of concentration 158 g/L. NB: solutions with low concentrations (c < 20 g/L) are very fluid, giving deformed beads with a very thin and fragile gel membrane so they may be more subjected to errors on weight measurements.*

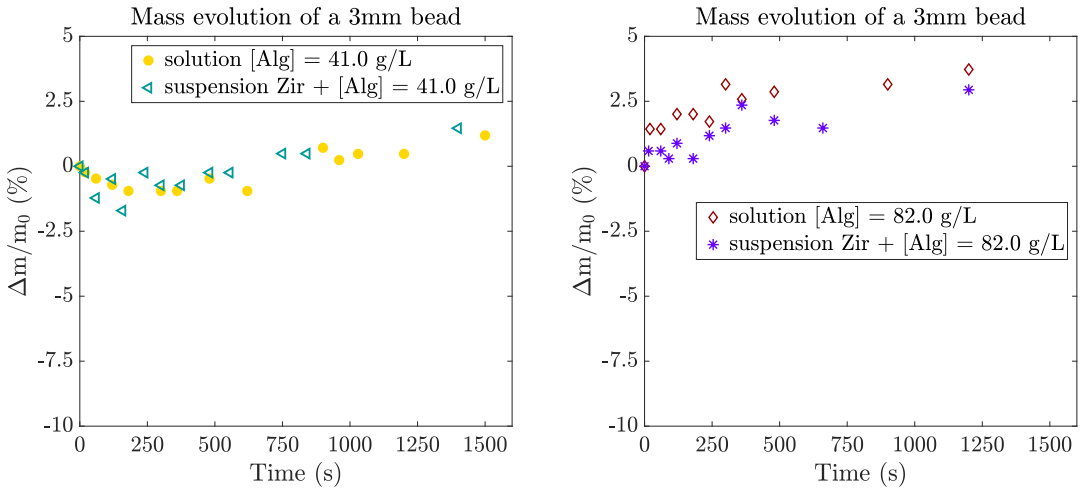

(a) (b)

Figure 3.13 *Weight loss measurements on 3 mm gelling beads in a calcium bath of concentration 158 g/L. Influence of particle content on syneresis. (a) [alginate] = 41 g/L. (b) [alginate] = 82 g/L. In all cases, M_w = 60 kg/mol.*

Different hypotheses can be formulated to justify this observation. First, the decrease in syneresis with reduced alginate molecular weight may rise from the concomitant increasing loose-end fraction, which reduces the possible attachment sites for the egg-box structures. Moreover, as previously established in Figure 2.17 of Chapter 2, the 60 kg/mol alginate solutions at 20.5 g/L and 29.5 g/L are in the semi-dilute unentangled regime, so the alginate chains may be subjected to more intra-molecular cross-linking rather than inter-molecular cross-linking, which can restrict the gel network from further contraction by preventing local rearrangements of egg-box structures, thus resulting in a lower degree of syneresis [51]. Another possible hypothesis refers to the protocol used to cut the alginate chains: by doing so, we may alter some of the monomers during hydrolysis, possibly leading to a decrease of G-blocks sequences, and therefore a decrease of syneresis.

e) Evolution of gel front with time

In addition to weight loss measurements, the advancing gel front can be observed as follows. After a certain gelation time, the capsule is extracted from the bath and cut in half with a razor blade. Then, we take a picture of the section, which enables us to distinguish the gelled crust from the liquid core and obtain an effective gel thickness h.

In Figure 3.14, we follow the gel thickness evolution with time for droplets of diameter D_0 = 1.4 - 1.6 mm immersed in three baths of different calcium concentrations. On the left (a), we give the results for the suspension A containing 0.8%wt of 250 kg/mol alginate. The gel thickness grows with time and shows a faster growth with increasing calcium concentration. On the right (b), we present the results for suspension D with 5%wt of 60 kg/mol alginate. In that case, h also increases with time and the higher the calcium concentration, the faster the gel growth. In a standard diffusion model, Ca^{2+} ions diffuse inside the droplet at the same speed regardless of the bath concentration. However, we can suggest that there is a calcium concentration threshold, above which the liquid suspension turns into a solid membrane. Therefore, in a bath of higher Ca^{2+} concentration, this threshold is reached sooner, meaning that the gel front advances faster, hence the evolution h(t) observed experimentally.

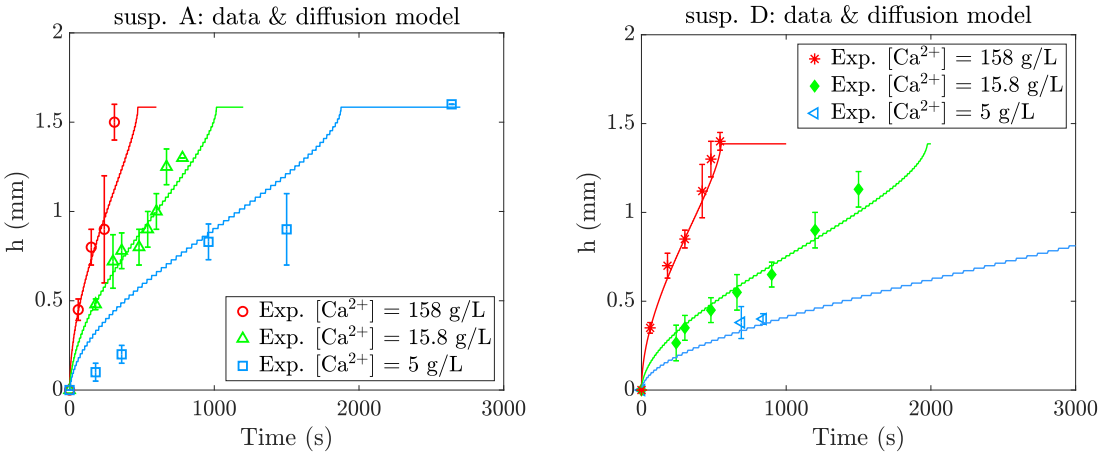

Figure 3.14 *Gel crust thickness measurements on beads of alginate - zirconia suspensions gelling in different calcium baths. (a) Suspension A: 0.8%wt alginate, M_w = 250 kg/mol. (b) Suspension D: 5%wt alginate, M_w = 60 kg/mol. The lines result from the diffusion model with a diffusion coefficient (a) D_{Ca} = 3.0 10^{-10} m^2/s or (b) D_{Ca} = 3.5 10^{-10} m^2/s.*

Experimentally, it is not possible to determine the gel thickness at very short time scales. Therefore, we want to model the evolution of h(t) in order to better predict it.

Since the gelation occurs for two alginate monomers and one Ca^{2+} ion, we can write the following simplified reaction:

$$2A^- + Ca^{2+} \rightarrow G$$

where A^- symbolizes a COO^- group and G an egg-box (a link between two alginate monomers and a calcium ion).

We further assume that the gel formation is a precipiation-like reaction: a given amount of Ca^{2+} ions is required to initiate the gelation. Above the gelation point, the concentrations of the free COO^- groups and Ca^{2+} ions are linked by the solubility product $K_s = [A^-]^2\,[Ca^{2+}]$. Besides, the kinetics is instantaneous and equilibrated. Similarly to [58], we assume that the speed of reaction follows a simple law such that $v_{gelation} = k\,[A^-]^2\,[Ca^{2+}]$ with k, the reaction coefficient, greater than D_{Ca} the Ca^{2+} diffusion coefficient: $k >> D_{Ca}$.

Therefore, in 3D spherical coordinates, the equations to solve are the following:

$$\begin{aligned}
\frac{\partial[Ca^{2+}]}{\partial t} &= \frac{D_{Ca}}{r^2}\frac{\partial}{\partial r}\left(r^2\,\frac{\partial[Ca^{2+}]}{\partial r}\right) - k\,[A^-]^2\,[Ca^{2+}] \\
\frac{\partial[A^-]}{\partial t} &= -\,2k\,[A^-]^2\,[Ca^{2+}] \\
\frac{\partial[G]}{\partial t} &= k\,[A^-]^2\,[Ca^{2+}]
\end{aligned}$$

In the Matlab code, we use k = 10^3 $L^2mol^{-2}s^{-1}$ and D_{Ca} as an adjustable parameter.

Finally, we need to take into account the initial conditions (at t = 0) to complete the description of our system. For example, for a drop of suspension A gelling in a bath of concentration 158 g/L, we have:

$$\begin{aligned}
&[Ca^{2+}](r < R_0) = 0 \\
&[Ca^{2+}](r \geq R_0) = 158\ \text{g/L} = 1.42\ \text{mol/L} \\
&[A^-](r < R_0) = 13.1\ \text{g/L} = 0.066\ \text{mol/L} \\
&[A^-](r \geq R_0) = 0 \\
&[G](r) = 0 \quad \forall r
\end{aligned}$$

The resulting curves are plotted in Figure 3.14 and we see that for a diffusion coefficient D_{Ca} = 3.0 10^{-10} - 3.5 10^{-10} m^2/s, they superimpose with our experimental measurements. Therefore, the simple diffusion of calcium ions in the droplet, turning the suspension into a gel, seems to describe accurately the experimental observations regarding the gel thickness growth. These curves will be further used in Chapter 5.

In this part, we have shown that the rapid gelation of alginate beads is accompanied by a change of weight due to two main osmotic flows: syneresis, linked to the reticulation reaction, and an inward or outward flow of water depending on the ion concentration inside and outside the capsule. The second one is easily predictable by calculating the ion concentrations in our system but the first one depends on the alginate molecular weight as well as alginate and zirconia concentrations. These parameters will also influence the final gel stiffness. That is why, in the next part, we focus on the mechanical properties of the gel beads and how they are affected when we change the composition of the suspension or the experimental conditions. These information will be very useful to understand the relaxation mechanism of the droplets (in Chapter 5).

3.3 Bead mechanical characterization

3.3.1 Apparatus

Once the zirconia-alginate beads have been produced, we use several techniques to characterize them. Among them, compression measurements are carried out on immersed gelled beads or gelled cylinders in order to investigate on the effect of suspension composition and varying gelling times on their mechanical properties. To do so, we design a small tank glued on a flat glass surface as well as a circular glass slide glued on an aluminum piece that we fix on the loading cell as shown in Figure 3.15.

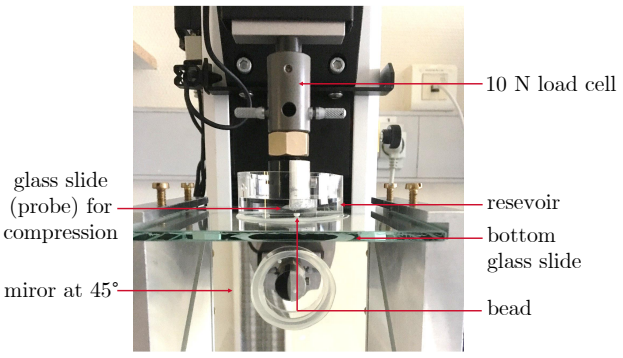

Figure 3.15 *Picture of the Instron set-up for compression tests.*

3.3.2 Experimental protocol

The main experiments performed on our gels are compression - relaxation tests. They were carried out on an Instron tensile tester (we kindly thank Alba Marcellan for her

training). First, we apply the cell's displacement corresponding to a bead deformation of 5% to 20%, at a compression speed of 0.01 mm/s. Then, we measure the stress relaxation in the bead by keeping the cell at the same displacement. For the sake of clarity, in all the following compression results, we plot positive values (i.e. -Force and -Deformation).

First, compression - relaxation tests are performed on 2 mm gelled beads under various conditions (different gelling time, calcium concentration, suspension composition, etc) as schematized in Figure 3.16 (a). The resulting curves, representing the force against the displacement, give us the relative stiffness of the beads but not their elastic modulus. Indeed, when compressed, the bead changes shape and its contact area with the glass slide varies. Using an approximation of the contact area to calculate the local stress applied on the bead from the force measurement is not really relevant as the real stress is not homogeneous at larger scale in the bead.

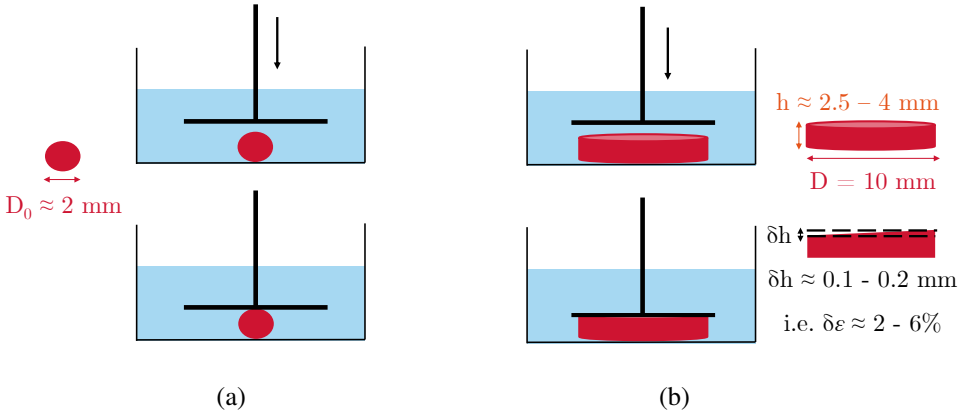

Figure 3.16 *Mechanical tests performed on (a) gel beads and (b) gel cylinders. Estimation of the deformation error $\delta\epsilon$ during the compression test due to the estimated flatness default in hand-cut cylinders.*

To overcome this issue, we perform compression tests on gel cylinders of diameter D ≈ 10 mm and height h ≈ 2.5 - 4 mm made using a round cutter of 10 mm diameter, and a razor blade. This last step is tricky as the planarity is essential to obtain valid stress - strain curves. The flatness error due to hand cut is estimated to be 2 - 6% as illustrated in Figure 3.16 (b). The considered suspensions are gelled for 2 weeks before performing the compression tests in order to estimate the elastic modulus at its higher value (when the gel is at equilibrium, i.e. at its highest gelation degree).

3.3.3 Experimental results

a) Bead behavior upon loading and unloading

Previous studies [42, 59–62], reported the mechanical properties of hydrogel beads. They were able to calculate the beads Young's moduli E from experimental compression data using Hertz analysis. Indeed, the contact mechanics of a linearly elastic spherical particle compressed between two flat rigid surfaces may be described by Hertz theory (1896). The relationship between the force F and the relative displacement of the plates Δ is, in that case, given by [61]:

$$F = \frac{\sqrt{2R_0}\,E}{3(1-\nu^2)}\,\Delta^{3/2} \tag{3.1}$$

where R_0 and ν are respectively the radius and the Poisson's ratio of the hydrogel bead. For instance, the following plot in Figure 3.17 was obtained by Chan et al. [42]. We can see that the Hertz model fits well their experimental data corresponding to the compression of alginate beads after 30 min gelation in a calcium bath of concentration 15 g/L.

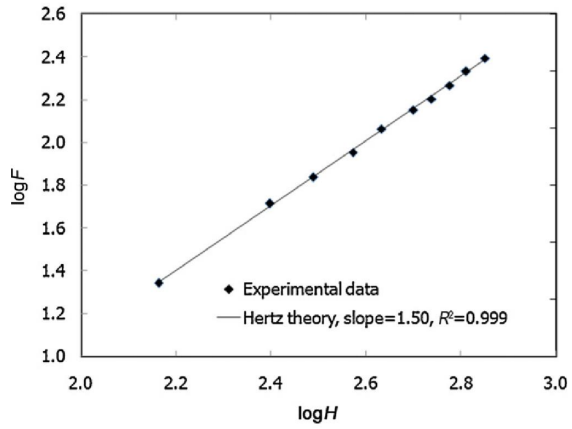

Figure 3.17 *Compression (up to 30% deformation) of a single alginate bead of diameter 2.7 mm after 30 min gelation in a calcium bath of concentration 15 g/L. Extracted from [42].*

In our case, the mechanical properties of the alginate-zirconia beads are completely different. Under compression, the force - displacement curve does not follow Hertz law as illustrated in Figure 3.18. The measured force seems to increase linearly with displacement. In fact, by plotting log(-Force) against log(Displacement), we notice that our experimental data are fitted by a line of slope 0.9 (close to 1, i.e. a linear evolution) rather than 1.5 given by Hertz theory. Therefore, Equation (3.1) cannot be used to

estimate the elastic modulus of the gelled beads from our compression results.

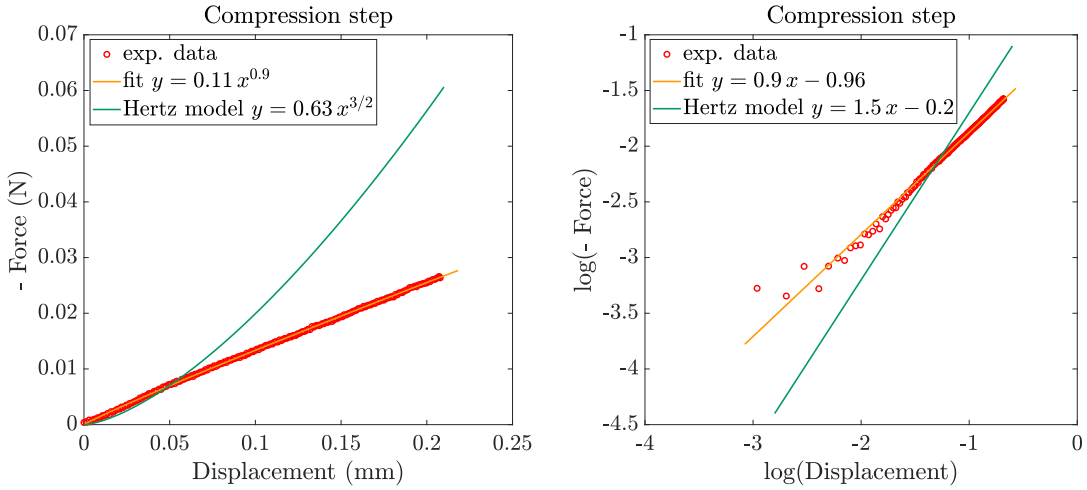

Figure 3.18 *Compression of a bead of reference suspension (0.8%wt of 250 kg/mol alginate) after 2 weeks gelation in a calcium bath of concentration 158 g/L. (a) - Force against Displacement ; (b) log(- Force) against log(Displacement). Comparison between experimental data and Hertz model.*

In order to have a general view of the overall mechanical behavior of a ceramic-alginate bead, we perform loading - unloading cycle compression tests. To do so, we first apply a deformation of 10% to the bead at a speed of 0.01 mm/s and when the maximal deformation is reached, we unload the sample at the same speed. The force response is measured. A typical example of the resulting response for a bead of suspension A after 15 min gelation is shown in Figure 3.19. At the beginning of the curve, the force is null (in the noise) as the probe moves down in the bath reservoir (1). Then, as soon as the probe touches the bead, the force increases and continues to increase until reaching the maximal displacement: it is the loading step (2). Finally, the probe is pulled back up and the measured force decreases: it is the unloading step (3 & 4). We observe that the loading and unloading curves are not superimposed, meaning that the gelled bead is not purely elastic but has a viscoelastic behavior.

In practice, it is difficult to determine precisely the mechanical properties of alginate gels using uni-axial compression because experiments are affected by uncertainty due to the bead geometry (when the probe compresses the bead, the contact area varies and may be subjected to sliding) and water exudation [60, 63]. In fact, alginate hydrogels contain more than 80%vol water: some of the water is bound to the polymer network

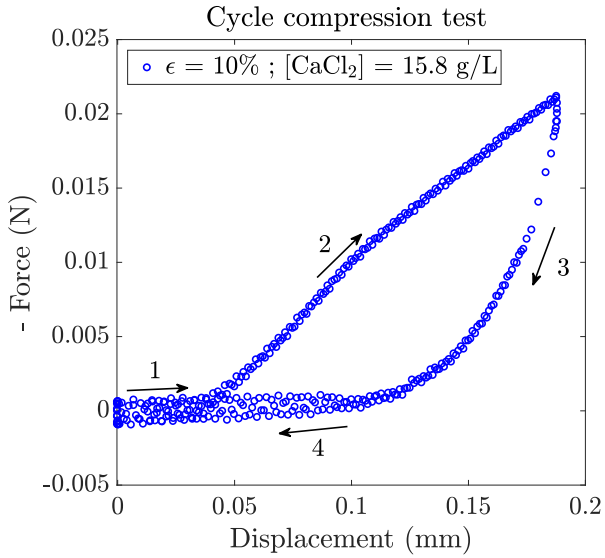

Figure 3.19 *Cycle compression test at ϵ = 10% deformation on a bead of suspension A (0.8%wt of 250 kg/mol alginate) after 2 weeks gelation in a calcium bath of concentration 15.8 g/L.*

due to osmotic forces, and some is free. During compression, the beads experience a rise of internal hydraulic pressure. If the compression speed is high enough, the water loss appears to be negligible [60] but at slow compression speeds, water can flow out of the structure.

That is why alginate beads mechanical properties are time-dependent, so we need to keep the same testing parameters in order to compare the beads mechanical behaviors. In the next paragraphs, the influence of several parameters are studied qualitatively and comparatively.

b) Influence of gelling time

Experimental data from the compression - relaxation tests on gelling beads of suspension C (1.6%wt of 250 kg/mol alginate) are shown in Figure 3.20 (a). First, the force is equal to zero when the glass slide has not touched the bead yet. Then, the compression step starts and the force increases linearly with time until reaching a maximum value F_{max} depending strongly on the gelling time: the higher the gelling time, the higher the maximal value. At this moment, the displacement is held constant and the force is measured. We observe a decrease of the force, meaning that the bead relaxes the stress. Two extreme cases are well-known: if the force relaxes to zero, the material behaves like

a liquid and if the force stays at its maximum value F_{max}, the material behaves like an elastic solid. In our case, the marked decrease in the observed force indicates that the composite beads are not purely elastic but rather of viscoelastic character [62]. This was confirmed by compression at different speeds, where higher speeds resulted in higher F_{max} (not shown).

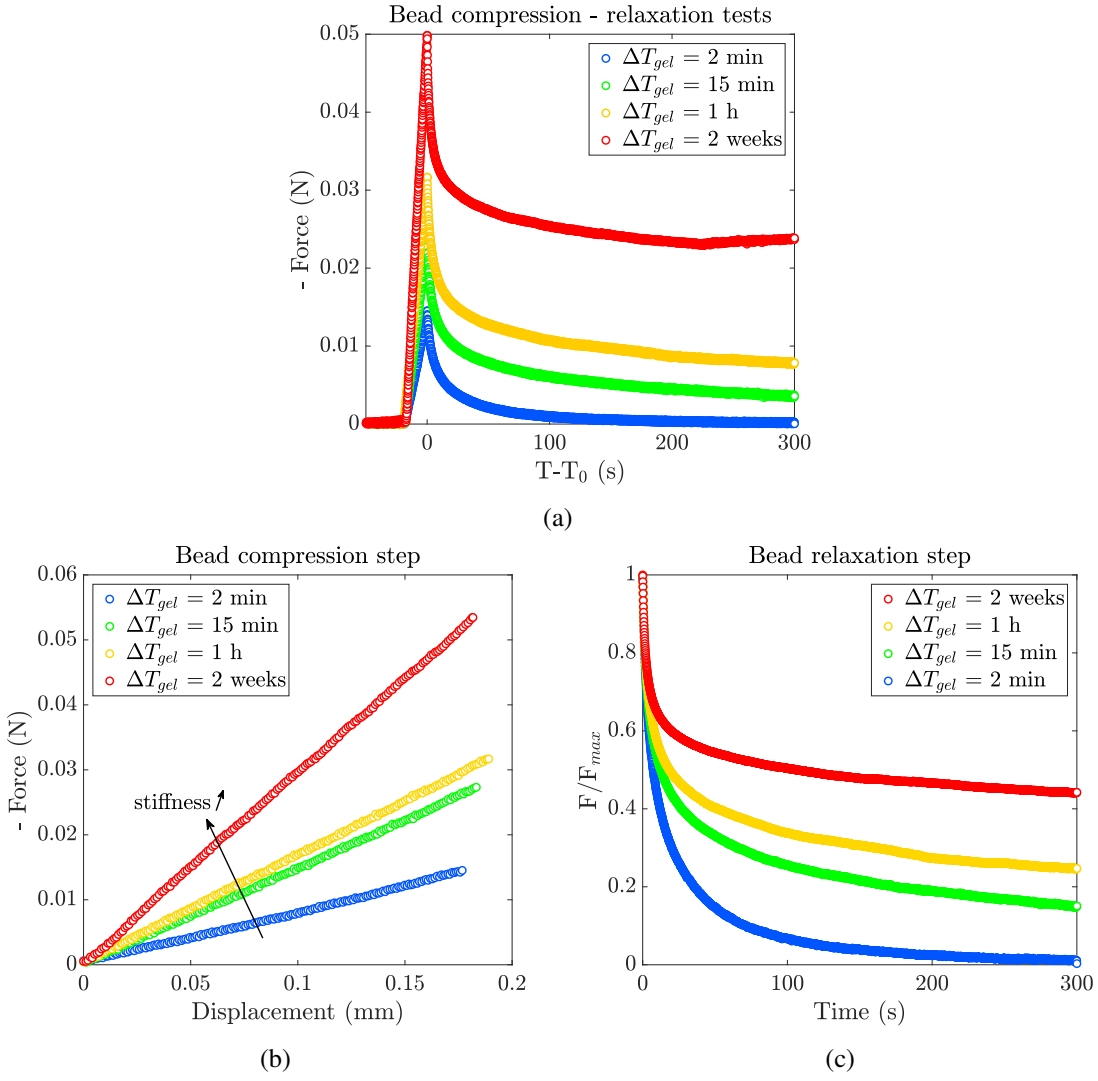

Figure 3.20 *Relaxation - compression test on a bead of suspension C ([alginate] = 1.6%wt and [zirconia] = 40%wt), after different gelling times in a bath of concentration [$CaCl_2$] = 158 g/L. T_0 is the time when the Force reaches its maximum value F_{max}. (a) Entire relaxation - compression test. (b) Compression step. (c) Relaxation step.*

In Figure 3.20 (b), the compression step is shown. We observe that the higher the gelling time, the higher the slope of the curve meaning a higher stiffness. As a matter of

fact, for longer gelling times, the bead is composed of more egg-box structures, which can be compared as reticulation points, and so it is stiffer.

Looking at the relaxation step in Figure 3.20 (c), the lower the gelling time, the greater the relaxation. In fact, when kept 2 min in the gelling bath, the capsule still has a liquid core referring to h(t) in Figure 3.14 (a). Consequently, the measured force is the result of both the solid crust and the liquid core contributions. In that case, we observe that the force relaxes to zero similarly to a liquid material. In the other cases ($\Delta T_{gel} \geq 15$ min), the bead is totally gelled so the force relaxes to a finite value F_∞. We observe that this value higher for longer gelation times, i.e. for strongly reticulated beads, which is consistent because reticulation points decrease the mobility of the polymer chains and hence their stress relaxation ability.

c) Influence of calcium concentration

When the bath concentration changes, the gelation kinetics is modified as we showed previously in Figure 3.14. But if we look at longer time scales, when the bead is totally gelled and has reached its final state, the calcium concentration does not seem to affect the bead mechanical properties.

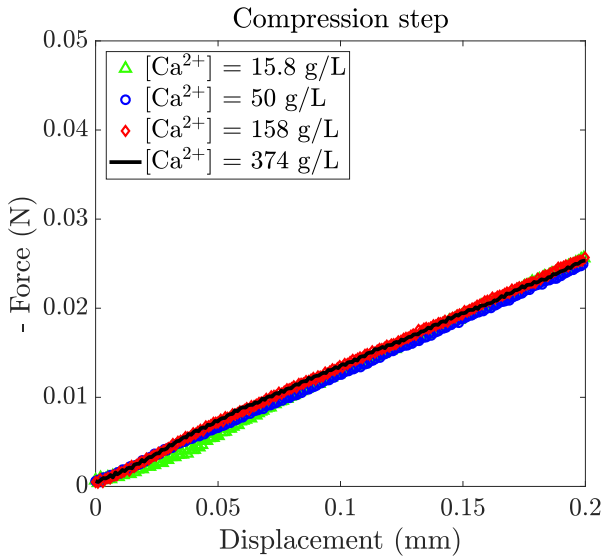

Figure 3.21 *Force against displacement during compression test on a bead of reference suspension (0.8%wt of 250 kg/mol alginate) after 2 weeks gelation in different baths.*

In fact, compression tests are performed on beads of suspension A (0.8%wt of 250 kg/mol alginate) gelled for two weeks in different baths of concentrations: $[Ca^{2+}]$ = 15.8 g/L,

50 g/L, 158 g/L and 374 g/L. The resulting data are shown in Figure 3.21. All the data superimpose, meaning that the bead has the same stiffness in its equilibrium state, independently of the initial calcium concentration in the bath. Indeed, the beads have the same alginate concentration, so the same number of G-blocks. When calcium ions diffuse inside the droplet, they react with the G-blocks units to form bridges between polymer chains. If we leave the bead in the gelling bath for a sufficient time, all the G-blocks will have reacted and rearranged and thus, no matter the initial Ca^{2+} concentration in the bath, the bead will have the same number of reticulation points, which is directly related to the bead stiffness [59].

d) Influence of zirconia content

Compression - relaxation tests are achieved on 1 hour gelled beads with varying amount of zirconia (0%wt, 40%wt and 60%wt).

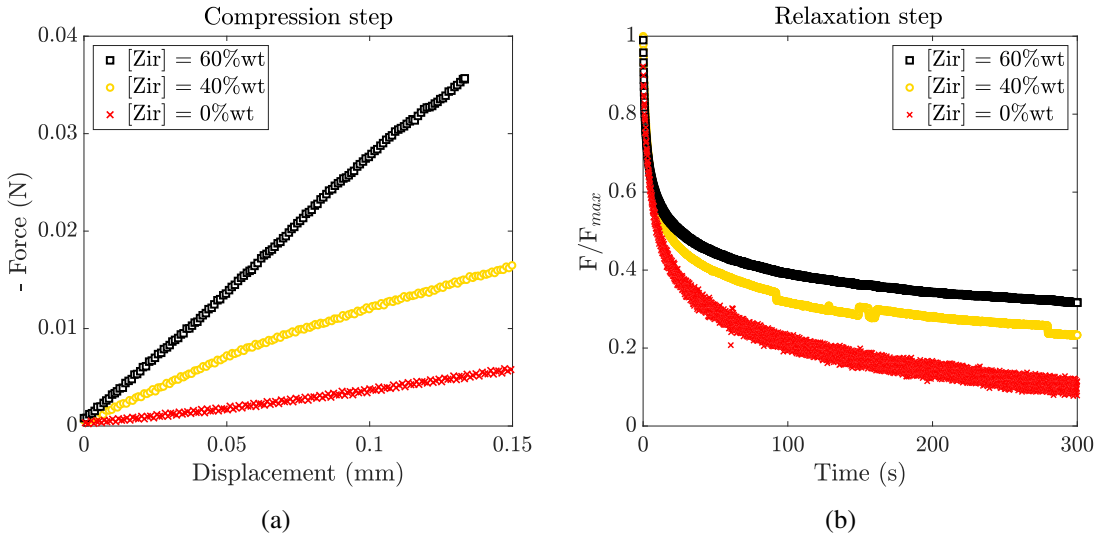

Figure 3.22 *Relaxation - compression test on beads containing 13.1 g/L alginate (250 kDa) and 40%wt or 60%wt zirconia, after 1 h gelation in a bath of concentration [$CaCl_2$] = 158 g/L. (a) Compression step. (b) Relaxation step.*

As expected, similarly to filler-reinforced polymers, the higher the particle content, the stiffer the material, which is illustrated in Figure 3.22 by the change of slope during the compression step. During the hold (relaxation step), the alginate bead without particles shows a better stress relaxation while the two other beads containing zirconia particles exhibit a comparable behavior. This may be due to the fact that the number of polymer chains and reticulation points are the same in both beads, so the mobility of

alginate chains is comparable in both cases. However, the force values at the end of the relaxation measurement lead us to believe that the presence of particles hinders chain relaxation.

e) Influence of alginate concentration

Ouwerxs et al. [59] showed that for alginate beads (without particles), the alginate concentration is the parameter controlling the bead's elasticity. They obtained the following equation: $E = K.C^2$, C being the polymer concentration and K a constant. In our case, where the beads contain ceramic particles, Figure 3.23 (a) illustrates that the bead stiffness is also highly dependent on alginate content. In fact, the higher the alginate concentration, the higher the number of G-blocks monomers, i.e. the higher the number of possible reticulation points, resulting in an increasing stiffness. As for the relaxation curves (b), they all look alike and have the same characteristic time. A possible explanation is that the stiffer bead contains smaller chains, hence more mobile chains. So even though its cross-link density is much higher, the chains can still relax partly the stresses due to their small size and their higher loose-end fraction.

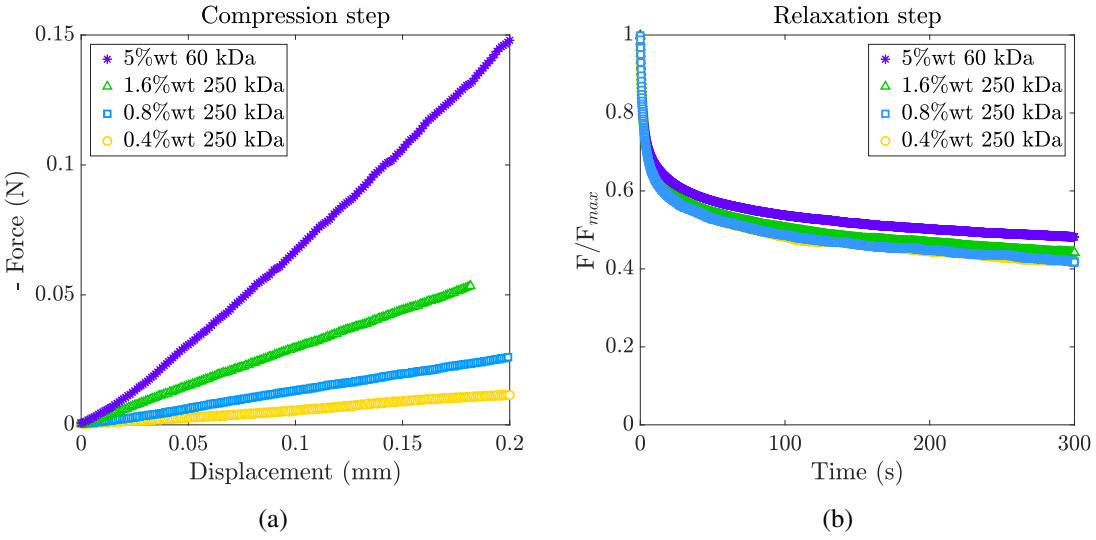

(a) (b)

Figure 3.23 *Relaxation - compression test on beads containing 40%wt zirconia and varying alginate content, after 2 weeks gelation in a bath of concentration [$CaCl_2$] = 158 g/L. (a) Compression step. (b) Relaxation step.*

f) Elastic modulus estimation

Typically, Ca-alginate beads deform plastically when they are compressed beyond 50% deformation [42]. Therefore, to obtain the elastic modulus of our gels, we compressed them at a maximum strain value of 10%. The experimental curves obtained from the cylinders compression are shown in Figure 3.24.

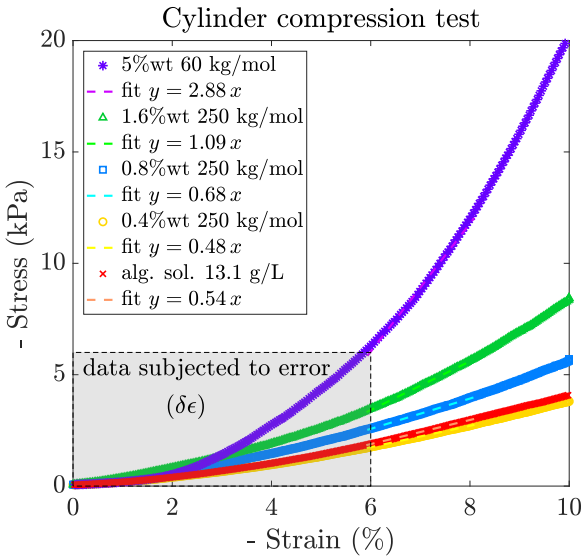

Figure 3.24 *Compression test on cylinder gels made out of the four main suspensions (A, B, C & D) and the alginate solution at 13.1 g/L without zirconia particles.*

The curves show a varying slope at small strains: this may be due to the flatness error, discussed earlier, estimated to be $2\% \leq \delta\epsilon \leq 6\%$. In fact, if the cylinder is not perfectly flat, the glass slide touches only a small part of the gel so the real contact area is much smaller than the estimated one. Therefore, we must look at the compression curves starting at a strain of 6%. We fit linearly the data on the strain range [6% - 8%] and the slope gives us an estimation of the elastic modulus of the gel cylinders. For 250 kg/mol alginate suspensions (A, B and C), the elastic modulus goes from 50 kPa to 100 kPa when the alginate concentration increases. For the suspension D (5%wt of 60 kg/mol alginate), its modulus is much higher: 290 kPa. Last, the alginate solution without particles shows a lower modulus ($\approx$ 50 kPa). The conclusion is clear: the higher the alginate or zirconia content, the higher the gel stiffness. However, we must keep in mind that these values are over-estimating the real moduli of the capsules gelled membrane, as they are taken after 2 weeks gelation, so the alginate chains have rearranged to form a very dense structure. In Figure 3.20 (b), we can see that the force evolution with displacement is 5 times steeper

for the oldest gel (2 weeks) compared to the youngest gel (2 min), meaning that in the gel ageing process, the modulus is increased by at least a factor 5. Bearing this in mind, the cylinders compression results allow us to determine a range of orders of magnitude for the gel modulus of the bead crust in formation during the drip-casting process, which will be used in Chapter 5: E $\approx$ 10 - 100 kPa.

3.4 Conclusion

This chapter was dedicated to the gelation properties of alginate. When this polyelectrolyte is in contact with Ca^{2+} ions, it starts to gel promptly. A gel membrane is thus immediately formed, growing as a square root of time at the beginning and then linearly with time. During the gelation, calcium ions diffuse inside the alginate droplet and get trapped by G-blocks monomers to form egg-box structures. Along with this rapid gelation, a phenomenon called **syneresis** takes place. It is characterized by the slow expulsion of water. The higher the calcium concentration in the bath, the faster the gel growth and thus, the faster the water loss. Syneresis is also dependent on the droplet composition: the lower the alginate concentration and the higher the molecular weight, the higher the syneresis. Similarly, the lower the zirconia concentration, the higher the syneresis.

Depending on the ion concentration inside and outside the droplet, another osmotic flow is evidenced. In the case of suspension D (low M_w and high concentration), the water loss is very low and we measure a swelling of the capsule. When the ion concentration inside the droplet is high, an inward flow of water is identified, greater than syneresis, causing the capsule to gain weight.

Once the bead is formed, we can compare their stiffness by conducting compression tests. We find that the beads are stiffer for longer gelation times because the G-Blocks rearrange to get together and confer better mechanical properties. The alginate-zirconia beads have an overall viscoelastic behavior. We managed to give an approximate estimation of their modulus at equilibrium (after 2 weeks gelation), by applying compression tests on cylinders. We found a modulus ranging from 10^4 Pa to 10^5 Pa.

Take-home messages of chapter 3

- When the alginate droplet falls into a calcium bath, its gelation starts instantaneously: the gelled membrane thickness evolves first as a square root of time. Then, at longer time scales, the gel grows linearly with time. The higher the calcium concentration in the bath, the faster the gelation.
- Syneresis (i.e. water expulsion) occurs during droplet gelation.
- The gelled bead containing zirconia and alginate has viscoelastic behavior.
- The order of magnitude for the gel elastic modulus is $E \sim 10^4 - 10^5$ Pa.

Part II

Physics of drip casting process

Introduction of Part II

The alginate suspensions and gels being characterized in the first part, we now focus on the two main issues of the dripping process: impact and relaxation of droplets. Before reporting the results concerning the impact and relaxation dynamics of droplets (Chapters 4 and 5 respectively), we first present in this introduction the dripping set-up used to study the droplets throughout all the steps of the process. Moreover, we estimate below the shear rates at play during the dripping process from the flow in the nozzle to the relaxation inside the calcium bath, which will be useful to discuss the influence of the suspensions rheological properties on the droplets impact and relaxation behaviors.

Experimental set-up

To start with, a drip-casting set-up at the lab scale is made. First, a Norcan frame, on which a mount is placed, is designed at the lab's workshop. An aluminum piece is also designed at the workshop and fixed on the movable support. This piece makes the connection between the suspension's arrival and its exit through the nozzle. During the process, the alginate-ceramic suspension is stored in a 100 mL steel syringe and is pushed out a Tygon tube joining the dripping nozzle thanks to the aluminum connecting piece described previously. The fluid flow rate is controlled by a syringe pump from KDScientific. Nozzles of different diameters (from 100 μm to 400 μm) are used. The collecting bath is a cubic 15 cm×15 cm×15 cm Plexiglas bath preventing distortion effects during the observation of capsules. Finally, to visualize the droplets behavior upon impact with the bath, we use a high speed camera Photron Fastcam Mini, with a 105 mm Macro lens and a focal doubler from Sigma. A LED back light (50 000 cd/m^2 SLLUB White from Phlox) is placed behind the liquid bath, facing the camera as shown in Figure 3.25.

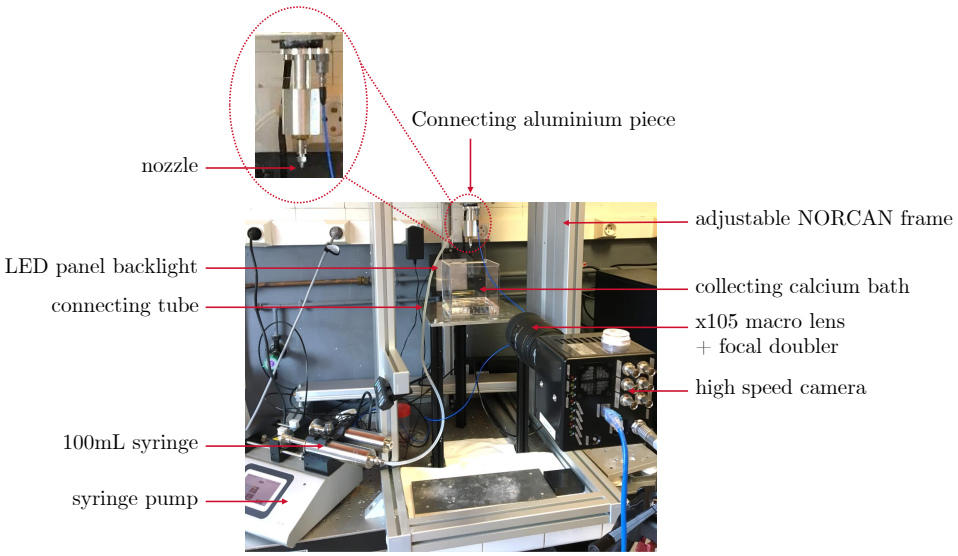

Figure 3.25 *Picture of the dripping experimental set-up*

Shear rate estimation at each step of the process

Nozzle Using the Mooney-Rabinowitsch equation, we can estimate the average shear rate $\dot{\gamma}_N$ in a nozzle of internal diameter D = 2R from the average flow velocity v [64], and the Poiseuille formula using the volumic flow rate Q:

$$\dot{\gamma}_N = \frac{8\,v}{D} = \frac{4\,Q}{\pi\,R^3}$$

This equation, valid for Newtonian fluids, can be transferred to non-Newtonian yield-stress fluids using the Herschel-Bulkley exponent m (calculated in Chapter 2):

$$\dot{\gamma} = \frac{3m+1}{4m}\,\frac{4\,Q}{\pi\,R^3}$$

During our experiments of dripping, the flow rate is varied from 0.01 mL/min to 0.1 mL/min and the typical nozzle used as a reference has an internal diameter of 375 μm which results in a range of shear rates: $\dot{\gamma} \approx 35 - 350\ s^{-1}$.

Fall When the droplet detaches from the nozzle, it falls down and relaxes to a spherical shape with a relaxation time depending on the suspension viscosity. At the considered flow rates, the drop formation at the nozzle tip takes 4 s to 50 s and in the usual experimental conditions, the fall lasts between 45 ms and 100 ms. As seen previously in

Chapter 2 dedicated to rheology, the suspension A (containing 250 kg/mol alginate at 0.8%wt) has a reversible behavior with a relatively short response (below 0.5 s) when we apply a shear rate increment from $\dot{\gamma} = 100\ s^{-1}$ to $\dot{\gamma} = 1\ s^{-1}$. Similarly, during droplet formation in the dripping process, the suspension undergoes a decrease of shear rate. As illustrated in Figure 3.26), a drop of suspension C (the more viscous) does not have time to relax its shape before impacting the bath: the droplet is not spherical but shaped as a pear. Therefore, in this case, the capillary relaxation time $\tau_{cap} \sim \eta L_0/\gamma$ (where γ is the surface tension of the droplet, η its viscosity and L_0 a typical length scale on which we observe the shape relaxation) is higher than the duration of the fall. So we can write:

$$\tau_{cap} > 45 - 100 \text{ ms} \quad \text{i.e.} \quad \eta > 3 - 7 \text{ Pa.s}$$

Referring to the flow curve, we notice that $\eta \sim 3 - 7$ Pa.s corresponds to $\dot{\gamma} \sim 2$ - 10 s^{-1}. These results emphasize the fact that during the formation and the fall, the droplet's viscosity increases to values expected for lower shear rates.

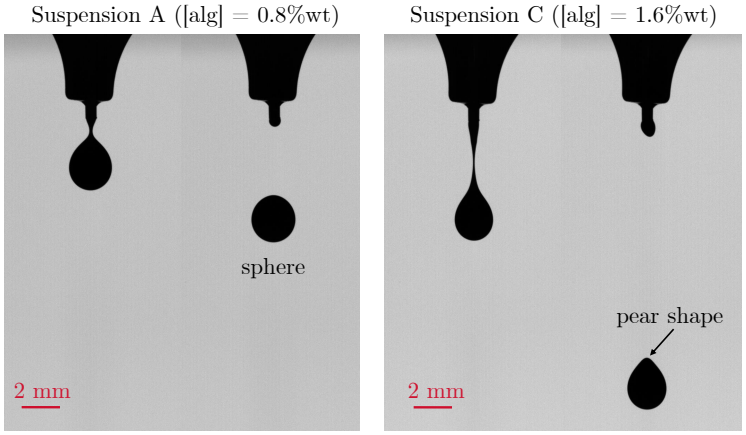

Figure 3.26 *Drop formation at the nozzle tip: the bottom part is formed first and thus has the time to relax to a spherical shape, whereas the top part is formed last, just before the fall so does not have as much time to relax.*

Impact When the droplet meets the calcium bath, it spreads and a gelled crust is formed. Inside the droplet, the speed is equal to zero on the gelled membrane and has a maximum value at the center of the droplet where the suspension flows to both sides of the droplet. Therefore, the suspension is sheared upon impact and we can give a first approximation of the effective shear rate using the impact speed U_0 and the size of the droplet: $\dot{\gamma}_{eff} \sim \frac{U_0}{D_0} \approx 200 - 1000\ s^{-1}$.

Relaxation After impact, the droplet detaches from the air/bath interface and sinks to the bottom of the bath while changing shape. Looking at the shape evolution of the droplet (studied in detail in Chapter 5), we can calculate an effective shear rate $\dot{\gamma}_{eff} \sim \frac{R(t+\delta t)-R(t)}{R(t)\times\delta t} \approx 0.5\ s^{-1}$.

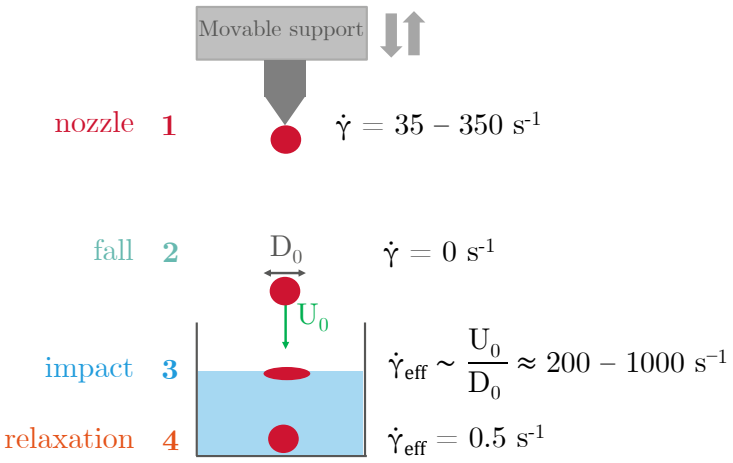

Figure 3.27 *Importance of rheology through all the steps of dripping process. The suspension is first sheared in the syringes, the tube and the nozzle, then the droplet relaxes during its fall and is sheared again upon impact to finally start relaxing at lower shear rates.*

Chapter 4

Impact

The major industrial issue resides in the non-sphericity of final beads, which starts with their deformation upon impact. That is why, in this chapter, we will analyze the dynamics of drop impact on the calcium bath in order to identify the parameters influencing the droplets elongation.

4.1 On the spreading of liquid drops: state of the art

4.1.1 Newtonian drops impacting a solid surface

Dimensionless numbers Impact and spreading of liquid drops are active areas of research. It has been shown that the droplet behavior upon impact on a surface depends on several parameters such as the velocity of the drop prior to impact, the surface tension and the viscosity of the fluid as well as the roughness of the impacted surface. Thus, impact dynamics are usually characterized by two main dimensionless numbers, the Reynolds and Weber numbers, defined from the liquid properties (surface tension γ and density ρ) as well as the droplet impact speed U_0 and diameter D_0 as follows:

$$Re = \frac{\rho D_0 U_0}{\eta} \quad \text{and} \quad We = \frac{\rho D_0 U_0^2}{\gamma}$$

These numbers balance inertia with viscous forces and capillary forces respectively. An important measurable dimension is the maximum diameter D_{max} reached by the droplet during impact onto the substrate. The dimensionless experimental variable usually studied is the maximum spreading ratio D_{max}/D_0. Moreover, a characteristic impact time $t_c = D_0/U_0$ is generally used in order to define a dimensionless time $t^* = t/t_c$.

Spreading dynamics The spreading mechanism of a droplet onto a solid substrate can be divided into three main phases [65]:

- The kinematic phase, at very short time scales ($t < 0.1\ t_c$), is the phase during which the droplet keeps a truncated spherical shape and no film spreads on the surface yet.

- The spreading phase: most of the spreading occurs during this phase, governed by inertia. The fluid surface tension and viscosity act together against the drop deformation. During the first two phases for which $t < t_c$, several authors have reported that the contact diameter evolves roughly as a square root of time: $D/D_0 \propto \sqrt{t^*}$. At the end of the spreading phase, inertia, viscosity and surface tension compete towards arresting the contact line and the drop diameter reaches its maximum D_{max}.

- The relaxation phase is driven by surface tension which tends to act against viscosity to minimize the free surface of the drop. Experimentally, we observe that

the contact diameter either decreases (i.e. the drop dewets the surface) or remains close to D_{max}.

Prediction models for the maximal deformation As mentioned earlier, an important variable of a drop impact on a solid substrate is the maximum spreading diameter. Numerous relations between D_{max}/D_0 and dimensionless numbers have been established in the literature [65–69]. Two regimes have been distinguished for the spreading factor.

The first regime is the **inertial regime** in which the maximal extension is obtained using a balance between the kinetic energy and the surface energy. In that case, viscous dissipation is neglected and we consider a low viscosity droplet impacting a super-hydrophobic surface. The energy conservation $\rho D_0^3 U_0^2 \sim \gamma D_{max}^2$ yields the scaling $D_{max}/D_0 \sim We^{1/2}$. In order to describe more accurately the experimental observations, Clanet et al. [67] developed an alternative using mass conservation and the thickness of the puddle created upon impact. They explained that this thickness h necessarily scales as a capillary length $a = \sqrt{\gamma/(\rho g)}$ with an effective acceleration experienced by the drop $g \sim U_0^2/D_0$. The volume conservation $D_0^3 \sim h D_{max}^2$ yields to the scaling law:

$$\frac{D_{max}}{D_0} \propto We^{1/4} \tag{4.1}$$

A drop hitting a surface first spreads inertially, whatever the nature of the surface. In fact, Clanet et al. [67] showed that the data of maximum spreading ratios for water droplets impacting various substrates (super-hydrophobic, plastic, linen paper, aluminum) all superimpose and follow the scaling law described by Equation (4.1). All these results only hold if the liquid has a low viscosity. In the case of higher viscosity, another regime has to be considered.

The second regime is a **viscous regime** in which the droplet spreading ratio is limited by viscosity. In that case, the kinetic energy is dissipated by viscosity during impact. The associated energy dissipation scales as $\eta (U_0/h) D_{max}^3$, η being the viscosity of the droplet and U_0/h the effective shear rate during impact. The energy balance yields to the scaling law:

$$\frac{D_{max}}{D_0} \propto Re^{1/5} \tag{4.2}$$

More generally, when impact dynamics are studied, the impact number $I = We/Re^{4/5}$ is defined and $(D_{max}/D_0)\,Re^{-1/5}$ is plotted against I. Thus, for $I < 1$ (inertial regime), the data describe a line of slope 1/4 and for $I > 1$ (viscous regime), the data are equal to 1.

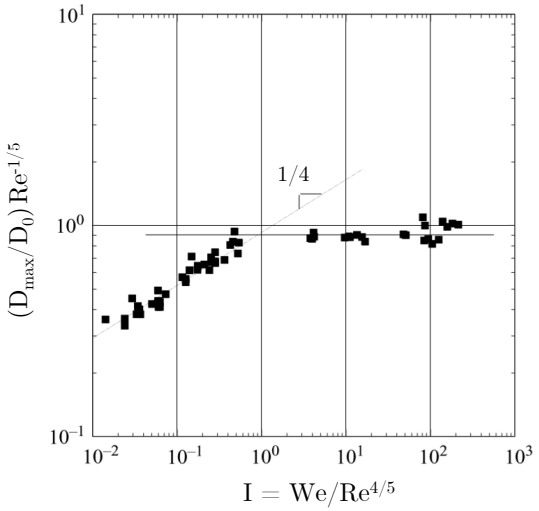

Figure 4.1 *Normalized dimensionless deformation of an impinging drop as a function of the impact number I, for all measurements. Two regimes are followed, the first one is the capillary regime and the second one is the viscous regime. Extracted from [67].*

4.1.2 Yield-stress fluids impacting a solid surface

So far, most of the studies have concerned Newtonian fluids. Understanding the impact behavior of complex fluids is very important for many industrial applications, including drip-casting process. More recently in the literature, non-Newtonian effects (normal stresses and elasticity for example) have been investigated by adding polymers or surfactants in the fluid [70, 71]. However, in some practical cases, the fluid used is more complex and displays a flow threshold. That is why, Luu et al. [72] investigated experimentally the impact of yield-stress fluids (polymer microgels or clay suspensions) on flat rigid surfaces (super-hydrophobic or partially wettable). They identified two regimes: a liquid-elastic and a viscoplastic regime. To describe the drop dynamics in each case, three additional dimensionless numbers are defined:

$$M = \frac{U_0}{\sqrt{G/\rho}}, \quad \gamma_c = \frac{\sigma_0}{G}, \quad De = \frac{U_0\,(K/G)^{1/m}}{D_0}. \tag{4.3}$$

The elastic Mach number gives the ratio of the impact velocity U_0 to the speed of elastic shear waves $\sqrt{G/\rho}$. The critical strain γ_c is the ratio of the yield-stress σ_0 to the elastic shear modulus G. Finally, De is the Deborah number comparing the fluid characteristic relaxation time $(K/G)^{1/m}$ (where K is the fluid consistency in Pa.s^m) and the characteristic

impact time $t_c = D_0/U_0$. In the limit of small Deborah numbers, the elastic deformations relax on time scales much shorter than the typical experiment time, meaning that the flow behavior is mainly viscoplastic. On the other hand, at large De, deformations have no time to relax during the impact and the flow behavior is mainly elastic.

When the deformation is **purely elastic**, the spreading of the droplet stops when its initial kinetic energy $\rho\,(\pi\,D_0^3/6)\,U_0^2$ is entirely converted into elastic energy $(\pi\,D_0^3/6)\,G\,\epsilon_{m,el}^2$ (where $\epsilon_{m,el} \sim D_{\max}/h$ is the elastic shear strain when the droplet reaches its maximum diameter D_{max}). Using the volume conservation $D_0^3 \sim h\,D_{\max}^2$, we obtain:

$$\frac{D_{\max}}{D_0} \propto M^{1/3} \tag{4.4}$$

In the **viscoplastic regime**, the scaling law described by Equation (4.2) for Newtonian fluids has to be revised. Indeed, the viscosity can be calculated using Herschel-Bulkley law expressed in Equation (2.5): $\eta = K\,\dot{\gamma}^{m-1}$. Equation (4.2) then becomes:

$$\frac{D_{\max}}{D_0} \propto \left(\frac{\rho\,U_0\,D_0}{K\,\frac{U_0}{h}^{m-1}}\right)^{1/5}$$

Using the volume conservation $D_0^3 \sim h\,D_{\max}^2$, we obtain:

$$\frac{D_{\max}}{D_0} \propto Re_m^{\frac{1}{2m+3}} \tag{4.5}$$

with $Re_m = \frac{\rho\,U_0^{2-m}\,D_0^m}{K}$ a generalized Reynolds number for yield-stress fluids. The transition between these two regimes described by Equations (4.4) and (4.5) is given by $M^{1/3} \sim Re_m^{1/(2m+3)}$ yielding to $M \sim (De/M)^{3m/(3-5m)}$. For different fluids, the boundary between the viscoplastic regime and the elastic regime differs due to the changing values of γ_c and m. A phase diagram can be obtained by plotting M/γ_c against De/M for all fluids and impact speeds, as illustrated in Figure 4.2. We will see how this phase diagram applies to our alginate - zirconia suspensions in Section 4.2.4.

4.1.3 Droplets impacting a liquid bath

In the drip-casting process, droplets of suspensions fall into a liquid bath. In the literature, the studies of liquid droplets impacting a liquid bath are usually focused on the analysis of the bath surface instabilities (waves and thin jet formation, gas-bubble entrapment, drop

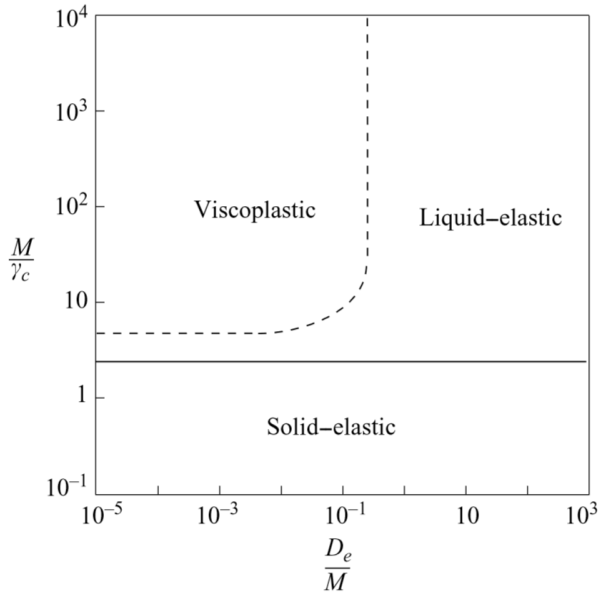

Figure 4.2 *Phase diagram showing the impact regimes of yield-stress fluids, extracted from [72].*

detachment, etc) [73, 74]. On the other hand, water-entry problem has extensively been studied for solid projectiles [75, 76]. Recently, Jalaal et al. [77] offered a new version of the water-entry problem by investigating the impact of yield-stress fluids in water. Indeed, at low stresses, these fluids behave initially like solids and above a critical stress (i.e. upon impact), they flow and behave like liquids. In that case, the solid-like properties of the projectile (i.e. the yield-stress and elasticity) as well as the shear-rate dependent rheological properties are expected to alter the dissipation mechanisms during the impact. The systems studied were Carbopol solutions with varying yield-stress values.

They showed that the droplets first reach a static shape (not always spherical) in the air before impact, then they deform plastically upon entry because they are subjected to high shear stresses, and finally they sink with a static shape at larger time scales (due to the decrease of the applied stresses below the yield-stress value). They demonstrated that the final bead shapes could be categorized using Reynolds number and Froude number ($\mathrm{Fr} = U_0^2/(g\,D_0^2)$). By shifting these numbers to high values, the capsules go from pears to sombreros to bowls and eventually spheres entrapping a bubble, as illustrated in Figure 4.3. The final spherical shape comes from the motion of the air cavity pulling on the droplet before complete detachment.

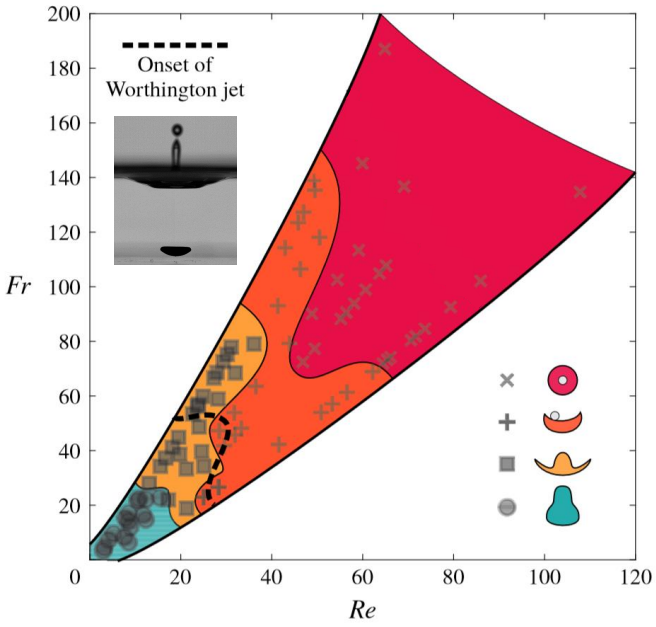

Figure 4.3 *Final shape of droplets categorized into 4 regimes: pears (in blue), sombreros (in yellow), bowls (in orange) and spheres (in pink), extracted from [77]. A picture of a Worthington jet, from our experiments, is added.*

4.1.4 Impacts of solidifying droplets

Drip-casting involves the gelation of liquid droplets. Droplet solidification upon impact is of great interest in many research fields and more particularly with the massive development of 3D-printing where a liquid of complex rheology is extruded through a nozzle and forced to spread on a solid substrate where it has to solidify instantly in a reproducible way to ensure good mechanical properties to the final product. Droplet solidification can be induced by heat transfer to the substrate. It is the case for raindrops that impinge and subsequently freeze on cold surfaces, which can have negative consequences on airplanes operations or wind turbines. Overall, the solidification of spreading drops is a challenging problem because it combines the spreading dynamics of a liquid drop simultaneously with heat transfer and phase transition. Watanabe et al. [78] observed the impact of n-cetane and n-eicosane on a cold surface and concluded that solidification had little influence on droplet maximal deformation because the solidification time was two orders of magnitude larger than the deformation time. As for molten wax droplets impacting an aluminum surface, Bhola et al. [79] found that the extent of droplet solidification was too small to affect the droplet impact dynamics. In both studies, it was shown that droplet deformation was proportional to $\mathrm{Re}^{1/5}$ (see Figure 4.4).

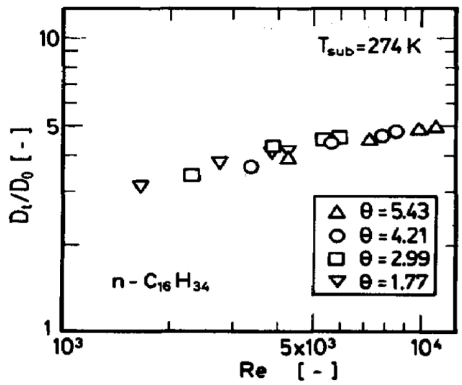

Figure 4.4 *Maximal deformation of a droplet of n-cetane against Reynolds number for different values of* $\theta = \frac{T_{\text{drop}} - T_{\text{sub}}}{T_{\text{mp}} - T_{\text{sub}}}$ *where* T_{sub} *is the substrate temperature,* T_{drop} *the droplet temperature and* T_{mp} *the melting point of n-cetane. Plot extracted from [78].*

On the contrary, in some cases, a droplet stops spreading because of temperature-dependent viscosity and/or because it starts solidifying before reaching maximal deformation. In these systems, drop arrest can be explained using crystallization kinetics [80] or solidification-induced pinning at the contact line [81, 82]. It has been established that the main parameter influencing the droplet spreading is the temperature difference between the substrate and the sol-gel transition temperature (or crystallization temperature).

4.2 Experimental results: impacts of alginate-zirconia suspensions

Looking back at the industrial application (drip-casting process), we are interested in the behavior of suspension droplets impacting a liquid bath. As shown in Chapter 3, the gelation reaction starts as soon as the droplet reaches the calcium bath and the resulting gel membrane thickness grows as a square root of time. So the main challenge of this work is to analyze the impact dynamics of initially liquid, complex fluid droplets which solidify upon impact with the calcium bath, to become entirely gelled beads in the end. To do so, we observe experimentally the impact dynamics and study the effect of multiple process or formulation parameters on the spreading of droplets.

4.2.1 Experimental observations

Using a frame rate of 4000 fps, we can visualize the spreading dynamics of the droplets. In Figure 4.5 (a), we show an image sequence of a droplet of suspension A (containing 0.8%wt alginate) falling into a liquid bath of concentration [Ca^{2+}] = 158 g/L.

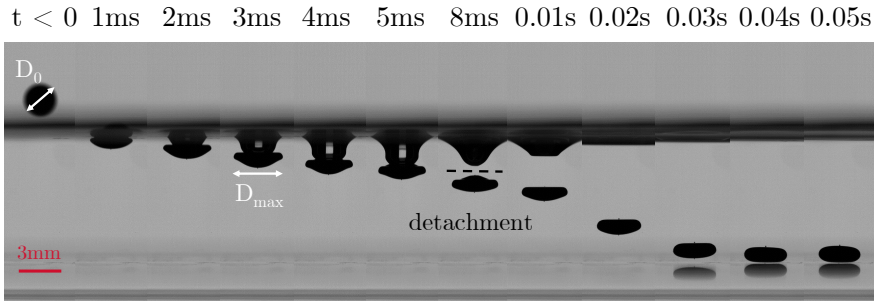

(a)

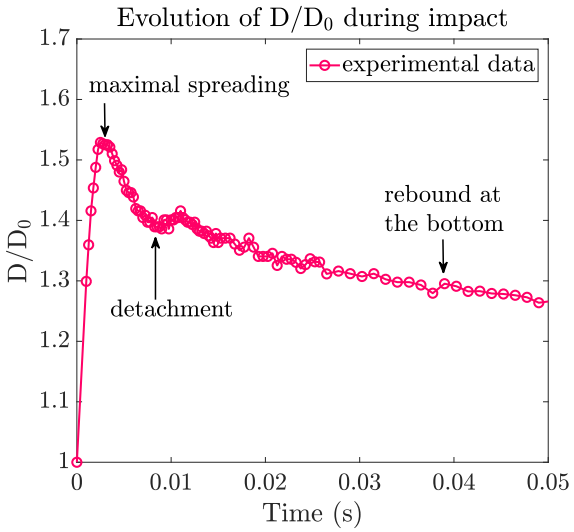

(b)

Figure 4.5 *Impact behavior of a droplet of suspension A (0.8%wt alginate) falling into a calcium bath of concentration 158 g/L at 1.4 m/s. (a) Image sequence. (b) Evolution of D/D_0 with time during impact.*

Below, in Figure 4.5 (b), we plot the corresponding deformation D/D_0 against time (from t = 0 to t = 0.05 s). During the spreading phase (from 0 to 3 ms), the droplet is rapidly elongated until reaching a maximum value D_{max}. Then, D decreases as the droplet keeps on penetrating the bath until reaching a local minimum value corresponding to the detachment from the interface. As a matter of fact, the air cavity pulls on the droplet as it closes and retracts, which leads to a (sometimes abrupt) decrease of the measured drop

elongation D. Afterwards, the relaxation phase starts: the droplet sinks and its horizontal diameter D continues to decrease. This shape recovery will be further discussed in Chapter 5. This curve gives us very useful information, including the maximal spreading ratio D_{max}/D_0 which is the most commonly used parameter to describe the spreading of a droplet (see Section 4.1). In the next sections, we will focus on this parameter to identify the main factors influencing the droplet deformation upon impact.

4.2.2 Influence of impact speed

To vary the impact speed U_0, we change the height of the nozzle with respect to the calcium bath. By doing so, we change the initial kinetic energy of the droplets. Figure 4.6 shows the evolution of the maximal spreading ratio D_{max}/D_0 for suspension A (containing 0.8%wt alginate of molecular weight M_w = 250 kg/mol), with varying impact velocities. We observe that the higher the impact speed, the higher the droplet deformation upon impact, which is consistent with the energy balance described earlier in Section 4.1. At very high impact speed (above 2 m/s), we notice that D_{max}/D_0 increases more slowly, suggesting a saturation value. In fact, as we discussed previously, the spreading of a droplet is not only controlled by impact speed but also by many other parameters such as droplet surface tension, viscosity and elastic properties.

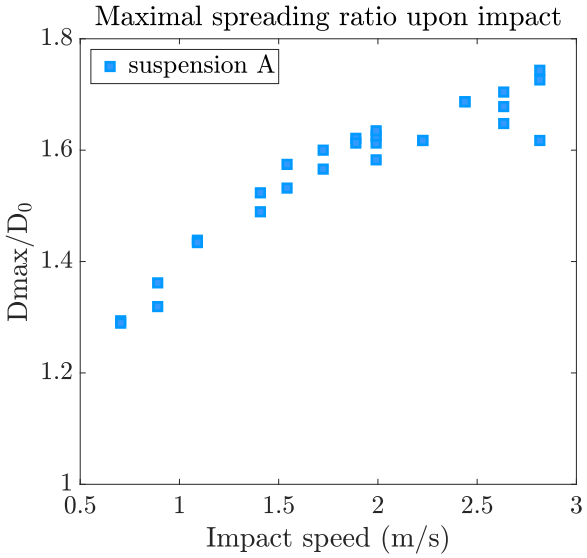

Figure 4.6 *Evolution of maximal spreading ratio (D_{max}/D_0) with varying impact velocities for suspension A (0.8%wt alginate, M_w = 250 kg/mol) in a bath of concentration [Ca^{2+}] = 158 g/L.*

4.2.3 Influence of calcium concentration

As mentioned earlier in the state of the art (Section 4.1.4), droplet solidification can have an effect on the spreading upon impact. In this part, we choose to focus on the influence of gelation on impact dynamics by changing the calcium concentration in the bath. In fact, in the alginate encapsulation community, to our knowledge, the influence of this parameter on droplet deformation has not been studied. Most articles examine empirically the effect of calcium concentration on the final shape and size of the capsules [40] rather than its effect on the impact dynamics. A global view of the spreading dynamics is shown in Figure 4.7. We follow the evolution of D/D_0 for a droplet of suspension A (0.8%wt alginate) falling with an impact speed of 1.4 m/s (a) or 2.0 m/s (b) in different gelling baths.

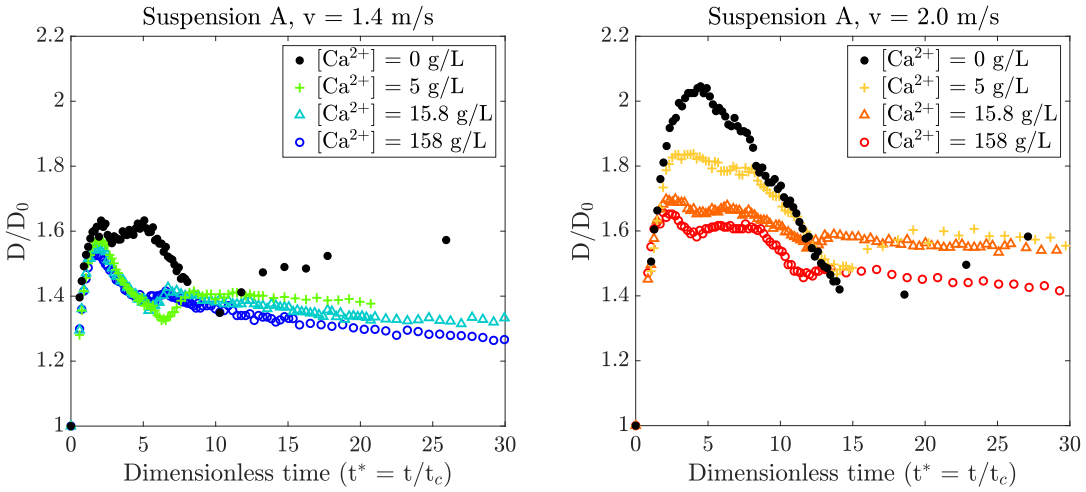

Figure 4.7 *Influence of calcium concentration on the spreading dynamics of a droplet of suspension A (0.8%wt alginate) falling in different calcium baths with different impact speeds: (a) v = 1.4 m/s ; (b) v = 2.0 m/s.*

- At very short time scales (for $t^* < 1$), all the curves superimpose and scale as $D/D_0 \propto \sqrt{t^*}$ (law predicted by [65]).

- At the end of the spreading phase, D reaches D_{max}. For an impact speed of 1.4 m/s (a), the bath concentration has no influence on the maximal spreading ratio, as all the curves superimpose. Indeed, the droplet spreads until reaching a maximum value at $t^* \approx 2$ for all calcium concentrations. However, at higher impact speed,

2.0 m/s (b), we notice a non negligible effect of the calcium concentration. In fact, at 2.0 m/s, we observe that the droplet deforms less at higher Ca^{2+} concentration. The same result is illustrated in Figure 4.8, where the evolution of D_{max}/D_0 with impact speed is plotted for droplets of suspension A falling into calcium baths of different concentrations. As explained in Section 4.1, in the case of viscous fluids, the spreading phase is usually controlled by the rheological properties of the drop. However, for high impact speeds, the maximal deformation seems to be affected by gelation. This may be due to the fact that for high deformations, the droplet surface in contact with the gelling bath increases, so the gelled membrane in formation has to be taken into account. In Chapter 3, we have shown that the gel thickness grows faster for higher Ca^{2+} concentrations. Although we do not know the exact mechanical behavior of the gel, we can speculate that the thicker the gelled membrane, the harder it is to stretch it. This assumption is consistent with the observed decrease of D_{max}/D_0 for increasing calcium concentration (i.e stiffer membrane). In the absence of Ca^{2+} ions, the droplet spreads more because all the kinetic energy is translated into elongation and the maximal elongation is reached at $t^* \approx 4$. As we increase the calcium concentration in the bath, the droplet stops spreading sooner. More precisely, we notice that the higher $[Ca^{2+}]$, the sooner the elongation arrest. This echoes the phenomenon of contact line arrest in the case of droplet solidification upon impact [80]: when the solidification time is smaller than the spreading time, there is an effect of solidification on droplet elongation.

- After reaching the maximal deformation D_{max}, the drop starts to relax its shape: D/D_0 decreases until the drop detaches from the air cavity. Interestingly, we observe that the drop detachment occurs at the same time ($t^* = 6$ for $v = 1.4$ m/s or $t^* = 12$ for $v = 2.0$ m/s) whatever the calcium concentration in the bath. At longer time scales, after detachment, we notice that the curves split up, meaning that the calcium concentration has a stronger influence on the relaxation phase than on the spreading phase. This will be discussed more deeply in Chapter 5.

4.2.4 Influence of rheology

The suspensions rheological properties can be varied by changing the alginate concentration as we mentioned in Chapter 2. We first focus on the suspensions A and B containing 0.8%wt and 0.4%wt alginate respectively. In Figure 4.9, we plot the evolution

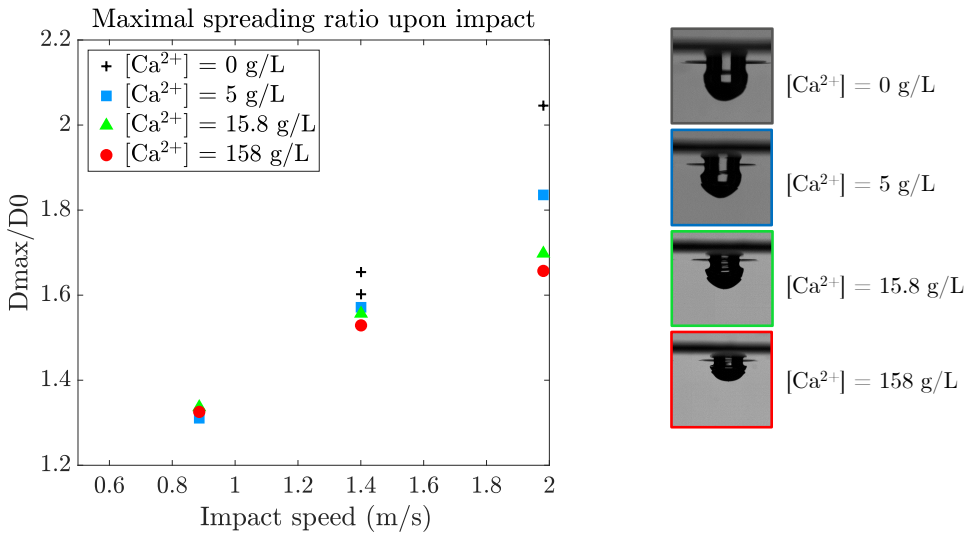

(a) (b)

Figure 4.8 *(a) Evolution of D_{max}/D_0 with varying impact speeds for suspension A (0.8%wt alginate), falling in calcium baths of different concentrations (from 0 to 158 g/L). (b) Corresponding pictures of the maximal deformation for droplets falling at 2.0 m/s.*

of droplets deformation D/D_0 upon impact, with an impact speed of 1.4 m/s (a) and 2.0 m/s (b). In both cases, the droplet of suspension B, which is less viscous, spreads more. Viscosity, and more generally rheology, seems to affect greatly the maximal deformation upon impact: the lower the viscosity, the higher the elongation upon impact. Since impact speed and rheology both influence droplet spreading, Reynolds and Mach numbers appear to be the parameters of choice to compare the data.

Similarly to Luu et al. [72], we calculate the Deborah and elastic Mach numbers defined in Equation (4.3) for our experiments in the case of our three yield-stress suspensions (A, B and C). The elastic shear modulus of each suspension is obtained by rheological strain sweep measurements at 1 rad/s (see Figure 4.10). By looking at the linear domain (where G' is constant before collapsing at large strain), we find an elastic modulus of 9.3 Pa, 14.5 Pa and 20 Pa for suspension B, A and C respectively. This allows us to plot the phase diagrams predicted by the model described in Section 4.1.2 for the three fluids. Looking back at Equations (4.4) and (4.5), the boundary between the elastic and the visco-plastic region is obtained by the following equation:

$$\frac{De}{M} \sim M^{(3-5m)/3m} \quad \text{i.e.} \quad \frac{M}{\gamma_c} \sim \frac{1}{\gamma_c}\left(\frac{De}{M}\right)^{3m/(3-5m)} \tag{4.6}$$

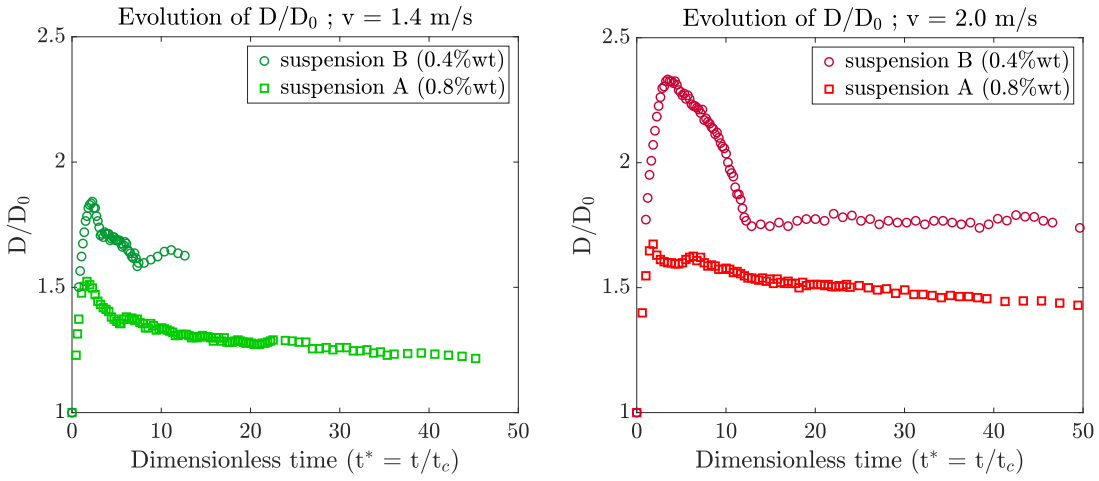

(a) (b)

Figure 4.9 *Influence of alginate concentration on the spreading dynamics. Comparison between suspension A (0.8%wt alginate) and B (0.4%wt algiante) for a droplet falling at v = 1.4 m/s (a) or v = 2.0 m/s in a calcium bath of concentration* $[Ca^{2+}]$ *= 158 g/L.*

The resulting phase diagram is illustrated in Figure 4.11. The experimental data show two kinds of behavior: droplets of suspension A ([alginate] = 0.8%wt) and C ([alginate] = 1.6%wt) are in the elastic zone whereas droplets of suspension B ([alginate] = 0.4%wt) fall into the visco-plastic zone.

However, in the case of suspension A, although the data points seem to be in the elastic region, the corresponding scaling law $D_{max}/D_0 \propto M^{1/3}$ is not verified (not shown). This may be due to the approximate description of the boundary given by Equation (4.6). Since the data points are quite close to the limit between these two regimes, we assume thereafter that the suspension A behaves like a visco-plastic fluid.

Figure 4.12 exhibits the maximal spreading ratio as a function of the elastic Mach number for suspension C (a), or the generalized Reynolds number for suspensions A and B (b) in agreement with the phase diagram established previously. We first plot the experimental data corresponding to impacts on a solid surface (PMMA) in order to compare the results with the theory predicted by [72]. Then, we superimpose the data obtained for impacts on a calcium bath of concentration 158 g/L. In the left plot (a), the data can be fitted by a power law $D_{max}/D_0 \propto M^{0.33}$, which is consistent with Equation (4.4). On the right plot (b), the data collapse on a single master curve of slope $0.22 \approx 1/(2m+3)$, as predicted by Equation (4.5). Interestingly, the spreading of droplets upon

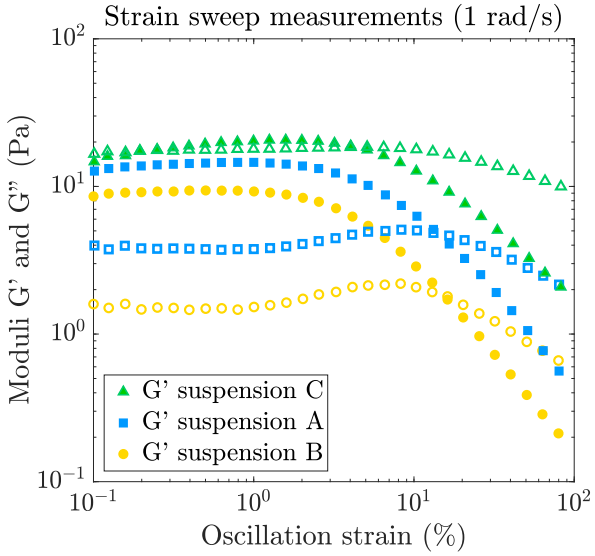

Figure 4.10 *Strain sweep oscillatory measurements at 1 rad/s: determination of storage (G', filled symbols) and loss (G", open symbols) moduli.*

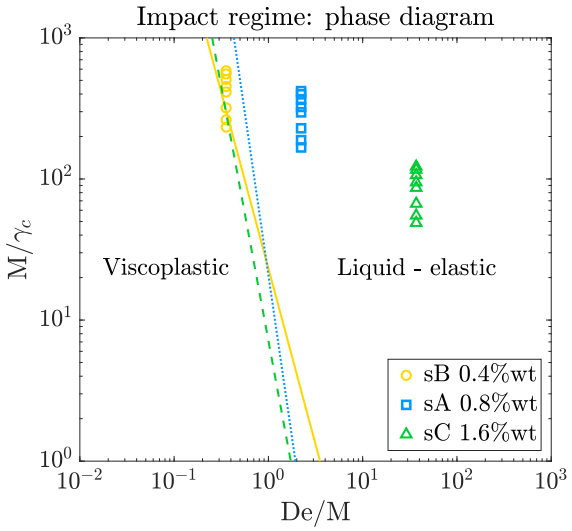

Figure 4.11 *Phase diagram describing the experiments of suspensions A, B and C impacting the gelling bath of concentration [Ca^{2+}] = 158 g/L (according to Luu et al. model [72]). The region boundaries are given by the lines (solid, dotted and dashed for suspension A, B and C respectively).*

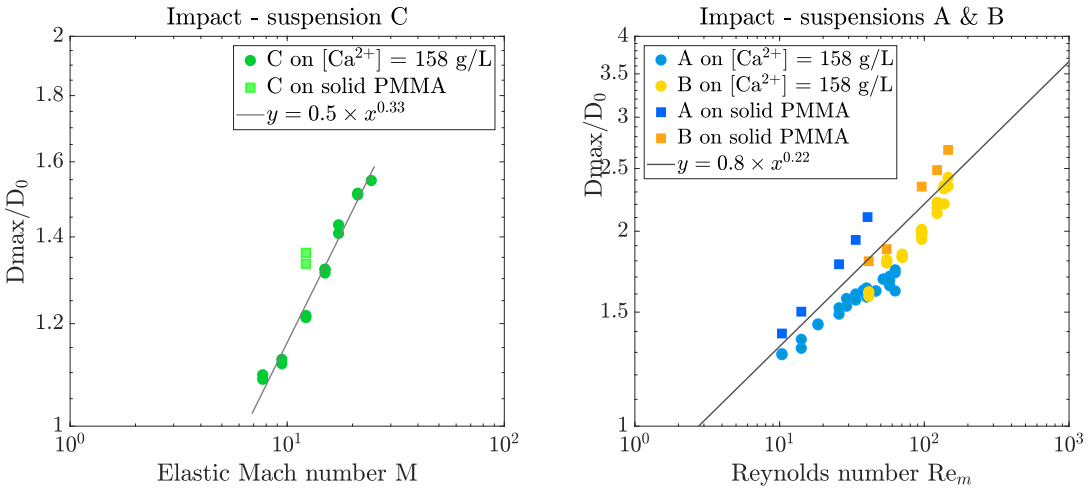

Figure 4.12 *Impacts on a solid surface (■) and on a liquid bath [Ca^{2+}] = 158 g/L (●). (a) Elastic region: D_{max}/D_0 against M for suspension C ([alg] = 1.6%wt). (b) Visco-plastic region: D_{max}/D_0 against Re_m for suspension A ([alg] = 0.8%wt) and B ([alg] = 0.4%wt).*

impact with a solid or a liquid surface are comparable. We find globally higher values of the spreading ratio for impacts on solid but this must be due to the definition of D_{max} for impacts on liquid baths: it is defined as the horizontal maximal length of the droplet and not its total curved length, expected to be larger. As a consequence, we can predict the maximal deformation of suspension droplets in the drip-casting process simply by analyzing the impacts on a solid surface, which is handy for industrial trials.

To evaluate the robustness of the scaling law in the visco-plastic region, we perform experiments on droplets of different sizes to access a wider range of Re_m numbers. To do so, nozzles of various diameters are tested (from 90 μm to 375 μm) and a micro-valve dispenser "Gyger" is used to decrease furthermore the droplet size. Combining these two techniques, we are able to form droplets of diameters going from D_0 = 2.3 mm to D_0 = 0.3 mm. Moreover, in Chapter 3, we have seen that the gelation depends on the calcium concentration in the bath, so we perform dripping experiments on baths of different concentrations (from 0 g/L to 158 g/L). Finally, we change the rheological behavior of the impacting fluid by conducting experiments with Newtonian fluids: suspension D (5%wt alginate, M_w = 60 kg/mol) and alginate solutions without zirconia particles (with an alginate concentration of 13.1 g/L). All the data points are shown in Figure 4.13. We observe that all the data corresponding to suspensions A and B, in plot (b), follow the line

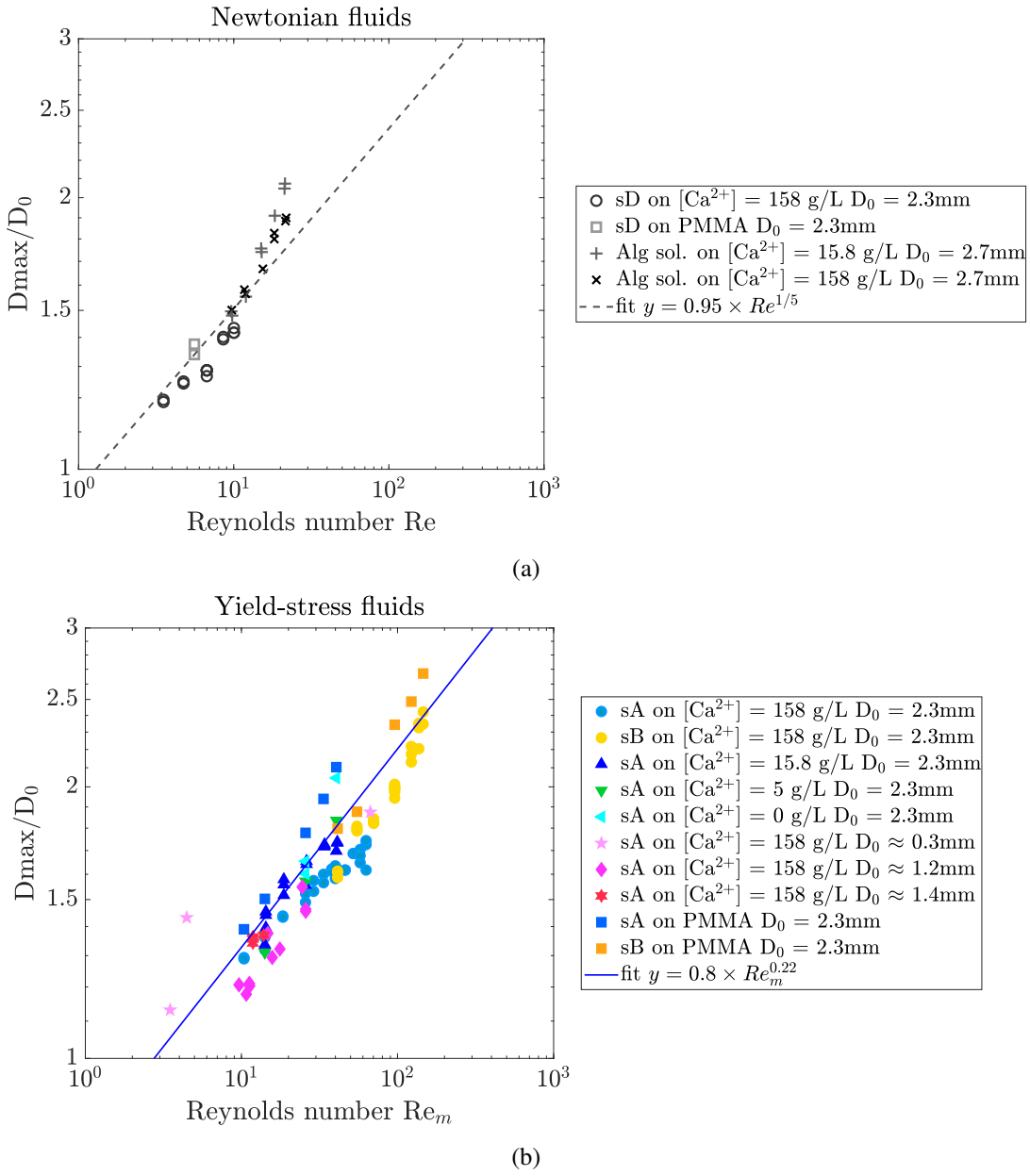

Figure 4.13 *Maximal spreading ratio (D_{max}/D_0) against Reynolds number (a) Re for Newtonian fluids ; (b) Re_m for yield-stress fluids.* ***Open black and grey symbols*** *are used for the Newtonian fluids (suspension D (5%wt of 60 kg/mol alginate) and alginate solution at 13.1 g/L without zirconia particles).* ***Filled colored symbols*** *are used for the yield-stress fluids (suspension A 0.8%wt of 250 kg/mol alginate and suspension B with 0.4%wt of 250 kg/mol alginate). (●) = reference data points (the bath concentration is $[Ca^{2+}]$ = 158 g/L and the droplet diameter is D_0 = 2.3 mm). (▲, ▼, ◀) = different calcium bath concentrations. (♦, ⋆) = different droplet diameters. (■) = impacts on a solid surface.*

of slope 1/(2m+3) ≈ 0.22, whereas the Newtonian fluids, in plot (a), are well described by the dashed line of slope 1/5. This brings us to the conclusion that the spreading behavior upon impact is mainly controlled by inertia, rheology, and calcium concentration to a lesser extent.

4.3 Simulation & comparison with experiments

4.3.1 Principle

In this work, we aim at understanding the rheological and gelation effects on droplet impact because it is a key step in the dripping process. In the previous section, we managed to predict the evolution of the maximal spreading ratio as a function of the rheological properties of the fluids. However, it is difficult to predict the whole spreading dynamics because of the complexity of the system. In fact, the considered suspensions are non-Newtonian as they exhibit a yield-stress. Moreover, upon impact with the calcium bath, the droplet starts to gel, involving significant complexity at the interface between the drop and the bath. Experimentally it is difficult to decouple the influence of viscosity and gelation process on the dynamics. Indeed, a change in the formulation will lead to a variation of both the rheological properties and the gelation mechanism, as seen in Chapters 2 and 3. Therefore, numerical simulations appear to be the best way to visualize the effects of various parameters on impact behavior.

Simulations were performed by Anselmo Soeiro Pereira, from the Mines ParisTech CEMEF laboratory. The computational approach used to simulate droplet impacts is based on a general solver (Climlib-CFD, a finite element library, [83]) which takes into account the complex rheological behavior of each fluid. In the model, the effective viscosity is computed using the Herschel-Bulkley constitutive equation with the parameters found in Table 2.2 in order to describe as accurately as possible the three main yield-stress suspensions.

In order to capture the droplet/air and droplet/bath interfaces as a function of time, a level-set method enabling the localization of interfaces is used. A detailed description of the method is given in [84, 85]. Then, the simplest way to take into account complex surface effects (i.e. droplet gelation) occurring at the droplet/bath interface, is to consider a surface tension between the droplet and the calcium bath. In the level-set method, the surface tension force is modeled as a distributed body force concentrated in a small band

around the interface. This band is chosen small enough (thanks to the very thin adaptive mesh network) such that the force has its maximum value on the interface and decays rapidly with distance from it, similarly to a smoothed Dirac function. This approach allows the surface tension to be modeled using standard numerical techniques in Eulerian models.

However, we must keep in mind that in our case, two interfaces meet (drop/air and air/bath) as the droplet hits the bath, so three media are at stake (droplet, air and bath) and the level-set method is challenged. In fact, it does not take into account the final stage of the drainage of the thin air layer between the drop and the bath (where long range interactions between the drop and the bath could play a role in the dynamics), or the complex dynamics of the triple line air/drop/bath.

To summarize, the modeling of our system is challenging, nevertheless, we consider yield-stress fluids droplets falling into an immiscible liquid bath with a tunable surface tension $\gamma_{d/b}$ between the drop and the bath. To simplify the problem, we use the same surface tension value for all the interfaces of the system. Figure 4.14 illustrates the anisotropic adaptive mesh network used to describe the whole system.

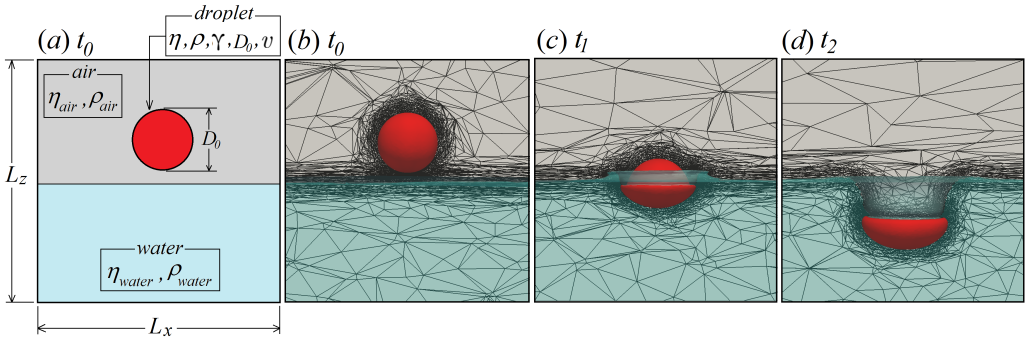

Figure 4.14 *Representation of the adaptive mesh network of the computational domain, at different steps of the process (before impact and during impact).*

4.3.2 Numerical results

First, the influence of impact speed is investigated. Figure 4.15 exhibits the numerical results obtained from the simulations by considering the rheological properties of suspension A (0.8%wt, M_w = 250 kg/mol alginate) and setting the droplet surface tension at $\gamma_{d/b}$ = 20 mN/m while varying the impact speed from 0.9 m/s to 2.0 m/s. The curves show a clear dependence on impact speed. The higher it is, the higher the maximal spreading

ratio upon impact: D_{max}/D_0 goes from 1.2 to 1.7 as we increase the drop kinetic energy. These results are consistent with Vadillo et al. [65] analysis saying that the spreading phase is mostly governed by inertia.

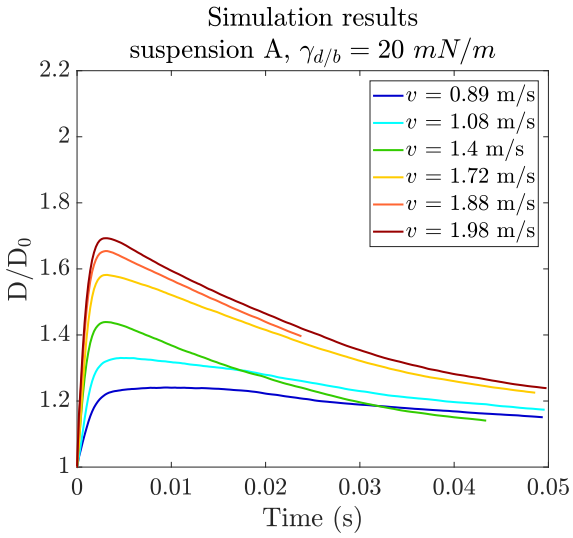

Figure 4.15 *Evolution of D/D_0 for a droplet of suspension A falling in a liquid bath with a surface tension $\gamma_{d/b}$ = 20 mN/m, at different impact speeds v going from 0.89 m/s to 2.0 m/s.*

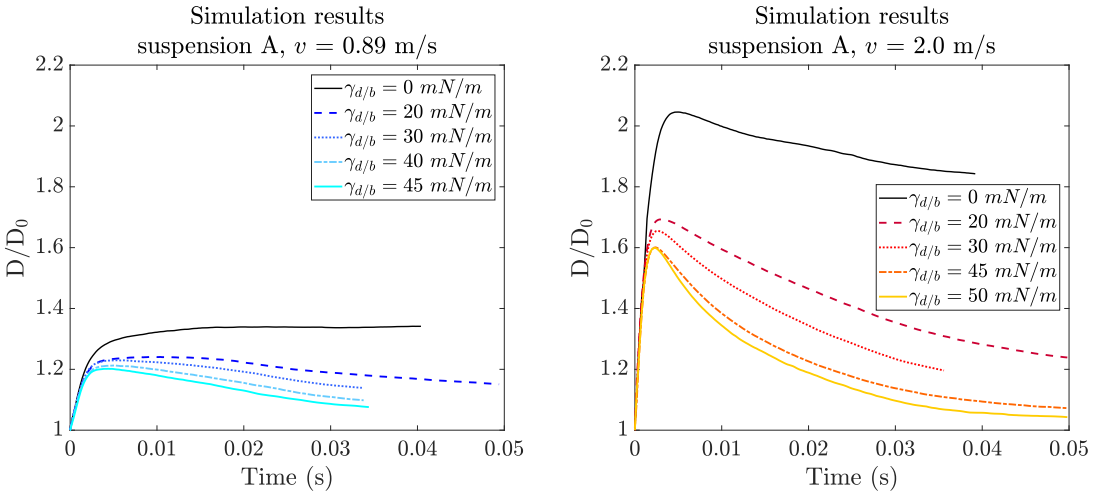

Figure 4.16 *Influence of surface tension $\gamma_{d/b}$ on droplet impact dynamics. Simulation results of a droplet of suspension A (0.8%wt alginate) falling in a liquid bath with an impact speed: (a) v = 0.89 m/s or (b) v = 2.0 m/s.*

On the other hand, we study the influence of the drop surface tension $\gamma_{d/b}$ (see Figure 4.16). We observe that no matter the impact speed, the surface tension value has no influence on the impact dynamics at very short time scales. In fact, during the spreading phase (i.e. before the droplet reaches its maximal deformation), all the curves superimpose, which is consistent with the experimental results showing that the major parameter influencing the spreading is inertia. Then, D/D_0 continues to increase until reaching a maximum. We notice that the higher the surface tension between the drop and the bath $\gamma_{d/b}$, the sooner the spreading arrest, resulting in a smaller maximal elongation D_{max}. As a matter of fact, at the end of the spreading phase, surface tension and viscosity enter in competition toward arresting the droplet elongation. This observation is all the truer at higher impact speed, where the difference in maximal deformation is more pronounced, which echoes the experimental data shown in Figure 4.7. Finally, the relaxation phase takes place. When the surface tension is equal to zero, no relaxation is observed: the droplet stays deformed after impact and D stays constant equal to D_{max} or decreases slightly at high impact speed. On the contrary, with a non-zero surface tension, the ratio D/D_0 decreases so that the droplet evolves towards a more spherical shape. The higher the surface tension, the faster the relaxation. Indeed, surface tension drives the relaxation by acting against viscosity to minimize the free surface of the drop until it becomes spherical as mentioned previously in the state of the art.

4.3.3 Comparison with experimental data

As shown in Section 4.2.3, the calcium concentration in the bath influences the maximal deformation upon impact, especially at high impact speed. Moreover, when a droplet of suspension falls into a bath of pure water (without Ca^{2+} ions), it does not relax but stays deformed and dissolves into the bath. These experimental observations seem to echo the previous numerical results where surface tension limits droplet spreading and enhances droplet relaxation. Thus a parallel between calcium concentration and surface tension is suggested.

By comparing the experimental and numerical curves showing the evolution of D/D_0 with time, we evidenced the surface tension value $\gamma_{d/b}$ for which the model fitted best the experimental data. That is why in both plots of Figure 4.17, we superimpose experimental data for $[Ca^{2+}]$ = 0 g/L and $[Ca^{2+}]$ = 158 g/L with simulation results for $\gamma_{d/b}$ = 0 mN/m and $\gamma_{d/b}$ = 20 mN/m. First, we notice there is a very good agreement between the experiments and the model for both impact speeds v = 0.89 m/s (a) and v = 2.0 m/s (b)

when there is no calcium in the bath or no surface tension implemented. In fact, in both experimental and numerical results, we observe an increase of D/D_0 upon impact until reaching a maximum value D_{max}/D_0, followed by no relaxation after detachment from the air cavity. The main notable difference between the experiments and the model is the effect of the air cavity retraction. Indeed, experimentally, we measure a decrease of D/D_0 just after the maximum elongation because the bath/air interface retracts to go back to a planar configuration. By doing so, it pulls on the droplet, leading to a decrease of D/D_0 until complete detachment. Then, D/D_0 increases as the droplet sinks freely until reaching the bottom of the bath where it spreads slowly and starts to dissolve. In the simulations, however, we notice a small decrease of D/D_0 due to the slow retraction of the air cavity pulling slowly on the droplet. Looking at the simulation movies, we can confirm that the cavity retraction is much slower than in the actual experimental case (30 ms against 15-20 ms). This difference is probably due to the simplified definition of the surface tension in the model, compared to the complexity of the interfaces in the real system.

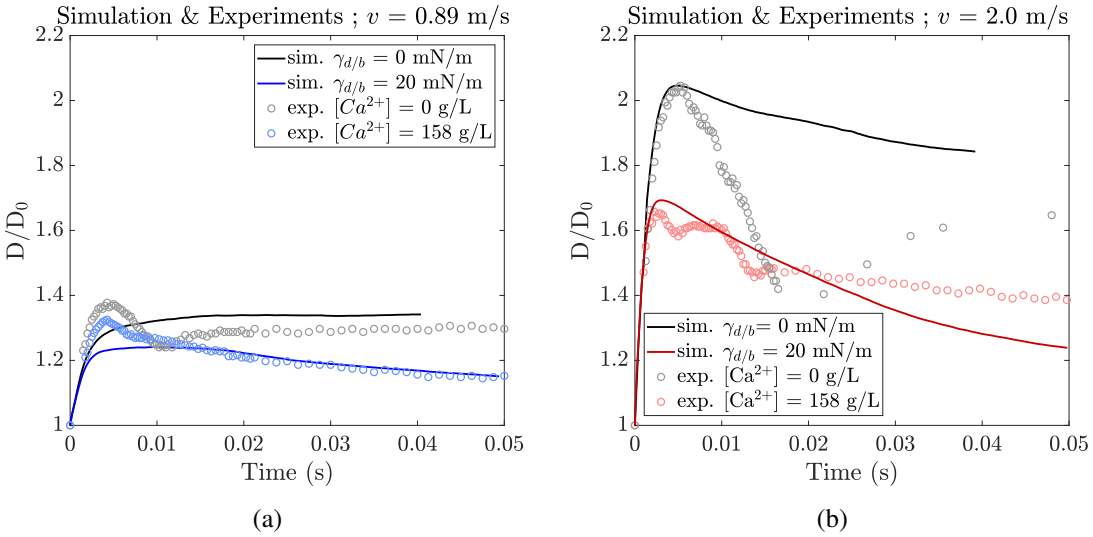

Figure 4.17 *Influence of surface tension and calcium concentration on droplet impact dynamics. Comparison between simulations and experiments for a droplet of suspension A (0.8%wt alginate) of impact speed: (a) v = 0.89 m/s or (b) v = 2.0 m/s.*

On the other hand, when we add calcium in the liquid bath and a non-zero surface tension in the model, the drop dynamics is changed but we can see that the overall shape of the curves are well captured by the model. Indeed, in both the experiments and the simulations we observe an increase of D/D_0 during the spreading phase until

reaching a maximal elongation, followed by a decrease of D/D_0 as the droplet relaxes its shape. This agreement between the experimental and the numerical curves reinforces our idea to introduce a surface tension between the drop and the bath in order to take into account the gelation phenomenon at short time scales. On the left plot (a), we notice that the experimental maximal spreading ratio is higher than the numerical one, suggesting that the surface tension effect is overestimated during the spreading phase at low impact speed. At higher time scales, the model seems to describe accurately the relaxation phase observed experimentally. On the right plot (b), the experimental data and the numerical results are in agreement for $t < 0.02$ s but at longer time scales, D/D_0 decreases more slowly in the experiments.

Al these results lead to the conclusion that the model with a drop/bath surface tension describes quite well the impact dynamics but suggest that our system is more complex and cannot be entirely predicted by simple surface tension effects.

To evaluate the robustness of the model, we change the suspension rheology. Figure 4.18 exhibits the comparison between the simulation results and the experimental data obtained for suspensions A and B (0.8%wt and 0.4% alginate respectively). We first notice that in both plots, there is a very good agreement between the numerical and the experimental results at very short time scales in the spreading phase. So the complex rheological behavior of the droplets are well described by the simulations.

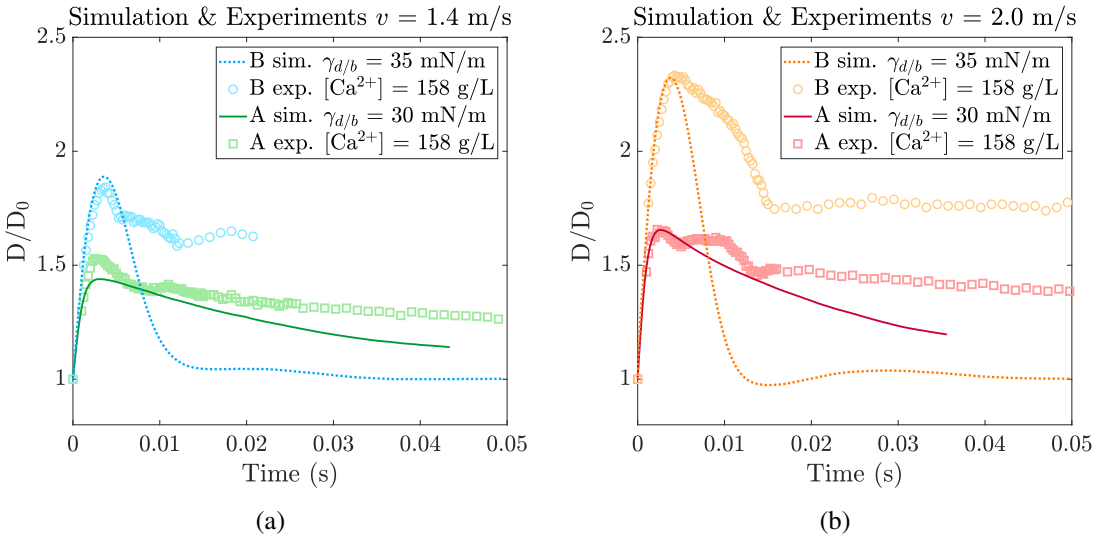

Figure 4.18 *Influence of rheology on droplet impact dynamics. Comparison between simulation and experimental results for suspension A (0.8%wt alginate) and suspension B (0.4%wt alginate). (a) v = 1.4 m/s ; (b) v = 2.0 m/s.*

In the case of suspension A (0.8%wt alginate), as explained previously, the overall shape of the curve is quite well predicted by the model for both impact speeds v = 1.4 m/s (a) and v = 2.0 m/s (b). For suspension B (0.4%wt alginate), however, just after reaching D_{max}, the experimental data and the simulation curves are quite different. We note that D/D_0 decreases very sharply in the model, because surface tension acts against viscosity, which is lower for suspension B than for suspension A. Therefore, there is very little viscous losses and the droplet relaxes until reaching a perfect sphere. On the contrary, in the experiments, we measure a rapid relaxation until 0.01 s, which then gives way to a very slow relaxation or no evolution at all, letting us think of a blocking mechanism linked to droplet solidification.

Overall the simulation results give us a good overview of the impact dynamics of our complex droplets falling into calcium baths. These studies are still ongoing to improve the model by implementing different surface tension values in order to describe more accurately the complexity of our system (interfaces air/droplet, air/bath and droplet/bath).

4.4 Conclusion

This chapter was dedicated to the impact dynamics of alginate-ceramic suspension droplets on a gelling bath. The major challenge consisted in studying the behavior of a non-Newtonian fluid droplet, falling into a liquid bath in which it starts to solidify promptly.

We have shown that the beginning of the impact dynamics (i.e. the spreading phase) is mainly controlled by **inertia** and **rheology**, hence the use of Reynolds number to predict the maximal droplet elongation. For non-Newtonian suspensions with high M_w alginate, D_{max}/D_0 is proportional to $Re_m^{1/(2m+3)}$ and for suspensions with low M_w alginate which present a Newtonian-like behavior, D_{max}/D_0 is proportional to $Re^{1/5}$. These scaling laws are also valid for experiments of impacts on solid surfaces, which is interesting for industrial applications.

The influence of the calcium concentration in the bath was also investigated. We observed no significant effect on the droplet maximal elongation for low impact speeds but for high impact velocities, the solidification of the droplet, which depends on Ca^{2+} concentration, seems to limit the maximal spreading.

Simulations of droplet impacts have been performed by applying a tunable surface tension between the yield-stress fluid droplet and the bath. By increasing the surface tension, the droplet maximal deformation is lowered and the relaxation phase is enhanced,

which is experimentally observed by increasing the calcium concentration in the bath. The model describes quite well the impact dynamics at very short time scales but at longer time scales, the gelation of alginate comes at play and makes the system more complex. That is why we need to study more carefully the relaxation dynamics, which is the object of Chapter 5.

Take-home messages of chapter 4

- The spreading phase is mostly driven by inertia (impact speed and drop size) and rheology (viscosity at high shear rates).
- The gelation of the drop (Ca^{2+} concentration) comes at play, especially at high impact velocities, to limit droplet spreading.
- There seems to be a parallel between the role of Ca^{2+} ions and the surface tension used in classic models: they restrict the elongation of droplets upon impact at short time scales and seem to enhance the retraction process at longer time scales.

Chapter 5

Relaxation

After the spreading phase comes the relaxation phase where the droplet sinks into the bath and relaxes towards a more spherical shape. In this chapter, we study the relaxation dynamics in order to identify the parameters influencing the change of shape. A better understanding of the relaxation phenomenon is the key towards improving the final shape of the beads.

5.1 Droplet relaxation: state of the art

Studies of stress relaxation and shape recovery of droplets after application of shear strains are reported in the literature [86–91]. In general, the models consider the force balance between the interfacial tension contribution and the viscous dissipation due to the flow in the deformed drops. Okamoto et al. [91] solved the equation by approximating the droplet shape as an ellipsoid of revolution. In all cases, the droplet shape evolution can be described by a characteristic time τ proportional to the capillary time $\tau_{cap} = \frac{\eta_{eff} R_0}{\gamma}$ where η_{eff} is the effective viscosity of the system (taking into account both the viscosity of the drop and the viscosity of the matrix), R_0 the effective radius of the droplet and γ the surface tension. For Newtonian fluids, using Palierne's emulsion model [92] we can write:

$$\tau = \tau_{cap} \times \frac{(2k+3)(19k+16)}{4 \times 10(k+1)}$$

with k the viscosity ratio η_d/η_m where η_d and η_m are respectively the Newtonian viscosity of the drop and the matrix.

To describe the droplet shape recovery, two parameters are usually studied: the deformation $\lambda(t) = \frac{a(t)-b(t)}{a(t)+b(t)}$ and the aspect ratio AR(t) = $\frac{a(t)}{b(t)}$ where a(t) and b(t) are the major and minor axes of the ellipse at time t. λ tends towards zero with an exponential decay of characteristic relaxation time τ [93, 94] as written in Equation (5.1).

$$\lambda(t) = \lambda_0 \, exp(-\frac{t}{\tau}) \tag{5.1}$$

In 2008, Assighaou et al. [93] evidenced a universal retraction process for a droplet embedded in an immiscible fluid of same density after a large strain jump. They considered that the key factor in the relaxation process of the drop is related to a decrease of the curvature gradient at the interface. These changes in curvature cause a pressure difference given by the Laplace law, along the deformed surface of the drop. This leads to internal convection in the drop in order to decrease the internal pressure gradient and recover a spherical shape.

By contrast, in our case, the droplet is a suspension containing zirconia, alginate and water, immersed in a water bath with calcium ions. Therefore, we do not expect any interfacial tension between the drop and the bath. So, what is the driving force of the relaxation in our system? In this chapter, we will study the effect of multiple parameters

on the relaxation mechanism of zirconia-alginate capsules through high-speed camera observations.

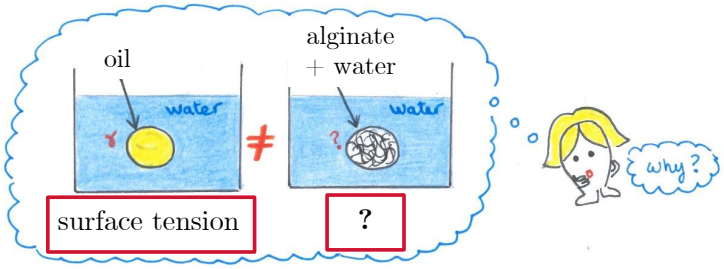

Figure 5.1 *Difference between the case of a droplet relaxing in an immiscible fluid and our case.*

5.2 Driving force of the relaxation

5.2.1 Experimental observations

First, the behavior of a droplet suspension falling into a pure water bath (without Ca^{2+} ions) is followed by high speed camera. The resulting image sequence is shown in Figure 5.2 (a). We observe that the droplet deforms largely upon impact before sinking to the bottom of the bath. Once at the bottom, the drop stays deformed as a pool and starts to dissolve in the bath after a few seconds instead of relaxing its shape. It is clear evidence that the 'real' surface tension between the suspension droplet and the bath is negligible.

When we add a small amount of Ca^{2+} ions in the liquid bath, we notice a slight change in the shape evolution of the droplet. In fact, as illustrated in Figure 5.2 (b), in a bath of concentration 1.58 g/L, the droplet spreads largely upon impact, similarly to the previous image sequence. Then, as the drop reaches the bottom of the bath, it adopts an elongated shape but does not dissolve, even at longer time scales.

As we continue to increase Ca^{2+} concentration (5 g/L), we can see in Figure 5.2 (c) that the relaxation phase is modified whereas the spreading phase is quite similar to the previous cases. As a matter of fact, from t = 0.1 s to t = 1 s, the droplet seems to relax slowly its ellipsoidal shape. However, after 5 s, the droplet tilts and bursts, showing the expulsion of some liquid suspension gelling as it encounters Ca^{2+} ions in the bath. As a result, the final bead turns out to be a spheroid with a defect due to the rupture of the gelling crust.

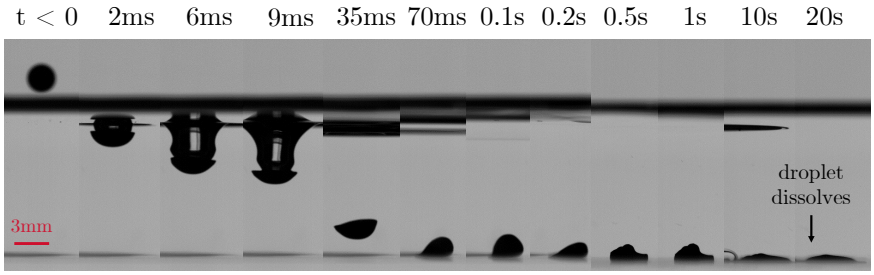

(a) *[$CaCl_2$] = 0 g/L.*

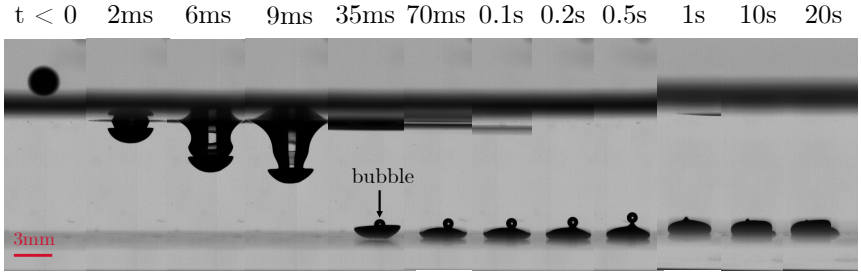

(b) *[$CaCl_2$] = 1.58 g/L.*

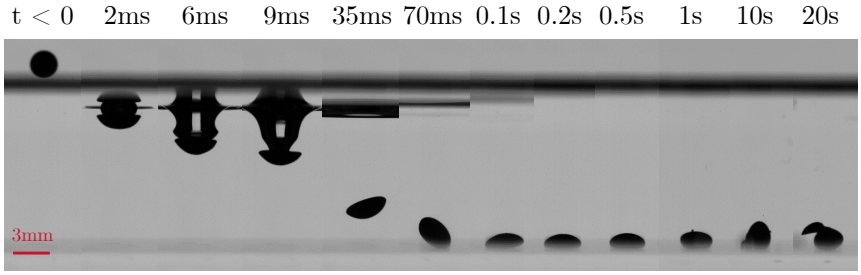

(c) *[$CaCl_2$] = 5 g/L.*

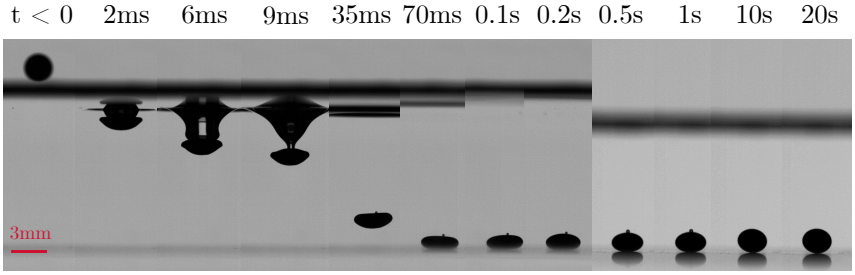

(d) *[$CaCl_2$] = 15.8 g/L.*

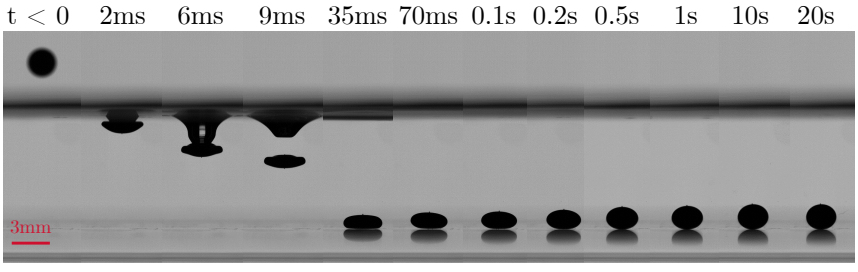

(e) *[$CaCl_2$] = 158 g/L.*

Figure 5.2 *Image sequence of a drop of reference suspension (0.8%wt alginate) falling into different calcium baths at v = 1.4 m/s.*

Figure 5.2 (d) exhibits the image sequence obtained when we add more calcium ions in the bath up to a concentration [$CaCl_2$] = 15.8 g/L. At short time scales, the droplet spreads upon impact, comparably to previously. However, we notice that the droplet starts to relax earlier, before reaching the bottom of the bath. In the end, the bead seems to recover a spherical shape.

Finally, as we increase 10 times the calcium concentration in the bath ([Ca^{2+}] = 158 g/L), as illustrated in Figure 5.2 (e), we observe that the droplet spreads a little bit less, showing an ellipsoidal shape very soon (t = 2 - 6 ms) rather than following the shape of the air cavity upon impact. Then, as the droplet sinks, it relaxes to a more spherical shape, even faster than in the previous case.

These images show that there is an evident correlation between the presence of Ca^{2+} ions and the capsules ability to relax. To quantify this phenomenon, we study the shape evolution of the beads through time by measuring their aspect ratio (AR) which is the ratio between the maximal and minimal diameter of the elongated droplet. Figure 5.3 exhibits the experimental data corresponding to the previous image sequences. We observe that in the bath of concentration 1.58 g/L, there is a slight relaxation from AR = 3.5 to AR = 3 but in the end, the droplet stays deformed. In the other baths, more concentrated in Ca^{2+} ions, the droplets aspect ratios decrease from AR = 3 to AR = 1.2 approximately, meaning that the droplets relax to more spherical shapes and become spheroidal gel beads. Nevertheless, we notice a difference in the kinetics of relaxation: the higher the calcium concentration in the bath, the faster the relaxation. For instance, at 0.2 s the capsule has an aspect ratio of 1.7, 2.1 or 2.4 depending on whether the bath has a concentration of 158 g/L, 15.8 g/L or 5 g/L. These results are in agreement with the previous observations and prove that there is a clear interdependence between the relaxation behavior and the quantity of gelation agents (Ca^{2+}). As we add calcium ions in the bath, the gelling droplet relaxes its shape.

5.2.2 Hypothesis for the driving force

In the previous paragraph, we have observed the relaxation process of elongated droplets towards more spherical shapes even though there is no surface tension between the drops and the bath, both composed of water. Moreover, this relaxation is faster for higher calcium concentrations. To account for this surprising behavior, we suggest the following mechanism (refer to Figure 5.4). As soon as the droplet is in contact with the bath, Ca^{2+}

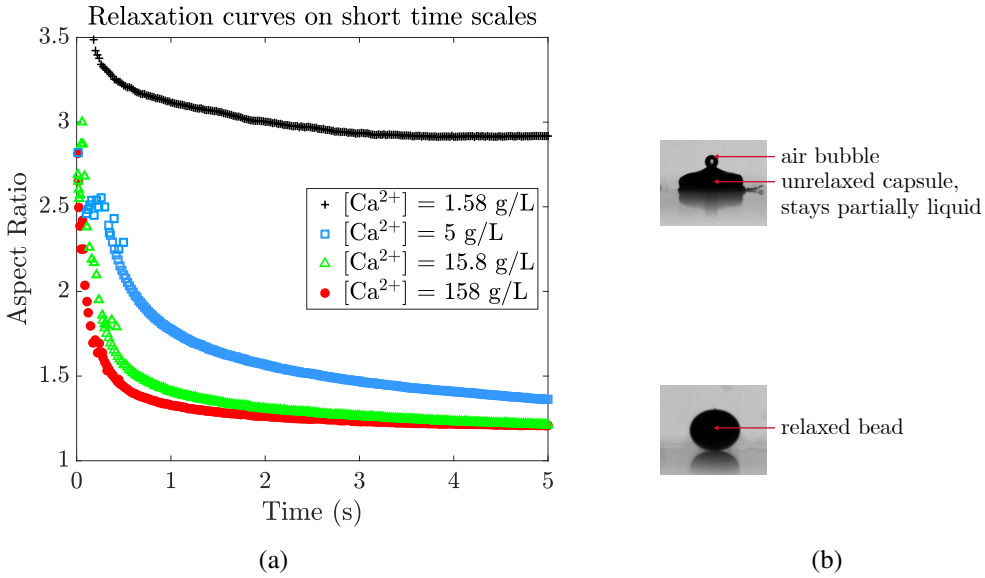

Figure 5.3 *(a) Relaxation curves in linear scale for a droplet of suspension A (0.8%wt alginate) in different gelling baths ([Ca^{2+}] = 1.58 - 158 g/L). (b) Corresponding images of the beads final shape.*

ions diffuse inside the drop and locally transform the slurry into a gel. Thus a solid-like membrane forms at the surface of the drop (represented in red in the drawing), and gradually thickens as Ca^{2+} diffusion proceeds. In addition, syneresis takes place, meaning that water is expelled from the gel-like region (phenomenon described in Chapter 3). As a result, the membrane is under tensile stress. This tension in the membrane gives rise to a pressure gradient inside the drop due to the different curvatures of the elongated shape. This generates a flow of liquid inside the droplet going from the regions of high curvatures (left and right extremities) to regions of smaller curvatures (top and bottom of the ellipse). Consequently, the capsule relaxes its shape, as we can see in Figure 5.2 (e).

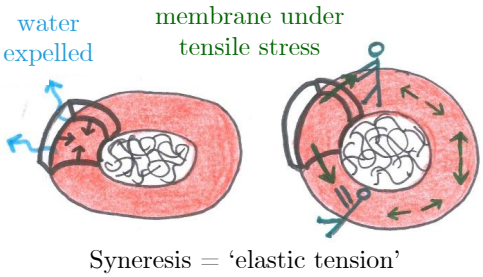

Figure 5.4 *Drawing explaining the consequence of syneresis phenomenon on a gelling deformed droplet.*

When the bath concentration is too low, it seems that there is not enough calcium ions to form a homogeneous gelled membrane around the droplet and therefore, the syneresis is probably very weak, resulting in no tensile stress in the membrane to drive the relaxation mechanism. That is why the droplets do not relax when immersed in a bath of concentration [Ca^{2+}] = 1.58 g/L.

In the more concentrated baths (5 g/L, 15.8 g/L and 158 g/L), the droplets have the same behavior upon impact and thus similar aspect ratios just after passing through the interface at 0.01 s. However, we observe a faster relaxation process as Ca^{2+} concentration increases. This can be directly linked to the weight loss and gel thickness measurements shown previously in Figure 3.8 (a) and Figure 3.14 (a) of Chapter 3. We demonstrated that the higher the calcium concentration, the faster the gel front and the sooner the weight loss due to syneresis, thus resulting in a faster relaxation mechanism.

We now try to evaluate the elastic tension in the membrane. It depends on the elastic modulus of the gelled membrane E, its thickness h and the syneresis strain ϵ_0:

$$T = E \times \epsilon_0 \times h$$

Referring to Figure 3.8 (a), the reference suspension looses approximately 10% of its initial weight, which corresponds to a volume loss $\delta V \simeq 15\%$ to reach an equilibrium state. In 3D, the syneresis strain can then be calculated as: $\epsilon_0 \simeq \delta V/3$. We assume that as soon as the droplet touches the calcium bath, a thin gelled membrane forms, and we can evaluate its thickness using the diffusion model established previously in Figure 3.8 (a). At short time scales (t $\approx$ 20 ms - 0.2 s at the beginning of the relaxation phase), we find a gel thickness h(20 ms - 0.2 s) $\approx 2 - 10\ \mu$m.

We also suppose that this thin gelled membrane is at its final equilibrium state, meaning that it looses 15% of its volume by syneresis and has a modulus E $\approx 10^4 - 10^5$ Pa similar to the one measured in Section 3.3.3 f) on macroscopic cylinder gels. These assumptions allow us to evaluate the elastic tension $T \simeq 1 - 50$ mN/m which is comparable to a typical liquid surface tension value. Furthermore, to reinforce this comparison, we note that the drop/bath surface tension used in the numerical model in Section 4.3 to describe the impact dynamics of droplets falling into a calcium bath of concentration 158 g/L was of the same order of magnitude: $\gamma_{d/b} = 20$ mN/m.

In short, as the droplet meets the calcium bath, it starts to gel and expels water through syneresis, which puts its outer membrane under stress. This elastic tension T mimics the

role of a surface tension: it drives the capsule relaxation mechanism. However, contrary to the case of a surface-tension driven relaxation mentioned in the state of the art Section 5.1, our capsules do not relax entirely: their final aspect ratio is 1.1 at best as illustrated in Figure 5.3. To understand this result, we must investigate the obstacles to relaxation.

5.3 Obstacles to relaxation

The viscosity of the liquid core can slow down shape recovery or even stop it completely if there is a threshold. There is another possibility, however: since the membrane turns solid and increases in thickness, it becomes more and more rigid, and can block further relaxation. Below, we examine these two possible obstacles to the relaxation mechanism.

5.3.1 Suspension viscosity

As explained in the state of the art (Section 5.1), we expect viscosity to be responsible for the slowing down of the relaxation mechanism. In fact, it has been reported that the characteristic relaxation time is proportional to the viscosity ratio $\eta_{\text{droplet}} / \eta_{\text{matrix}}$. This has been verified in Chapter 4 in the numerical model showing the spreading and early relaxation dynamics of droplets of suspension A (0.8%wt alginate) and B (0.4%wt alginate) in Figure 4.18. We observed a much faster shape recovery in the case of suspension B, with lower viscosity.

Experimentally, however, the suspension viscosity and the gel mechanical properties are linked and cannot be decorrelated. In fact, we have shown in Chapter 2 that we can tune the rheological behaviors of our suspensions by changing alginate concentration and/or alginate molecular weight. By doing so, we know from Chapter 3 that we modify simultaneously the syneresis phenomenon (i.e. the driving force of the relaxation) and the mechanical properties of the final gel.

Nevertheless, we decide to study the shape relaxation for suspensions B, A and C, with increasing alginate concentrations (0.4%wt, 0.8%wt and 1.6%wt respectively). In Figure 5.5, we plot the reduced aspect ratio (AR divided by the initial aspect ratio AR_i) against time for these three suspensions. We observe that the less viscous droplet has a quicker relaxation whereas the most viscous one (suspension C) keeps the same shape before and after impact suggesting that all the kinetic energy is transformed into viscous dissipation.

Actually, in addition to viscous effects, the relaxation kinetics depends on other parameters. Indeed, we have shown in Chapter 3 that a lower alginate concentration gives a higher syneresis, hence a higher relaxation driving force. So the observed quicker relaxation can be due to a greater syneresis as well as a more deformed shape upon impact, giving rise to a higher pressure gradient in the drop.

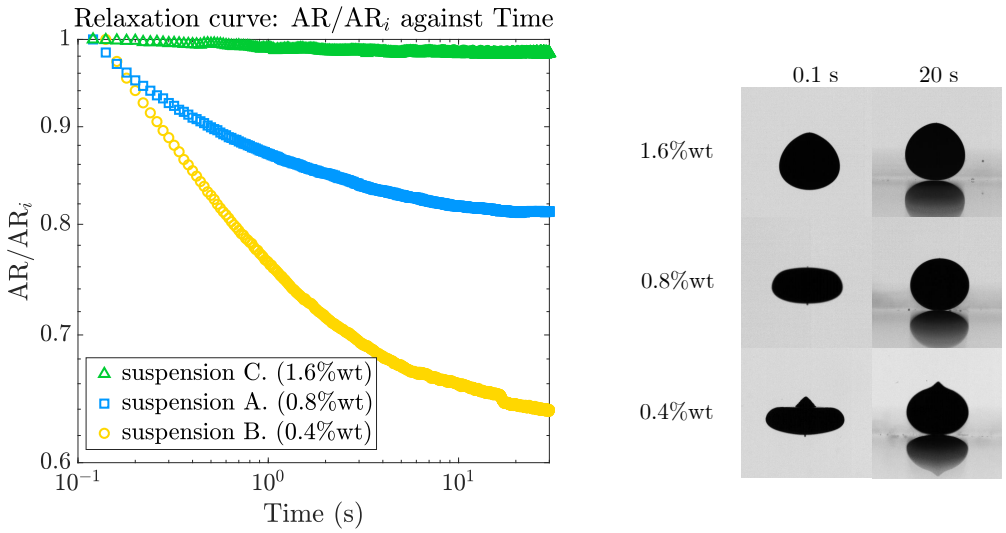

Figure 5.5 *(a) Relaxation curves of droplets of suspension A, B and C falling at 0.89 m/s in a bath of concentration [Ca^{2+}] = 158 g/L. We follow the evolution of AR/AR$_i$ (where AR$_i$ is the initial aspect ratio at t = 0.1 s). (b) Pictures of the immersed droplets, before and after relaxation (at t = 0.1 s and t = 20 s).*

If viscosity was the only resistance mechanism, the capsule would always recover totally its spherical shape because there is no threshold (see Section 5.4). In our case, capsules are frozen in a deformed state (AR > 1). Therefore, another blocking mechanism must be taken into account.

5.3.2 Gel mechanical properties

As discussed above, it is difficult to decorrelate experimentally the gelled membrane modulus value from the suspension viscosity because they are both strongly related to the quantity of alginate in the suspension.

Therefore, in the present paragraph, we choose to study the effect of gelation speed, related to membrane thickness and thus to bending rigidity, by changing the calcium concentration in the bath. In fact, we have seen in Chapter 3 that the membrane thickness

grows faster when Ca^{2+} concentration increases. As the gel crust thickens, the tensile stress in the membrane increases but the energy required to bend it increases as well. Therefore, we may question whether the time at which the droplet stops relaxing occurs for a critical gel thickness.

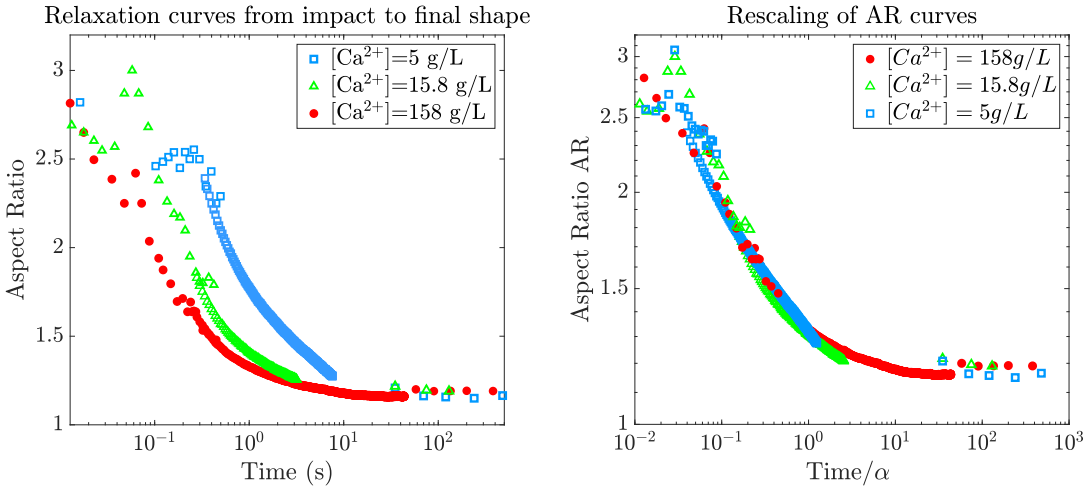

Figure 5.6 *(a) Extended log-log relaxation curves: from short time scales to the end of relaxation (i.e. the final shape of the capsule). (b) Rescaling of extended relaxation curves with α = (1, 2, 6) for [Ca^{2+}] = (158 g/L, 15.8 g/L, 5 g/L) respectively.*

We refer to Figure 5.6 (a) where the aspect ratio is plotted against time during the relaxation step at short and long time scales at constant impact speed and changing Ca^{2+} concentration. We find that we can rescale the curves by applying a multiplication factor $1/\alpha$ on the x axis with α = (1, 2, 6) for [Ca^{2+}] = (158 g/L, 15.8 g/L, 5 g/L) respectively. All the data points collapse on a single master relaxation curve as shown in Figure 5.6 (b), implying that the calcium concentration determines the relaxation kinetics. We observe that the higher the Ca^{2+} concentration, the faster the shape recovery. In fact, increasing the bath concentration ensures a faster gelation and so a faster syneresis, which drives the relaxation step.

Looking closer at the plot (b), we measure that 99% of final AR value is reached at Time/α = 10, corresponding to end relaxation times of 10 s, 20 s and 60 s for a droplet in a bath of concentration [Ca^{2+}] = 158 g/L, 15.8 g/L and 5 g/L respectively. Using the evolution of h with time shown in Figure 3.14 (a), we can evaluate the thickness of the capsule's gelled membrane when the relaxation mechanism stops. We obtain: h_{158} = 160 μm, $h_{15.8}$ = 150 μm and h_5 = 165 μm. Thus, we obtain a critical thickness value $h_c \approx$

155 μm above which the capsule is stuck in its shape. This result is consistent with our hypothesis that on top of viscous dissipation described in the literature, there is a another mechanism limiting the relaxation: the stiffness of the capsule's gel crust.

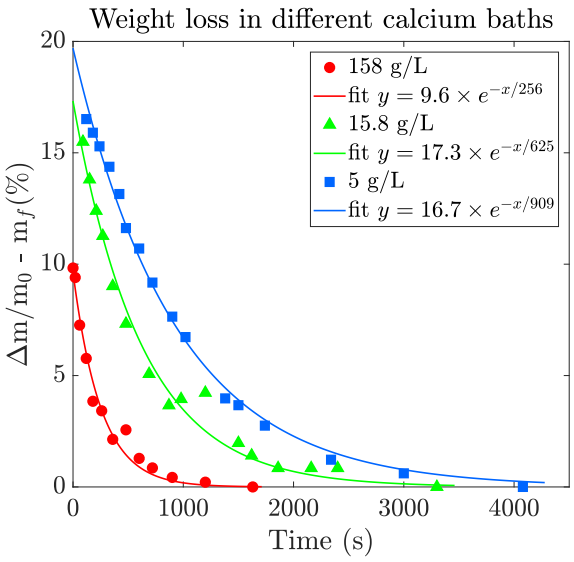

Figure 5.7 *Weight loss measurements on 3 mm beads in baths of concentration [Ca^{2+}] = (158 g/L, 15.8 g/L, 5 g/L. In order to fit the data points with an exponential law, we shift all the data up to positive values. To do so, we plot the relative weight loss $\frac{m-m_0}{m_0} - m_f$, where m_0 and m_f are the initial and final bead weight respectively.*

Interestingly, we find that the beads stop relaxing although they are not entirely gelled. Indeed, the gelled membrane thickness is about 155 μm while the capsule radius is 1.2 mm. Using the equations of Figure 3.14 (a) giving h(t), we can calculate the total gelation time for each calcium concentration:

$$t_{gel,158} \approx 345 \text{ s} \quad ; \quad t_{gel,15.8} \approx 780 \text{ s} \quad ; \quad t_{gel,5} \approx 1490 \text{ s}.$$

These roughly correspond to the characteristic times of the exponential laws describing the weight loss measurements : $\tau_{158} = 256$ s, $\tau_{15.8} = 625$ s and $\tau_5 = 909$ s (see Figure 5.7). The last one is not a perfect match because it is a more complicated case where the liquid core swells at the same time (see Section 3.2.2).

5.4 Stress estimation

Since it is difficult to decouple the rheological properties from the mechanical properties and the syneresis extent, we will estimate roughly the orders of magnitude of the stresses at play in this part.

Tension Syneresis puts the gelled crust under tension with an elastic tension T. We simplify the problem by looking at a 2D ellipsoid, slightly deformed from it original spherical shape: $a = R_0 + \delta R$ and $b = R_0 - \delta R$ (see Figure 5.8). The elastic tension in the membrane creates a shear stress inside the liquid core of the capsule: due to the curvature gradient, a difference of pressure is induced, creating a flow of liquid from the sides to the top and bottom of the ellipsoid. As a result, in comparison with the Young - Laplace equation ($\Delta P = 2\gamma/R$) giving the pressure in a droplet of radius R and surface tension γ, the pressure gradient induced in the liquid core of the capsule in our case can be estimated as follows:

$$\Delta P = T \times (\frac{1}{R_0 - \delta R} - \frac{1}{R_0 + \delta R})$$

where T is the elastic tension in the gelled membrane playing the part of the surface tension (see Equation 5.2.2). For small deformations ($\delta R \ll R_0$), we can make the following approximation:

$$\Delta P \sim T \times \frac{2\delta R}{R_0^2}$$

In order of magnitude, for a drop of suspension A:

$$\Delta P \sim \frac{2 \times T}{R_0} \times \frac{\delta R}{R_0} \approx \frac{2 \times T}{10^{-3}} \times 10^{-1}$$

As we mentioned previously in Section 3.3.3.f), the modulus value is subjected to errors and varies between 10^4 Pa and 10^5 Pa, giving an elastic tension $T \simeq 1 - 50$ mN/m, which leads to a range of shear stresses inside the capsule: $\Delta P \approx 1 - 10$ Pa.

Viscous stress Drop retraction is slowed down by viscous losses inside the liquid core. The resulting stress can be defined as $\sigma_{visq} = \eta \times \dot{\gamma}_{eff}$, where $\dot{\gamma}_{eff}$ is the effective shear rate during relaxation. Once the droplet gets through the interface and starts to relax,

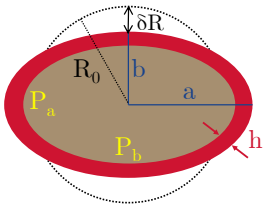

Figure 5.8 *Schematics of an ellipsoidal droplet (deformed from a sphere of radius R_0), with a gelled membrane of thickness h.*

the applied shear rate decreases, so the viscosity of the droplet increases. The best way to evaluate the effective shear rate at stake is to analyze the droplet shape at the early stages of the retraction process. We can therefore write the following approximation: $\dot{\gamma}_{eff} \approx \frac{R(t+\delta t)-R(t)}{R(t)\times\delta t}$.

$$\sigma_{visq} = \eta(\dot{\gamma}_{eff}) \times \frac{R(t+\delta t) - R(t)}{R(t) \times \delta t}$$

We choose a time step $\delta t = 0.1$ s, and with image analysis, we find, in order of magnitude, for the suspension A: $\dot{\gamma}_{eff} \approx 0.5\ s^{-1}$. Looking at the flow curve established in Chapter 2, we measure $\eta(\dot{\gamma}_{eff}) \approx 2$ Pa.s, which leads to:

$$\sigma_{visq} \approx 2 \times 0.5 \approx 1 \text{ Pa}$$

Here again, this value is subjected to discussion. In fact, the effective shear rate and the suspension viscosity are not fixed, they evolve with time during the relaxation process. Overall, the viscosity can be estimated as $\eta \approx 2 - 20$ Pa.s. Therefore, $\sigma_{visq} \approx 1 - 10$ Pa.

Yield-stress Another obstacle to relaxation, linked to the suspensions rheological properties, is the yield-stress σ_0. In fact, yield-stress fluids can be stuck in a deformed shape if their yield-stress value is higher than the driving stress of the retraction. In our case, the yield-stress values are too low (see Table 2.2) to stop the relaxation mechanism:

$$\sigma_0 \approx 0.3 \text{ Pa}$$

Bending stress Let us calculate the stress required to bend a membrane of thickness h and modulus E. To simplify the problem, we consider a thin plate of length R_0 and

thickness h (see Figure 5.9). The bending energy per unit length can be written as $\mathcal{E}_{bend} = Eh^3C^2$ where the curvature is $C = \frac{\partial^2 y}{\partial x^2} \approx \delta/R_0^2$. So, from the starting curved configuration, the total energy after flattening is:

$$\mathcal{E}_{bend} = \frac{Eh^3}{R_0^4}(\delta - \delta_0)^2$$

The bending stress can then be deducted as follows:

$$\sigma_{bend} \approx \frac{Eh^3}{R_0^4}(\delta - \delta_0) \approx E\left(\frac{h}{R_0}\right)^3 \frac{\delta R}{R_0} \tag{5.2}$$

Of course this is just an approximation because in our case the membrane is ellipsoidal and so in 3D we would have to take into account all the curvatures of the system. Nevertheless with this approximate calculation, we notice that the bending stress becomes relevant (i.e. of the same order of magnitude than the driving stress due to syneresis $\Delta P \simeq$ 1 - 10 Pa) for a thickness h = 50 - 210 μm, which is consistent with the critical thickness $h_c \approx 155$ μm calculated earlier in Section 5.3.2. In fact, in order of magnitude, for a drop of suspension A, with E = 10^4 - 10^5 Pa and h = h_c = 155 μm, we find:

$$\sigma_{bend} \approx E \times \left(\frac{155 \times 10^{-6}}{10^{-3}}\right)^3 \times 10^{-1} \approx 3 - 30 \text{ Pa}$$

For lower thickness values, the bending stress is lower than the driving syneresis stress and so the droplet continues to relax, being only slowed down by viscous stresses.

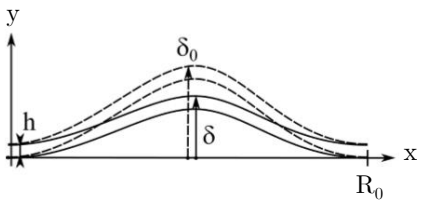

Figure 5.9 *Thin plate of thickness h and length R_0, at initial curved state in dashed lines, and final more flattened state in solid lines.*

Gravity stress As the droplet lays at the bottom of the bath during its relaxation, we can ask ourselves if the gravity plays a part in keeping the capsule deformed. We can

write the stress as follows:

$$\sigma_g = \Delta\rho\, g\, b$$

where $\Delta\rho \approx 0.4$ g/cm^3 is the density difference between the droplet and the bath and b is the height of the deformed capsule, i.e. its minor axis. The resulting order of magnitude is:

$$\sigma_g \approx 400 \times 10 \times 10^{-3} \approx 4 \text{ Pa}$$

This value is non negligible as it is of same order of the viscous stress (1 - 10 Pa). As a matter of fact, we see in Figure 5.2 (a) that in the non-gelling case, the droplet spreads as a pool at the bottom of the bath due to gravity. We can therefore imagine that in the gelling cases, the gravity also plays a part and acts against relaxation.

To sum up, as the droplet reaches the calcium bath, it starts to gel and syneresis puts the capsule under tension. This tension results in a pressure gradient inside the liquid core of the drop, estimated to vary from 1 Pa to 10 Pa, driving the shape relaxation. The suspension yield stress (0.3 Pa) is too low to resist such a relaxation, especially at the beginning of the retraction process. Then, at longer time scales, other obstacles of much higher importance will come into play so we choose to neglect the yield stress. However, the viscosity of the liquid core participates in energy dissipation and slows down the relaxation. The associated viscous stresses vary approximately from 1 Pa to 10 Pa. In addition to this viscous effect, a time-independent stress linked to gravity, of non negligible order of magnitude 4 Pa, limits further relaxation. As the gelation continues, the tension T increases proportionally to the gel thickness h, so the driving force of the relaxation increases. But at the same time, a new obstacle appears: it becomes more and more difficult to bend the gel membrane to further relax. This bending stress grows proportionally to h^3, much faster than the driving stress of the relaxation. That is why, above a critical gel thickness of 150 - 160 μm, the capsule is frozen into an elongated shape.

5.5 Simulation & comparison with experiments

5.5.1 Principle

The goal of the simulation is to verify our hypotheses. In other words, we want to evaluate whether a membrane contraction enables the droplet to relax and whether a

solid membrane can block the retraction process. The simulations were performed by Etienne Barthel (laboratory SIMM, ESPCI Paris).

The major problem is to incorporate in the simulation the transformation of the material from viscous liquid to solid. From the two possible frameworks, eulerian and lagrangian, we choose the second, which is more adequate for solids. The viscous liquid will be represented by a viscoelastic solid with a negligible terminal elasticity.

To solve for the deformation of this viscous liquid, we use a Galerkin method and mesh a 2D elongated droplet (i.e. an ellipsoid). We also consider a scalar field C, going from 0 to 1, proportional to Ca^{2+} concentration. We keep $C = 1$ at the surface of the droplet (equal to the concentration of the bath) and let C obey a standard diffusion equation inside the droplet, starting at t = 0.

The calcium concentration modifies the response of the viscoelastic material in two different ways. First, it transforms the viscous liquid into an elastic solid. Second, syneresis induces a contraction of the material. This is taken into account in the model by an eigenstrain (i.e. a pre-strain) proportional to C. Note that this eigenstrain is not relaxed by viscoelasticity because the relaxation time is very large in the transformed (solid) material. Since the transformed region forms a membrane around the almost incompressible core, the eigenstrain actually results in a tensile stress region at (and along) the surface of the droplet, effectively acting like a surface tension.

The diffusion equations related to calcium transport are the following. According to Fick's first law, the diffusion flux $\mathbf{J}$ is proportional to the negative of the concentration gradient:

$$\mathbf{J} = -D\,\nabla C$$

where D is the diffusion coefficient of calcium ions. Then, using the mass conservation, the second Fick's law gives us the corresponding standard diffusion equation, where Δ is the Laplace operator:

$$\frac{dC}{dt} + \nabla \,.\, \mathbf{J} = 0$$
$$\frac{dC}{dt} = D\,\Delta C$$

So we assume that the calcium ions follow a simple diffusion law: $C(t) \propto \sqrt{t}$.

Then, as explained earlier, to describe the capsule material, we must take into account

the fact that the core is liquid and the shell becomes solid as calcium ions diffuse in the material. We need to model where the core material turns from liquid to solid. For that purpose, we consider a viscoelastic material with a very low long term modulus. For small to moderate deformations, this material will effectively behave as a viscoelastic liquid. We further assume that the instantaneous modulus increases linearly with Ca^{2+} concentration up to a factor 100 at saturation in calcium concentration ($C = 1$). In addition, the relaxation time also increases with calcium concentration.

In the numerical model, we define a reduced time $\xi(t)$, used in all the calculations, related to actual experimental time t through an integral differential equation:

$$\xi(t) = \int_0^t \frac{ds}{A(C(s))} \quad \text{with} \quad A(C) = e^{3C}$$

To sum up, when the material turns solid because of the Ca^{2+} flow, we consider the following hypotheses:

- the modulus increases from 0.01 to 1 (proportionally to C)
- the characteristic relaxation time τ_r is 20 times larger
- the material contracts with a 10% maximal contraction $\epsilon = -0.1\,C$ with $0 < C < 1$.

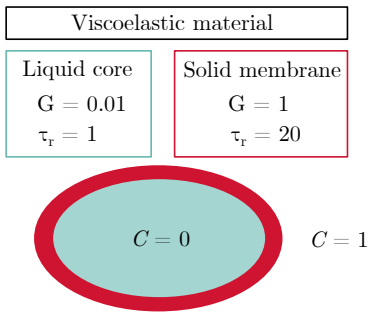

Figure 5.10 *Schematics explaining the boundary conditions in the numerical model.*

Once we have made these assumptions, we can study the influence of a wide range of parameters (wider than what is possible experimentally) on the relaxation of droplets. All the simulations are done on 2D droplets of given initial deformed shape (we choose the initial aspect ratio to be coherent with the ones we measure experimentally at t ≈ 0.1 s just after impact).

5.5.2 Model results and comparison with data

Firstly, when we perform the above calculations, we obtain a visible relaxation, which proves the consistency of our theory: the contraction of an ellipsoidal membrane (due to syneresis) is responsible for the relaxation of the capsule shape as shown in Figure 5.11.

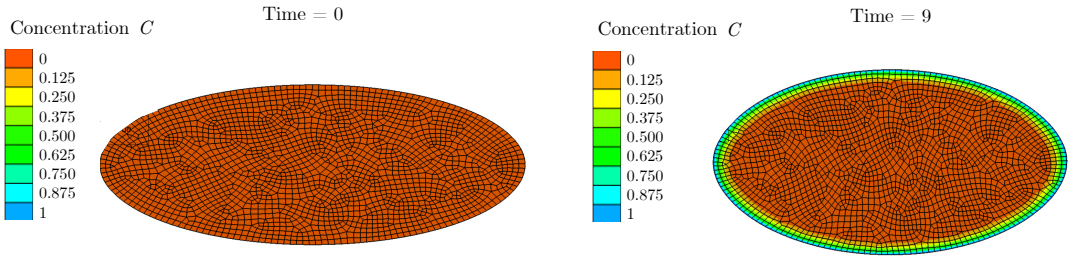

(a) *Image from simulation. Time = 0.* (b) *Image from simulation. Time = 9.*

Figure 5.11 *Images obtained from the simulation. (a) Initial state. (b) During the relaxation process.*

a) Influence of calcium concentration

The influence of calcium concentration is studied by changing the Ca^{2+} concentration gradient ΔC between the interior of the droplet and the exterior bath from 0 to 1. Referring to Figure 5.12 (a), we notice that for a bead having the same initial shape, the relaxation is faster when we increase ΔC. If we take a closer look at the blue curves, corresponding do $\Delta C = 1$, we notice that the major axis decreases abruptly from 1.4 to 1.05 for a time step $\delta T^* < 10$, and then decreases slowly with time. The minor axis, on the other hand, increases rapidly from 0.7 to 0.9 for $\delta T^* < 10$ and then decreases slowly with time. The first part of the curves ($\delta T^* < 10$) corresponds to the fast relaxation process due to the high calcium concentration in the bath, which makes perfect sense with our previous experimental observations. The second part of the curves ($\delta T^* > 10$), however, captures our attention because in the relaxation process where an ellipsoid becomes spherical, we usually observe the concomitant decrease of the major axis and increase of the minor axis. In our model, the syneresis is taken into account so during the gelation process, the capsule expels water and thus becomes smaller. That is why we observe such a decrease of both the major and the minor axes at longer time scales ($\delta T^* > 20$) when the relaxation process is blocked (due to the gel thickness) while the gelation and the syneresis still continue.

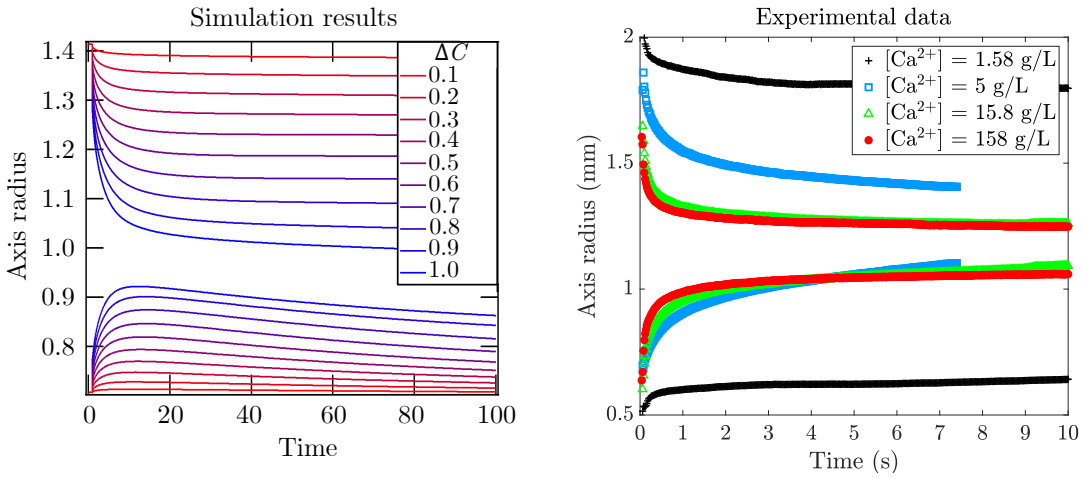

(a) (b)

Figure 5.12 *Influence of calcium concentration on the evolution of major and minor axes of the ellipsoid through relaxation process. (a) Simulation results with ΔC = 0.1 - 1. (b) Experimental data for a drop of suspension A (0.8%wt alginate) falling at 1.4 m/s in calcium baths of concentration [Ca^{2+}] = 1.58 - 158 g/L.*

It is interesting to compare these numerical results with our experimental data shown in Figure 5.12 (b). To do so, we plot the major and minor axes of droplets of suspension A (0.8%wt alginate) relaxing in different calcium baths of concentrations going from 1.58 g/L to 158 g/L. Overall, as we already showed previously in Section 5.3.2, increasing the calcium concentration results in a faster relaxation process, which is consistent with the simulation curves. For [Ca^{2+}] = 1.58 g/L, the minor and major axes vary slightly until reaching a plateau, keeping the droplet in a very elongated unrelaxed shape. The same evolution is noted in the model for small concentration gradients $\Delta C < 0.3$. On the contrary, for [Ca^{2+}] = 158 g/L, the major (resp. minor) axis decreases (resp. increases) abruptly in 1 s before reaching a plateau, meaning that the droplet has reached its final shape. For $\Delta C > 0.7$, the model gives a good description of the experiments at small time scales. However, at long time scales, the simulation results have a notable contribution of the droplet contraction with the decrease of both axes, whereas in the experimental data, we have to zoom in to see this volume loss.

b) Influence of suspension viscosity

As we mentioned earlier in Section 5.3.1, it is difficult to observe experimentally the influence of suspension viscosity on droplet relaxation because by changing the alginate

concentration, we not only change the viscosity but the extent of syneresis and the gel mechanical properties. In parallel, we also modify the initial deformation of the droplet upon impact as studied in Chapter 4. For that matter, the simulation appears as a very useful tool to study independently the effect of viscosity. In fact, in the simulation, the initial aspect ratio of the droplet is kept identical and we solely change the suspension viscosity by modifying its relaxation time τ_r from 0.1 to 30 (dimensionless). The higher τ_r, the higher the viscosity. The numerical results are illustrated in Figure 5.13. Contrary to the theory predicted in the state of the art (Section 5.1), the relaxation curves are not decreasing exponentially because all the mechanisms evolve simultaneously (the driving force and the obstacles) but the overall orders of magnitude of the decay are in agreement with the theoretical predictions: the higher the suspension viscosity, the slower the relaxation process.

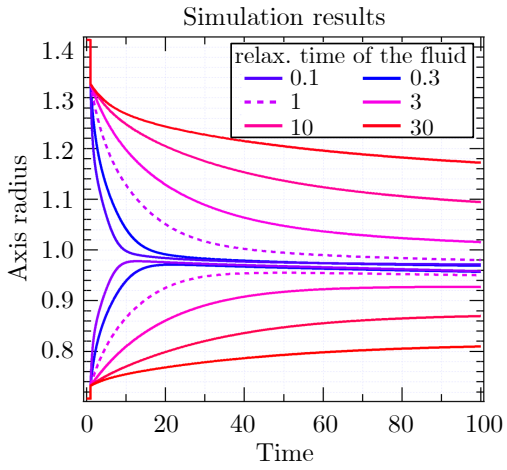

Figure 5.13 *Influence of viscosity on the evolution of major and minor axes of the ellipsoid through relaxation process. Simulation results.*

For $\tau_r = 0.1$, the major (resp. minor) axis decreases (resp. increases) abruptly ($\delta T^* < 10$), meaning that the relaxation process is very fast. Another notable point is that in this case the droplet becomes spherical at $\delta T^* \approx 20$ where the major and minor axes meet. On the contrary, for $\tau_r = 30$, the relaxation process is much slower, which is consistent with the theory presented in the state of the art (Section 5.1). In the intermediate case ($\tau_r = 1$, in dashed line), the relaxation kinetics is quite fast but not fast enough to relax to a perfect sphere. Indeed, the major and minor axes reach a plateau (or more precisely a decreasing plateau due to syneresis) and show a parallel evolution, meaning that the droplet is frozen in a deformed ellipsoidal state. This is probably due to the other obstacles to relaxation

identified earlier: the gelled membrane mechanical properties and gravity, which is in agreement with our experimental observations.

We cannot compare directly these numerical results with our experimental data for the multiple reasons given above. Nevertheless, the general shape of the simulation curves is in agreement with the experimental curves shown in Figure 5.5 (a).

Furthermore, an interesting conclusion arises: if we decrease the viscosity of a droplet without changing its elongation upon impact, its gel modulus or its syneresis mechanism, the droplet would be able to relax fast enough to reach a perfect sphere before being blocked by any obstacle.

c) Influence of gel modulus

In order to verify our assumptions on the effect of the gel stiffness, we change the solid elastic modulus from E = 0.03 to 30 (dimensionless) in the simulations. The results are plotted in Figure 5.14 (a). For $0.03 < E < 3$, we observe that the droplet shape recovery is faster for higher gel modulus. This is coherent with our hypothesis on the syneresis: the higher the modulus, the higher the elastic tension in the membrane and thus the higher the driving force of the relaxation. Another interesting result is obtained for very high modulus values. In fact, for E = 30, we notice that the major axis decreases sharply but reaches a plateau (more precisely a slow decreasing plateau because of syneresis) much sooner than for lower modulus values. This is in agreement with our previous discussion suggesting that increasing the gel modulus leads to an increase of the syneresis, hence a faster relaxation, but also a sooner arrest due to the greater stiffness of the gelled membrane which requires a higher energy to bend it.

Experimentally, to be as rigorous as possible, we compare droplets of equivalent initial radii after impact but with very different gel modulus values. Figure 5.14 (b) exhibits the relaxation curves of a drop of suspension A ([alginate] = 0.8%wt, M_w = 250 kg/mol) and a drop of suspension D ([alginate] = 5%wt, M_w = 60 kg/mol). The first one shows a fast relaxation stopping at approximately 5 s where its major and minor axes are around 1.3 mm and 1.09 mm respectively. The droplet of suspension D also seems to relax rapidly but reaches a plateau sooner at 2 s with radii sizes of 1.33 mm and 1.09 mm, hence with a more elongated final shape. These observations are similar to the simulation results comparing E = 10 (for drop A) and E = 30 (for drop D), which reinforces our hypotheses.

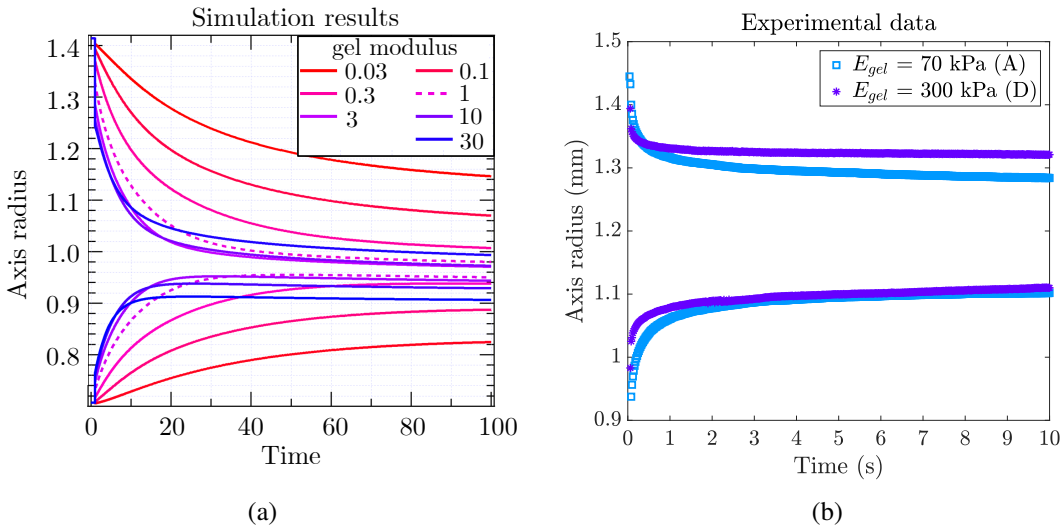

Figure 5.14 *Influence of the gel modulus on the relaxation process. (a) Simulation results (dimensionless quantities). (b) Experimental data: drops of suspension A ([alg] = 0.8%wt, M_w = 250 kg/mol), and D ([alg] = 5%wt, M_w = 60 kg/mol) falling into a bath of concentration [Ca^{2+}] = 158 g/L at 0.9 m/s.*

5.5.3 Limitations of the model

The simulation results confirmed our hypothesis on the driving force of droplet relaxation and the viscous and mechanical obstacles which oppose such a retraction. However, we observe some differences between the experimental data and the model when it comes to the influence of impact speed. In Figure 5.15 (b), we follow the experimental axis radii as a function of time and we observe that for high impact speeds, the initial aspect ratio is high and so the initial axis radii are very different. As mentioned earlier [93], the relaxation mechanism is also driven by the curvature difference at the surface of the droplet, leading to pressure gradients. So the higher the initial aspect ratio, the higher the pressure gradient, hence the high internal stresses driving the relaxation. As a matter of fact, experimentally, the highly deformed droplet (red circles) relaxes a lot (i.e. the difference between the initial and the final radius values is important) but keep an elongated shape in the end. On the contrary, the capsules starting with a low aspect ratio have a lower range of relaxation (light blue crosses).

Oppositely, the simulation results in Figure 5.15 (a) show a bigger range of relaxation for droplets starting with a lower aspect ratio. This is due to the fact that the tensile stress in the membrane leads to very localized flows in the right and left extremities of the ellipsoid. Therefore, the pressure gradients result in the motion of the liquid core

confined in the highly curved domains, which makes it impossible for the droplet to relax (see Figure 5.16).

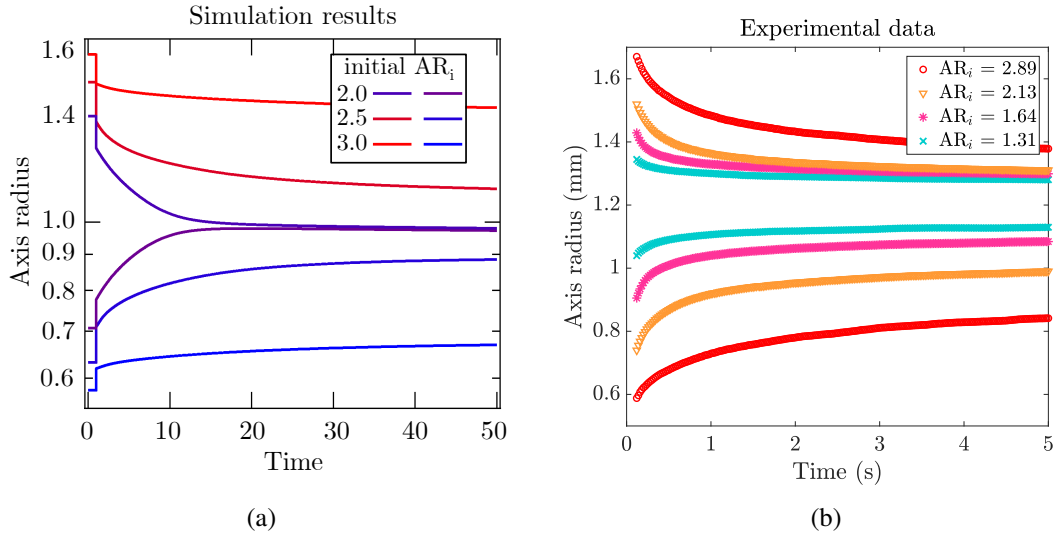

Figure 5.15 *Influence of the initial deformation (AR_i) on the evolution of major and minor axes of the ellipsoid through relaxation process. (a) Simulation results. (b) Experimental data: drops of suspension A ([alg] = 0.8%wt, M_w = 250 kg/mol) falling in a bath of concentration [Ca^{2+}] = 158 g/L with varying impact speeds from 0.6 m/s to 2.8 m/s.*

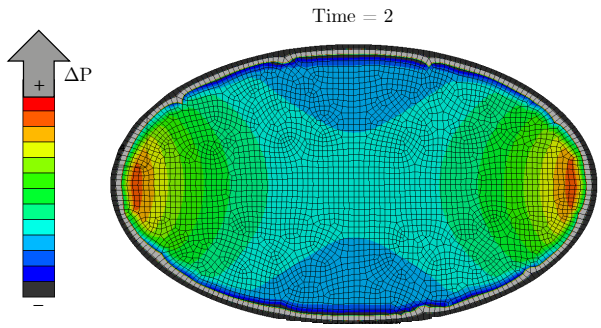

Figure 5.16 *Image resulting from the simulations giving the quantification of the pressure gradient inside the droplet. We notice that it is maximal and localized at the right and left sides of the droplet.*

The main limitation of the model comes from the fact that it is a 2-D model, not taking into account all the curvatures of the ellipsoidal droplet. Moreover, it is a simplified model, illustrating the relaxation mechanism through water loss by syneresis without including the other existing osmotic flows in the system. Other limitations come from

the approximate description of the diffusion and of the mechanical responses of the materials. In fact, we only consider one single relaxation time of the system while the relaxation curves show a non-exponential decay, suggesting a more complex behavior with many relaxation times. Furthermore, the standard diffusion model is used to describe the calcium ions entry in the droplet, but in the real system, the diffusion might be slowed down by the solid membrane in formation.

5.6 Conclusion

This chapter was dedicated to the relaxation mechanism of zirconia-alginate capsules after their deformation upon impact with the calcium bath. The syneresis phenomenon, during which the gel contracts and expels water, was observed. **Syneresis** puts the gelled membrane under tension, seemingly to the surface tension of a droplet in an immiscible fluid. This tensile stress gives rise to a pressure gradient inside the droplet which results in the relaxation of the elongated shape. By adding more calcium to the bath, the retraction process is accelerated. However, by doing so, the relaxation arrest is also reached earlier.

In fact, two main mechanisms are directly opposed to droplet relaxation. The first one is linked to **viscous stresses in the capsule liquid core**. The higher the viscosity, the higher the viscous drag force. The second obstacle to relaxation is related to the **mechanical properties of the gelled membrane** (its modulus and thickness). When the capsule membrane gets thicker (above a critical thickness $h_c \approx 155\ \mu$m), it requires too much energy to bend it. Therefore, the bead is frozen in a deformed shape before being totally gelled.

Take-home messages of chapter 5

- The syneresis phenomenon induces an elastic tension T in the gelled membrane. The resulting tensile stress drives the relaxation of the droplet, similarly to a classical surface tension between two liquids.
- The major parameters influencing the relaxation are: the Ca^{2+} concentration in the bath and the suspension composition (alginate and zirconia content as well as alginate molecular weight).
- Viscous dissipation, due to the viscosity of the liquid core, slow down the relaxation process.
- Mechanical properties of the gel membrane also oppose such a relaxation. They come at play over a certain critical thickness, over which the bending stress is too high compared to the driving stress. The relaxation process is then stopped and the droplet frozen in an ellipsoidal shape.

Chapter 6

Conclusion and perspectives

The main purpose of this study was to understand the mechanisms involved in the drip-casting process governing the final shape of the beads. Dripping process is the most classical way to produce monodisperse alginate beads. In this method, the alginate solution is extruded through a nozzle at a controlled volumetric rate and allowed to drip under gravity. The resulting droplet is collected in a calcium bath where it gels. Previous studies have described empirically the influence of several parameters (solution viscosity, tip size, impact speed, etc) on the size and shape of the final beads through trial and error works but droplet deformation dynamics during impact and gelation are rarely discussed.

In this thesis, we were interested in using this dripping technique to manufacture ceramic beads, as they are of great matter to Saint-Gobain. To do so, ceramic particles (zirconia in our case) were added to the alginate solution prior dripping. The system became more complex, which led us to divide our work into two main parts. The first one (Chapters 2 and 3) focused on the rheological characterization of the ceramic-alginate suspensions as well as their gelation mechanism when in contact with Ca^{2+} ions. The second part (Chapters 4 and 5) examined the droplet dynamics upon impact with the liquid bath, as well as its shape evolution with time during the gelation process.

We first studied in great detail the rheological behavior of zirconia-alginate suspensions and compared them with the Newtonian behavior of alginate solutions generally used in the literature (in Chapter 3). With this complete rheological characterization, we were able to describe the state of the suspensions at each step of the process (through the nozzle, during the fall, upon impact and during relaxation). We found that the addition of sodium alginate (M_w = 250 kg/mol) in a PAA-stabilized zirconia suspension, caused the zirconia particles to flocculate. This depletion-induced aggregation was suggested to be

responsible for the shear-thinning, yield-stress behavior of zirconia-alginate suspensions. Then, we evidenced an interesting point by adding smaller molecular weight alginate (M_w = 60 kg/mol) in a zirconia suspension. First, the resulting fluid exhibited a yield-stress due to zirconia aggregation. But after 48 hours of stabilization, the suspension showed a Newtonian behavior, with a viscosity staying approximately constant with shear rate, similarly to an alginate solution without particles. We explained this change in behavior by the adsorption of the shorter alginate chains onto the surface of zirconia particles, leading to their stabilization (deflocculation). So by changing the concentration and/or the molecular weight of sodium alginate in the suspension, we were able to control and cover a wide range of rheological properties (Section 2.5.3).

The next chapter of this first part (Chapter 4) was dedicated to the gelation properties of the previous formulations. We showed that they were subjected to syneresis, an osmotic phenomenon during which a polyelectrolyte gel expels its solvent. Through image analysis and weight measurements, we proved that the gelling capsules expelled water (Section 3.2). This volume loss was shown to be greater when the suspension was poorly concentrated in zirconia and alginate. For the suspensions with lower molecular weight alginates, the extent of syneresis was smaller, giving us the opportunity to identify another osmotic flow (inward or outward) linked to the ion concentration inside and outside the droplet. For instance, a droplet of suspension D (highly concentrated in low M_w alginate) falling into a poorly Ca-concentrated bath, swells due to the poor syneresis and the high inward flow of water. The droplet gelation mechanism regarding different experimental parameters being more clearly understood, we studied the mechanical behavior of the gelled beads (Section 3.3). By applying compression tests on beads and cylinders, we pointed out the viscoelasticity of suspension beads and were able to give an approximation of their elastic modulus ($E \sim 10^4 - 10^5$ Pa).

The next challenge of this thesis was to link the suspension rheological properties as well as the gel mechanical properties to the final shape of the bead. That is why, in the second part of this work, we analyzed the droplet dynamics upon impact with the liquid bath, and during the gelation process after impact. Chapter 4 was dedicated to impact dynamics. We first gave an overview of what has been done in the literature regarding drop impacts on solid or liquid surfaces. Despite the complexity of our system (a liquid droplet becoming solid during impact with a liquid bath), we managed to relate to existing models in order to predict the maximal spreading of droplets upon impact (Section 4.2.4). In fact, we showed that droplet elongation was mainly controlled by inertia and rheology

(i.e. impact speed and fluid viscosity). These results are of practical interest to Saint-Gobain because the maximal spreading ratio of a droplet can be predicted using a simple scaling law: $D_{max}/D_0 \propto Re_m^{1/(2m+3)}$ (m being the Hershel-Bulkley exponent, equal to 1 for Newtonian fluids) and verified easily looking at the drop deformation upon impact on a solid substrate.

After the spreading phase, the droplet evolves towards a more spherical shape. This relaxation behavior was the object of Chapter 5. The question that naturally arose was: why do we observe such a relaxation? In fact, in the literature the relaxation phenomenon is driven by surface tension but in our case, there is no real surface tension between the droplet and the liquid bath. To verify it, a drop of zirconia-alginate suspension was dripped into a bath of pure water (without calcium ions) and we observed its elongation upon impact and no relaxation but a progressive dissolution of the drop. By increasing the Ca^{2+} concentration in the bath, the relaxation was proven to be faster which led us to the very interesting following conclusion. The syneresis due to the fast gelation of the droplet, puts the outer gelled membrane under tensile stress, responsible for the capsule relaxation. The originality of our system is that an elastic tension takes the place of a classical surface tension to explain the shape evolution of deformed droplets. However, contrary to the typical systems studied in the literature, the final shape of the bead is not perfectly spherical. In fact, we identified two main obstacles to relaxation: viscosity, which slows down the retraction, and mechanical properties of the gelled membrane, which are responsible for the complete stop of the process. Therefore, we concluded that increasing Ca^{2+} concentration in the bath enhanced the syneresis and thus the relaxation process, but also accelerated its stoppage. A simplified summary of the key parameters at stake in the dripping process are shown in Figure 6.1.

To further improve the ceramic beads sphericity through drip-casting process, several paths could be investigated in future works.

First we must keep in mind that the gelled beads resulting from the drip-casting process are dried and then sintered. An ongoing study at Saint-Gobain Research on the effect of drying process on bead morphology has shown that the aspect ratio prior to drying is not always conserved according to formulations. In most cases, drying has negative consequences on the bead shape as an initial sphericity defect is aggravated by isotropic drying. However, this observation depends on the formulation and an interesting result has been obtained with low molecular weight sodium alginate. In that case, the widhdrawal ratio on the major axis is higher, which leads to a good aspect ratio

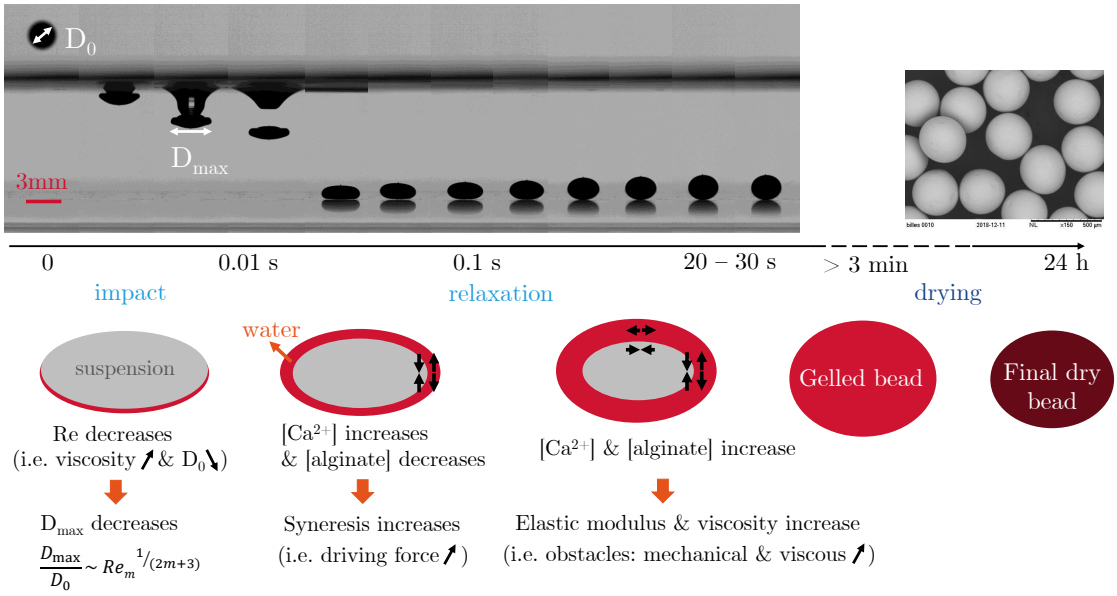

Figure 6.1 *Summary of the key parameters at each step of the drip-casting process.*

conservation after drying. It is a promising result still not fully understood: is it linked to the bead microstructure and porosity (i.e. zirconia distribution in the alginate matrix)?

Concerning the prediction of droplet spreading through simulation, we could think of improving the numerical model by implementing a surface tension between the droplet and the bath that evolves with time to mimic the varying syneresis due to the growing gel thickness.

From a more fundamental point of view, it would be interesting to study more deeply the syneresis phenomenon, associated with the alginate gelation kinetics. Preliminary results have shown that M/G ratio has no effect on droplet rheology and therefore no effect on the spreading behavior upon impact. However, in the literature it has been stated empirically that alginate M/G ratio as well as its molecular weight M_w modify the extent of syneresis, but this phenomenon has not been analyzed quantitatively and is still not well understood. Several influencing parameters have been identified in this work (alginate and zirconia concentrations, alginate molecular weight, calcium concentration in the bath), but other ones could be interesting to study (alginate M/G ratio, dispersing agent, temperature, etc). Temperature could have an effect on the gelation kinetics and therefore the driving force of the relaxation while M/G ratio is expected to modify the stiffness of the gel. Changing the dispersing agent could have an influence on the

suspension rheology and therefore the droplet deformation upon impact.

On a larger time line, it would be interesting to use the co-extrusion technique to produce alginate capsules as in [46]. This manufacturing process ensures the production of capsules of controllable and variable shell thicknesses, decorrelated from the liquid core viscosity. By doing so, we could study independently the effect of the liquid rheological behavior and the gel mechanical properties on the impact dynamics and the relaxation mechanism of droplets. We could also study in more details the influence of gel thickness and composition on syneresis without changing the liquid core and more importantly by controlling the ion quantity inside and outside the droplet to ensure no swelling or deswelling of the liquid core. Overall, the co-extrusion dripping process could be an interesting way to obtain a more controlled system to further understand the impact, gelation and relaxation dynamics of compound alginate droplets.

Appendix A

Relaxation of alginate droplets without zirconia

A.1 Experimental observations

Experiments are conducted on alginate solutions without particles. Figure A.1 illustrates the impact and relaxation behaviors of a drop of alginate solution at 13.1 g/L (M_w = 250 kg/mol) falling into calcium baths of concentrations [Ca^{2+}] = 15.8 g/L (a) and [Ca^{2+}] = 158 g/L (b). We first notice that it is difficult to follow the relaxation dynamics of a drop in a highly concentrated bath because the droplet does not stay at the bottom of the bath, it rises at the surface as it is less dense than the calcium solution at 158 g/L. We also observe that droplet relaxation seems to be less dependent on calcium concentration than in the case of zirconia suspensions. In fact, if we compare the image sequences, we can see that the alginate capsules have approximately the same relaxation behavior whether [Ca^{2+}] = 15.8 g/L or [Ca^{2+}] = 158 g/L.

Figure A.2 exhibits the comparison between the relaxation dynamics of a droplet of alginate solution without particles and a droplet of suspension A (with the same alginate concentration 13.1 g/L) in a bath of concentration [Ca^{2+}] = 15.8 g/L. The overall shape of the relaxation curve is similar between the two systems. The only difference is that the droplet without zirconia seems to relax more rapidly (the aspect ratio starts to decrease earlier) and the final shape of the bead is more spherical. In order to explain these observations, let us calculate the driving force and limiting forces in the case of an alginate droplet without particles and compare them with what we have previously calculated for the suspension A in Section 5.4.

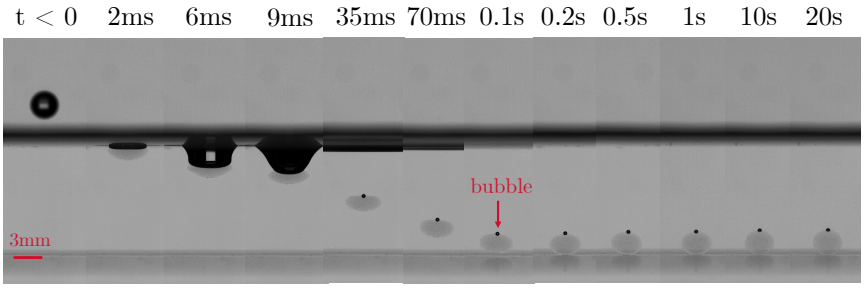

(a) $[Ca^{2+}] = 15.8$ g/L.

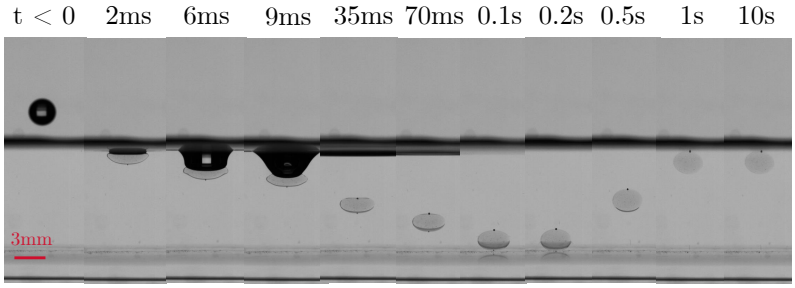

(b) $[Ca^{2+}] = 158$ g/L.

Figure A.1 *Image sequences of a drop of alginate solution at 13.1 g/L falling in calcium baths of different concentrations.*

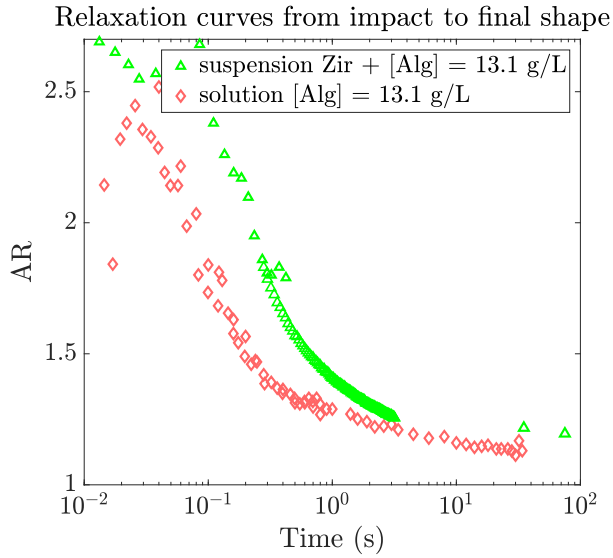

Figure A.2 *Relaxation curves: comparison between a droplet of reference suspension (A) and a droplet of alginate solution without zirconia gelling in a calcium bath of concentration* $[CaCl_2] = 15.8$ g/L.

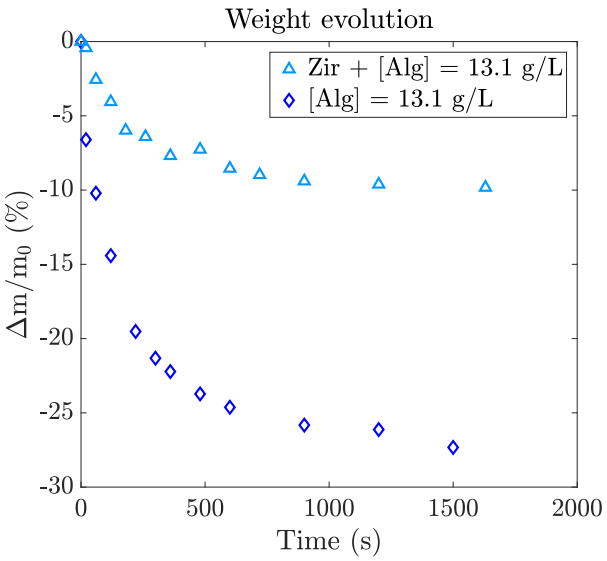

Figure A.3 *Weight loss measurements of a droplet of suspension A ([zirconia] = 40%wt and [alginate] = 13.1 g/L) and a droplet of alginate solution ([alginate] = 13.1 g/L) in a bath of concentration [$CaCl_2$] = 158 g/L.*

A.2 Estimating forces

Referring to the stress analysis in Section 5.4, we can estimate the stresses at play in the case of a droplet of alginate without particles.

- The elastic tension $T = E \times \epsilon_0 \times h$ is approximately of same order of magnitude than previously because the elastic modulus is twice as small as the one for suspension A ([zirconia] = 40% and [alginate] = 13.1 g/L) if we recall the stress - strain curve in Figure 3.24, but the syneresis is almost three times more important, as is shown in Figure A.3. These results lead us to $T \approx 1 - 75$ mN/m, resulting in a pressure gradient stress slightly higher than the one for suspension A: $\Delta P \approx 1 - 15$ Pa.

- The viscous stress is much lower in that case because the solution of alginate without particles has a lower viscosity, especially at low shear rates. We can calculate the resulting stress as follows: $\sigma_{visq} = \eta \times \dot{\gamma}_{eff} \approx 0.25 \times 0.5 \approx 0.1$ Pa.

- The bending stress linked to the mechanical properties of the gel is calculated using Equation (5.2). We find that it becomes of same order of magnitude than the driving tensile stress for a gel thickness h $\approx 50 - 250$ μm, which is a little bit higher than the critical thickness calculated for suspension A because the gel's elastic modulus is lower.

- The difference in density between the alginate solution and the calcium bath is smaller than in the previous case because of the high density of zirconia. However, as illustrated in Figure A.1, the alginate capsule without particles is sometimes less dense than the bath, which causes its rising to the surface of the bath. Nevertheless, with a density difference of $\Delta\rho \leq 0.1$ g/cm^3, the gravity stress becomes $\sigma_g \leq 1$ Pa.

Keeping in mind these orders of magnitude, we can compare the relaxation behaviors of a droplet of alginate solution at 13.1 g/L and a droplet of suspension A (see Figure A.2). We notice that the aspect ratio of the droplet without zirconia decreases earlier, which may be due to the higher syneresis, leading to a slightly higher driving force and a lower viscous brake. In fact, contrary to the case of suspension A, the droplet relaxes without being slowed down by viscosity. The only obstacle to relaxation in that case is the mechanical properties of the gelled membrane, which comes a little bit later. Indeed, we observe that the relaxation stoppage occurs at $t \geq 30$ s, which corresponds to a gel thickness of $h_c \approx 155$ μm, consistent with the range of critical thicknesses calculated in the previous paragraph. Therefore, with a slightly higher driving stress, and lower viscous dissipation, the alginate capsule relaxes faster and more than a capsule containing zirconia particles: its final aspect ratio is 1.13 compared to 1.20 for suspension A.

To put it in a nutshell, it is easier to make spherical beads with Newtonian alginate solutions without particles.

Appendix B

Relaxation of suspension droplets with low M_W alginate

B.1 Experimental observations

Throughout this manuscript, we have used and characterized four main suspensions. Among them, three (suspensions A, B and C) contain sodium alginate of molecular weight M_w = 250 kg/mol and the other one (suspension D) contains 5%wt of alginate of lower size M_w = 60 kg/mol. In Figure B.1, we show image sequences of droplets of suspension A and D respectively falling at 1.4 m/s and relaxing in a calcium bath of concentration $[Ca^{2+}]$ = 158 g/L.

The first pictures confirm what we have studied in Chapter 4. The droplet of suspension D is less deformed upon impact, because its viscosity is higher at the high considered shear rates. Then, at longer time scales, the capsule with low M_w alginate relaxes more slowly and less than the capsule of suspension A with longer alginate chains. The relaxation curves plotting the aspect ratio against time are shown in Figure B.2 (a). We can see that the droplet of suspension A has a higher aspect ratio at very short time scales ($t \leq 0.1$ s), but relaxes faster to reach a lower aspect ratio in the end (1.16 compared to 1.34 for suspension D).

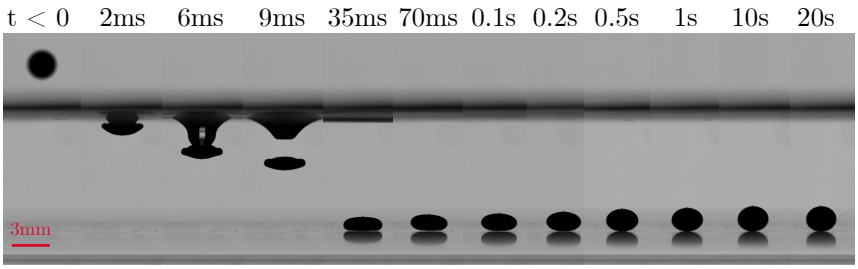

(a) *Suspension A (0.8%wt 250 kg/mol alginate) in [Ca^{2+}] = 158 g/L.*

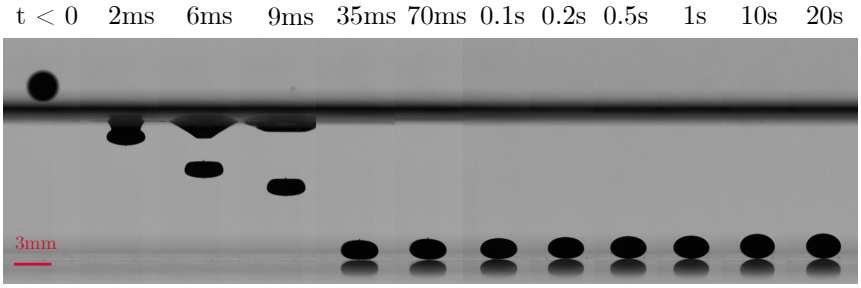

(b) *Suspension D (5%wt 60 kg/mol alginate) in [Ca^{2+}] = 158 g/L.*

Figure B.1 *Comparison of image sequences of a drop of reference suspension (A) and suspension D with shorter alginate chains.*

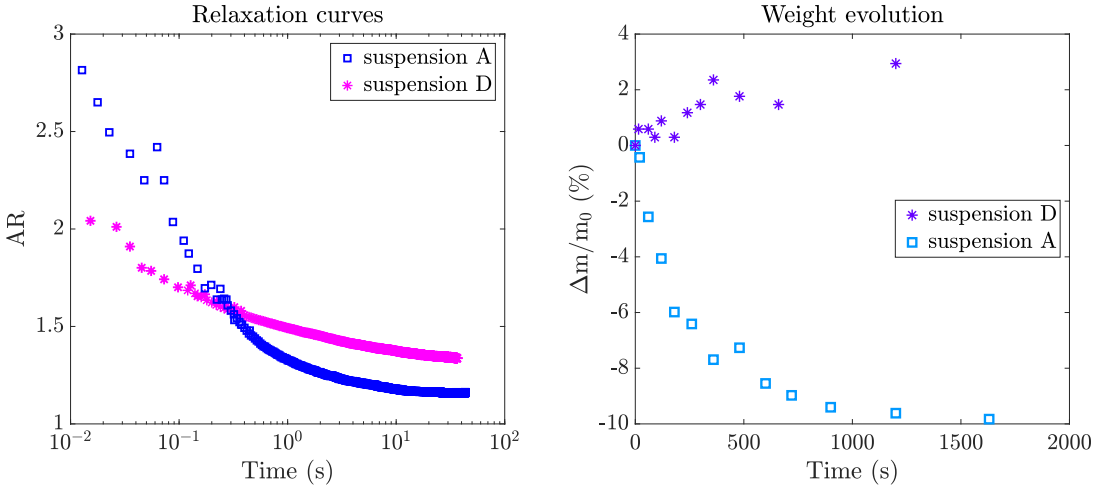

(a) (b)

Figure B.2 *Comparison between the relaxation behaviors of a droplet of suspension A ([alginate] = 0.8%wt, M_w = 250 kg/mol) and a droplet of suspension D ([alginate] = 5%wt, M_w = 60 kg/mol) in a bath of concentration [Ca^{2+}] = 158 g/L. (a) Relaxation curves (log-log scale). (b) Weight evolution.*

B.2 Discussion

In Chapter 3, we evidenced the existence of another osmotic flow, in addition to syneresis. In Figure B.2 (b), we exhibit the weight measurements for beads of suspension A and D through time. We noticed that instead of loosing weight because of syneresis, the bead of suspension D swells because of the higher ion concentration inside the droplet. In the present case, the overall bead volume increases of 3%. It is difficult to dissociate the contributions of syneresis and the swelling but in Chapter 3, we showed that the syneresis was much lower for suspension D than for suspension A. As a consequence, even with an elastic modulus three times higher, the tensile stress linked to syneresis is expected to be very small. As a matter of fact, in Figure B.2 (a), we measure a relaxation twice as slow for suspension D than for suspension A (looking at the slope of the curves at short time scales t < 0.1 s).

As for the obstacles to the relaxation mechanism, the viscous stresses are slightly lower ($\sigma_{visq} \approx 0.7$ Pa) because of the Newtonian-like behavior, giving a lower viscosity at low shear rates. The gel mechanical properties, however, are enhanced: we measured an elastic modulus three times higher for suspension D than for suspension A, making it more difficult to bend.

All these assumptions lead us to believe that the driving force of the relaxation (mostly syneresis) is lower for suspensions containing a high concentration of alginate of low molecular weight, and the blocking mechanism is higher, hence the overall slow relaxation process and deformed final shape.

Bibliography

[1] A. Penman & G. Sanderson; "A Method for the Determination of Uronic Acid Sequence in Alginates"; Carbohydrate Research **25**, pp. 273–282 (1972). ISSN 00086215. 10, 20

[2] G. S. Manning; "Limiting Laws and Counterion Condensation in Polyelectrolyte Solutions I. Colligative Properties"; The Journal of Chemical Physics **51**, pp. 924–933 (1969). ISSN 0021-9606, 1089-7690. 10

[3] F. Oosawa; *Polyelectrolytes* (M. Dekker, New York) (1971); ISBN 978-0-8247-1505-2. 10, 11

[4] P. G. de Gennes, P. Pincus, R. M. Velasco & F. Brochard; "Remarks on Polyelectrolyte Conformation"; Journal de Physique **37**, p. 12 (1976). 11

[5] A. Khokhlov & K. Khachaturian; "On the Theory of Weakly Charged Polyelectrolytes"; Polymer **23**, pp. 1742–1750 (1982). ISSN 00323861.

[6] A. V. Dobrynin, R. H. Colby & M. Rubinstein; "Scaling Theory of Polyelectrolyte Solutions"; Macromolecules **28**, pp. 1859–1871 (1995). ISSN 0024-9297, 1520-5835. 11, 12, 14, 28, 44

[7] P.-G. de Gennes; *Scaling Concepts in Polymer Physics* (Cornell University Press) (1979); ISBN 0-8014-1203-X. 11

[8] R. M. Fuoss & U. P. Strauss; "Electrostatic Interaction of Polyelectrolytes and Simple Electrolytes"; Journal of Polymer Science **3**, pp. 602–603 (1948). ISSN 00223832, 15426238. 12

[9] M. Rubinstein, R. H. Colby & A. V. Dobrynin; "Dynamics of Semidilute Polyelectrolyte Solutions"; Physical Review Letters **73**, pp. 2776–2779 (1994). ISSN 0031-9007. 12, 13

[10] C. G. Lopez, R. H. Colby, P. Graham & J. T. Cabral; "Viscosity and Scaling of Semiflexible Polyelectrolyte NaCMC in Aqueous Salt Solutions"; Macromolecules **50**, pp. 332–338 (2017). ISSN 0024-9297, 1520-5835. 12, 28, 29

[11] S. Dou & R. H. Colby; "Charge Density Effects in Salt-Free Polyelectrolyte Solution Rheology"; Journal of Polymer Science Part B: Polymer Physics **44**, pp. 2001–2013 (2006). ISSN 0887-6266, 1099-0488. 13, 28

[12] N. B. Wyatt & M. W. Liberatore; "Rheology and Viscosity Scaling of the Polyelectrolyte Xanthan Gum"; Journal of Applied Polymer Science **114**, pp. 4076–4084 (2009). ISSN 00218995, 10974628. 13

[13] R. Fournier; *Polymères associatifs par interaction covalente réversible diol-acide boronique*; Ph.D. thesis; Université Pierre et Marie Curie (2016). 13

[14] F. G. Donnan & E. A. Guggenheim; "Die genaue Thermodynamik der Membrangleichgewichte"; Zeitschrift für Physikalische Chemie **162A** (1932). ISSN 2196-7156, 0942-9352. 14

[15] A. S. Michaels; "Aggregation of Suspensions by Polyelectrolytes"; Industrial & Engineering Chemistry **46**, pp. 1485–1490 (1954). ISSN 0019-7866, 1541-5724. 15

[16] J. F. Joanny, L. Leibler & P. G. De Gennes; "Effects of Polymer Solutions on Colloid Stability"; Journal of Polymer Science: Polymer Physics Edition **17**, pp. 1073–1084 (1979). ISSN 00981273, 15429385. 15

[17] D. Lootens; *Ciments et Suspensions Concentrées Modèles. Ecoulement, Encombrement et Floculation*; Ph.D. thesis; Université Paris VI (2004). 15, 35

[18] F. Oosawa, S. Asakura, K. Hotta, N. Imai & T. Ooi; "G-F Transformation of Actin as a Fibrous Condensation"; Journal of Polymer Science **37**, pp. 323–336 (1959). ISSN 00223832, 15426238. 15

[19] A. L. Ogden & J. A. Lewis; "Effect of Nonadsorbed Polymer on the Stability of Weakly Flocculated Suspensions"; Langmuir **12**, pp. 3413–3424 (1996). ISSN 0743-7463, 1520-5827. 15

[20] R. Hogg; "Bridging Flocculation by Polymers"; KONA Powder and Particle Journal **30**, pp. 3–14 (2013). ISSN 0288-4534. 15

[21] I. Szilagyi, G. Trefalt, A. Tiraferri, P. Maroni & M. Borkovec; "Polyelectrolyte Adsorption, Interparticle Forces, and Colloidal Aggregation"; Soft Matter **10**, p. 2479 (2014). ISSN 1744-683X, 1744-6848.

[22] J. A. Lewis, H. Matsuyama, G. Kirby, S. Morissette & J. F. Young; "Polyelectrolyte Effects on the Rheological Properties of Concentrated Cement Suspensions"; Journal of the American Ceramic Society **83**, pp. 1905–1913 (2000). ISSN 00027820, 15512916. 15

[23] T. B. J. Blijdenstein, E. van der Linden, T. van Vliet & G. A. van Aken; "Scaling Behavior of Delayed Demixing, Rheology, and Microstructure of Emulsions Flocculated by Depletion and Bridging"; Langmuir **20**, pp. 11321–11328 (2004). ISSN 0743-7463, 1520-5827. 16, 17, 33

[24] C. Zhao, G. Yuan, D. Jia & C. C. Han; "Macrogel Induced by Microgel: Bridging and Depletion Mechanisms"; Soft Matter **8**, p. 7036 (2012). ISSN 1744-683X, 1744-6848. 16

[25] Y. Otsubo; "Comparison of Rheological Behavior of Suspensions Flocculated by Polymer Bridging and Depletion"; The Society of Rheology **23**, pp. 75–80 (1995). 17, 33

[26] R. Vedula & H. Spencer; "Adsorption of Poly(Acrylic Acid) on Titania (Anatase) and Zirconia Colloids"; Colloids and Surfaces **58**, pp. 99–110 (1991). ISSN 01666622. 17

[27] H. G. Pedersen & L. Bergström; "Forces Measured between Zirconia Surfaces in Poly(Acrylic Acid) Solutions"; Journal of the American Ceramic Society **82**, pp. 1137–1145 (1999). ISSN 00027820, 15512916. 17

[28] H. Grasdalen; "High-Field, 1H-n.m.r. Spectroscopy of Alginate: Sequential Structure and Linkage Conformations"; Carbohydrate Research **118**, pp. 255–260 (1983). ISSN 00086215. 19

[29] M. Fertah, A. Belfkira, E. montassir Dahmane, M. Taourirte & F. Brouillette; "Extraction and Characterization of Sodium Alginate from Moroccan Laminaria Digitata Brown Seaweed"; Arabian Journal of Chemistry **10**, pp. S3707–S3714 (2017). ISSN 18785352. 20

[30] T. A. Fenoradosoa, G. Ali, C. Delattre, C. Laroche, E. Petit, A. Wadouachi & P. Michaud; "Extraction and Characterization of an Alginate from the Brown Seaweed Sargassum Turbinarioides Grunow"; Journal of Applied Phycology **22**, pp. 131–137 (2010). ISSN 0921-8971, 1573-5176. 20

[31] H. K. Holme, K. Lindmo, A. Kristiansen & O. Smidsrød; "Thermal Depolymerization of Alginate in the Solid State"; Carbohydrate Polymers **54**, pp. 431–438 (2003). ISSN 01448617. 20

[32] K. F. Tjipangandjara & P. Somasundaran; "Effects of Changes in Adsorbed Polyacrylic Acid Conformation on Alumina Flocculation"; Colloids and Surfaces **55**, pp. 245–255 (1991). ISSN 01666622. 23

[33] H. G. Pedersen & L. Bergström; "Stabilizing Ceramic Suspensions Using Anionic Polyelectrolytes: Adsorption Kinetics and Interparticle Forces"; Acta Materialia **48**, pp. 4563–4570 (2000). ISSN 13596454. 23, 24

[34] M. Wiśniewska; "Study of the Influence of Temperature and the Ionic Strength of the Solution on the Adsorption and Conformation of Poly(Acrylic Acid) Macromolecules on the ZrO2 Surface"; Adsorption Science & Technology **24**, pp. 673–686 (2006). ISSN 0263-6174, 2048-4038. 24

[35] S. Biggs & T. W. Healy; "Electrosteric Stabilisation of Colloidal Zirconia with Low-Molecular-Weight Polyacrylic Acid. An Atomic Force Microscopy Study"; Journal of the Chemical Society, Faraday Transactions **90**, pp. 3415–3421 (1994). ISSN 0956-5000, 1364-5455. 24

[36] K. I. Draget, G. Skjåk-Bræk & O. Smidsrød; "Alginate Based New Materials"; International Journal of Biological Macromolecules **21**, pp. 47–55 (1997). ISSN 01418130. 40

[37] A. Blandino, M. Macías & D. Cantero; "Formation of Calcium Alginate Gel Capsules: Influence of Sodium Alginate and CaCl2 Concentration on Gelation Kinetics"; Journal of Bioscience and Bioengineering **88**, pp. 686–689 (1999). ISSN 13891723.

[38] S. Boninsegna, R. D. Toso, R. D. Monte & G. Carturan; "Alginate Microspheres Loaded with Animal Cells and Coated by a Siliceous Layer"; Journal of Sol-Gel Science and Technology **26**, pp. 1151–1157 (2003).

[39] K. Y. Lee & D. J. Mooney; "Alginate: Properties and Biomedical Applications"; Progress in Polymer Science **37**, pp. 106–126 (2012). ISSN 00796700.

[40] B.-B. Lee, P. Ravindra & E.-S. Chan; "Size and Shape of Calcium Alginate Beads Produced by Extrusion Dripping"; Chemical Engineering & Technology pp. n/a–n/a (2013). ISSN 09307516. 85

[41] E.-S. Chan, B.-B. Lee, P. Ravindra & D. Poncelet; "Prediction Models for Shape and Size of Ca-Alginate Macrobeads Produced through Extrusion–Dripping Method"; Journal of Colloid and Interface Science **338**, pp. 63–72 (2009). ISSN 00219797.

[42] E.-S. Chan, T.-K. Lim, W.-P. Voo, R. Pogaku, B. T. Tey & Z. Zhang; "Effect of Formulation of Alginate Beads on Their Mechanical Behavior and Stiffness"; Particuology **9**, pp. 228–234 (2011). ISSN 16742001. 58, 65

[43] U. Prüsse; "Bead Production with JetCutting and Rotating Disk/Nozzle Technologies"; Landbauforschung Völkenrode p. 11 (2002).

[44] U. Prüsse, L. Bilancetti, M. Bučko, B. Bugarski, J. Bukowski, P. Gemeiner, D. Lewińska, V. Manojlovic, B. Massart, C. Nastruzzi, V. Nedovic, D. Poncelet, S. Siebenhaar, L. Tobler, A. Tosi, A. Vikartovská & K.-D. Vorlop; "Comparison of Different Technologies for Alginate Beads Production"; Chemical Papers **62** (2008). ISSN 1336-9075.

[45] N. Bremond, E. Santanach-Carreras, L.-Y. Chu & J. Bibette; "Formation of Liquid-Core Capsules Having a Thin Hydrogel Membrane: Liquid Pearls"; Soft Matter **6**, p. 2484 (2010). ISSN 1744-683X, 1744-6848.

[46] L. Rolland, E. Santanach-Carreras, T. Delmas, J. Bibette & N. Bremond; "Physicochemical Properties of Aqueous Core Hydrogel Capsules"; Soft Matter **10**, pp. 9668–9674 (2014). ISSN 1744-683X, 1744-6848. 131

[47] I. Meiser, S. C. Müller, F. Ehrhart, S. G. Shirley & H. Zimmermann; "A New Validation Method for Clinical Grade Micro-Encapsulation: Quantitative High Speed Video Analysis of Alginate Capsule"; Microsystem Technologies **21**, pp. 75–84 (2015). ISSN 0946-7076, 1432-1858. 40

[48] G. T. Grant, E. R. Morris, D. A. Rees, P. J. Smith & D. Thom; "Biological Interactions between Polysaccharides and Divalent Cations: The Egg-Box Model"; FEBS Letters **32**, pp. 195–198 (1973). ISSN 00145793. 40

[49] O. Smidsrød & A. Haug; "Dependence upon the Gel-Sol State of the Ion-Exchange Properties of Alginates"; Acta Chemica Scandinavica **26**, pp. 2063–2074 (1972). 40

[50] C. J. Brinker & G. W. Scherer; *Sol-Gel Science: The Physics and Chemistry of Sol-Gel Processing* (Academic Press, Inc., San Diego, CA 92101) (1990); ISBN 0-12-134970-5. 41, 48

[51] K. I. Draget, O. Gaserød, I. Aune, P. O. Andersen, B. Storbakken, B. T. Stokke & O. Smidsrød; "Effects of Molecular Weight and Elastic Segment Flexibility on Syneresis in Ca-Alginate Gels"; Food Hydrocolloids p. 6 (2001). 41, 42, 43, 48, 51, 53

[52] D. E. Dunstan, R. Salvatore, M. Jonsson & M.-L. Liao; "Syneresis of K-Carrageenan Gels at Different KCI and LBG Concentrations"; in "Gums and Stabilisers for the Food Industry," pp. 137–147 (Elsevier) (2000); ISBN 978-1-85573-788-4. 41, 42

[53] V. Palluault; *Nouveaux Traitements de Surface Respecueux de l'environnement Par Des Gels Polymères Réticulables*; Ph.D. thesis; Université de Bordeaux I (2010). 42, 43, 48

[54] K. I. Draget, K. Østgaard & O. Smidsrød; "Homogeneous Alginate Gels: A Technical Approach"; Carbohydrate Polymers **14**, pp. 159–178 (1991). ISSN 01448617. 42, 43

[55] A. Martinsen, G. Skjåk-Braek & O. Smidsrød; "Alginate as Immobilization Material: Correlation between Chemical and Physical Properties of Alginate Gel Beads"; Biotechnology and Bioengineering **33**, pp. 79–89 (1989). ISSN 00063592. 43

[56] G. SkjLk-Brek, H. Grasdalen & O. Smidsrod; "Lnhomogeneous Polysaccharide Ionic Gels"; p. 24. 43

[57] L. Rolland; *Propriétés physico-chimiques de capsules d'hydrogel à coeur liquide*; Ph.D. thesis; Université Pierre et Marie Curie (2013). 44

[58] O. Bonhomme; *Etude de La Formation de Fibres En Microfluidique : Compétition Entre Mise En Forme et Gélification de Fluides Complexes Sous Écoulement*; Ph.D. thesis; Université de Bordeaux I (2011). 55

[59] C. Ouwerx, N. Velings, M. Mestdagh & M. Axelos; "Physico-Chemical Properties and Rheology of Alginate Gel Beads Formed with Various Divalent Cations"; Polymer Gels and Networks **6**, pp. 393–408 (1998). ISSN 09667822. 58, 63, 64

[60] C. Wang, C. Cowen, Z. Zhang & C. Thomas; "High-Speed Compression of Single Alginate Microspheres"; Chemical Engineering Science **60**, pp. 6649–6657 (2005). ISSN 00092509. 59, 60

[61] Y. Yan, Z. Zhang, J. R. Stokes, Q.-Z. Zhou, G.-H. Ma & M. J. Adams; "Mechanical Characterization of Agarose Micro-Particles with a Narrow Size Distribution"; Powder Technology **192**, pp. 122–130 (2009). ISSN 00325910. 58

[62] M. Ø. Olderøy, M. Xie, J.-P. Andreassen, B. L. Strand, Z. Zhang & P. Sikorski; "Viscoelastic Properties of Mineralized Alginate Hydrogel Beads"; Journal of Materials Science: Materials in Medicine **23**, pp. 1619–1627 (2012). ISSN 0957-4530, 1573-4838. 58, 61

[63] M. Mancini, M. Moresi & R. Rancini; "Mechanical Properties of Alginate Gels: Empirical Characterisation"; Journal of Food Engineering **39**, pp. 369–378 (1999). ISSN 02608774. 59

[64] E. T. Severs & J. M. Austin; "Flow Properties of Vinyl Chloride Resin Plastisols"; INDUSTRIAL AND ENGINEERING CHEMISTRY **46**, p. 7 (1954). 72

[65] D. C. Vadillo, A. Soucemarianadin, C. Delattre & D. C. D. Roux; "Dynamic Contact Angle Effects onto the Maximum Drop Impact Spreading on Solid Surfaces"; Physics of Fluids **21**, p. 122002 (2009). ISSN 1070-6631, 1089-7666. 76, 77, 85, 94

[66] S. Chandra & C. T. Avedisian; "On the Collision of a Droplet with a Solid Surface"; Proceedings of the Royal Society A: Mathematical, Physical and Engineering Sciences **432**, pp. 13–41 (1991). ISSN 1364-5021, 1471-2946.

[67] C. Clanet, C. BéGuin, D. Richard & D. QuéRé; "Maximal Deformation of an Impacting Drop"; Journal of Fluid Mechanics **517**, pp. 199–208 (2004). ISSN 0022-1120, 1469-7645. 77, 78

[68] C. Josserand & S. Thoroddsen; "Drop Impact on a Solid Surface"; Annual Review of Fluid Mechanics **48**, pp. 365–391 (2016). ISSN 0066-4189, 1545-4479.

[69] J. Eggers, M. A. Fontelos, C. Josserand & S. Zaleski; "Drop Dynamics after Impact on a Solid Wall: Theory and Simulations"; Physics of Fluids **22**, p. 062101 (2010). ISSN 1070-6631, 1089-7666. 77

[70] J. Cooper White, R. Crooks & D. Boger; "A Drop Impact Study of Worm-like Viscoelastic Surfactant Solutions"; Colloids and Surfaces A: Physicochemical and Engineering Aspects **210**, pp. 105–123 (2002). ISSN 09277757. 78

[71] D. Bartolo, A. Boudaoud, G. Narcy & D. Bonn; "Dynamics of Non-Newtonian Droplets"; Physical Review Letters **99** (2007). ISSN 0031-9007, 1079-7114. 78

[72] L.-H. Luu & Y. Forterre; "Drop Impact of Yield-Stress Fluids"; Journal of Fluid Mechanics **632**, p. 301 (2009). ISSN 0022-1120, 1469-7645. 78, 80, 87, 88, 89

[73] B. Ray, G. Biswas & A. Sharma; "Regimes during Liquid Drop Impact on a Liquid Pool"; Journal of Fluid Mechanics **768**, pp. 492–523 (2015). ISSN 0022-1120, 1469-7645. 80

[74] S. Pregent, S. Adams, M. F. Butler & T. A. Waigh; "The Impact and Deformation of a Viscoelastic Drop at the Air–Liquid Interface"; Journal of Colloid and Interface Science **331**, pp. 163–173 (2009). ISSN 00219797. 80

[75] T. T. Truscott, B. P. Epps & A. H. Techet; "Unsteady Forces on Spheres during Free-Surface Water Entry"; Journal of Fluid Mechanics **704**, pp. 173–210 (2012). ISSN 0022-1120, 1469-7645. 80

[76] R. C. Hurd, J. Belden, M. A. Jandron, D. Tate Fanning, A. F. Bower & T. T. Truscott; "Water Entry of Deformable Spheres"; Journal of Fluid Mechanics **824**, pp. 912–930 (2017). ISSN 0022-1120, 1469-7645. 80

[77] M. Jalaal, D. Kemper & D. Lohse; "Viscoplastic Water Entry"; Journal of Fluid Mechanics **864**, pp. 596–613 (2019). ISSN 0022-1120, 1469-7645. 80, 81

[78] T. Watanabe; "Deformation and Solidification of a Droplet on a Cold Substrate"; Chemical Engineering Science **47**, p. 7 (1992). 81, 82

[79] R. Bhola & S. Chandra; "Parameters Controlling Solidification of Molten Wax Droplets Falling on a Solid Surface"; Journal of Materials Science p. 12 (1999). 81

[80] R. de Ruiter, P. Colinet, P. Brunet, J. H. Snoeijer & H. Gelderblom; "Contact Line Arrest in Solidifying Spreading Drops"; Physical Review Fluids **2** (2017). ISSN 2469-990X. 82, 86

[81] R. de Ruiter, L. Royon, J. H. Snoeijer & P. Brunet; "Drop Spreading and Gelation of Thermoresponsive Polymers"; Soft Matter **14**, pp. 3096–3104 (2018). ISSN 1744-683X, 1744-6848. 82

[82] V. Thiévenaz, T. Séon & C. Josserand; "Solidification Dynamics of an Impacted Drop"; Journal of Fluid Mechanics **874**, pp. 756–773 (2019). ISSN 0022-1120, 1469-7645. 82

[83] T. Coupez & E. Hachem; "Solution of High-Reynolds Incompressible Flow with Stabilized Finite Element and Adaptive Anisotropic Meshing"; Computer Methods in Applied Mechanics and Engineering **267**, pp. 65–85 (2013). ISSN 00457825. 92

[84] E. Hachem, M. Khalloufi, J. Bruchon, R. Valette & Y. Mesri; "Unified Adaptive Variational MultiScale Method for Two Phase Compressible–Incompressible Flows"; Computer Methods in Applied Mechanics and Engineering **308**, pp. 238–255 (2016). ISSN 00457825. 92

[85] S. V. Shepel & B. L. Smith; "On Surface Tension Modelling Using the Level Set Method"; International Journal for Numerical Methods in Fluids **59**, pp. 147–171 (2009). ISSN 02712091, 10970363. 92

[86] P. Scholz, D. Froelich & R. Muller; "Viscoelastic Properties and Morphology of Two-Phase Polypropylene/Polyamide 6 Blends in the Melt. Interpretation of Results with an Emulsion Model"; Journal of Rheology **33**, pp. 481–499 (1989). ISSN 0148-6055, 1520-8516. 102

[87] A. Cohen & C. J. Carriere; "Analysis of a Retraction Mechanism for Imbedded Polymeric Fibers"; Rheologica Acta **28**, pp. 223–232 (1989).

[88] I. Sigillo, L. di Santo, S. Guido & N. Grizzuti; "Comparative Measurements of Interfacial Tension in a Model Polymer Blend"; Polymer Engineering & Science **37**, pp. 1540–1549 (1997). ISSN 0032-3888, 1548-2634.

[89] S. Kitade, A. Ichikawa, N. Imura, Y. Takahashi & I. Noda; "Rheological Properties and Domain Structures of Immiscible Polymer Blends under Steady and Oscillatory Shear Flows"; Journal of Rheology **41**, pp. 1039–1060 (1997). ISSN 0148-6055, 1520-8516.

[90] H. Yamane, M. Takahashi, R. Hayashi, K. Okamoto, H. Kashihara & T. Masuda; "Observation of Deformation and Recovery of Poly(Isobutylene) Droplet in a Poly(Isobutylene)/Poly(Dimethyl Siloxane) Blend after Application of Step Shear Strain"; Journal of Rheology **42**, pp. 567–580 (1998). ISSN 0148-6055, 1520-8516.

[91] K. Okamoto, M. Takahashi, H. Yamane, H. Kashihara, H. Watanabe & T. Masuda; "Shape Recovery of a Dispersed Droplet Phase and Stress Relaxation after Application of Step Shear Strains in a Polystyrene/Polycarbonate Blend Melt"; Journal of Rheology **43**, pp. 951–965 (1999). ISSN 0148-6055, 1520-8516. 102

[92] J. F. Palierne; "Linear Rheology of Viscoelastic Emulsions with Interfacial Tension"; Rheologica Acta **29**, pp. 204–214 (1990). ISSN 0035-4511, 1435-1528. 102

[93] S. Assighaou & L. Benyahia; "Universal Retraction Process of a Droplet Shape after a Large Strain Jump"; Physical Review E **77** (2008). ISSN 1539-3755, 1550-2376. 102, 122

[94] W. Yu, M. Bousmina & C. Zhou; "Determination of Interfacial Tension by the Retraction Method of Highly Deformed Drop"; Rheologica Acta **43** (2004). ISSN 0035-4511, 1435-1528. 102

RÉSUMÉ

Faire tomber des gouttes de solution d'alginate dans un bain d'ions calcium est une technique robuste pour produire des billes gélifiées, dont les applications fleurissent dans de nombreux domaines. Ce procédé de dripping repose sur la réticulation électrostatique des chaînes d'alginate par les ions calcium, donnant naissance à un gel physique rigide. Les nombres de Reynolds et de Weber, caractérisant la compétition entre les forces d'inertie, de dissipation visqueuse et de tension de surface, sont connus pour influencer la forme finale des billes. En effet, l'énergie cinétique tend à favoriser l'étalement des gouttes à l'impact, alors que la viscosité et la tension de surface de la goutte tendent à limiter cette déformation. Cependant, il y a très peu d'étude sur la dynamique de déformation de gouttes impactant un bain liquide. Dans ces travaux, nous utilisons une caméra rapide afin d'étudier l'évolution de la forme de gouttes de suspensions alginate-céramique impactant un bain d'ions calcium. Nous observons tout d'abord que la goutte s'étale à l'impact, puis relaxe vers une forme plus sphérique au fur et à mesure de sa gélification dans le bain. Comme attendu, l'élongation maximale des gouttes est d'autant plus grande que la vitesse d'impact est importante et que la viscosité de la goutte est faible. L'effet de la concentration en calcium dans le bain est moins intuitive. Lorsque celle-ci augmente, la déformation maximale de la goutte à l'impact décroît et sa relaxation vers une forme sphérique est plus rapide. Nous montrons que la gélification de la goutte s'accompagne d'un phénomène de synérèse : la surface extérieure de la goutte commence à gélifier et se contracte en expulsant de l'eau. Par conséquent, cette membrane de gel est sous tension élastique, ce qui entraîne la relaxation de la capsule. Nous identifions également les freins de cette relaxation, expliquant pourquoi les billes s'arrêtent de relaxer avant d'atteindre la sphère parfaite et avant d'être totalement gélifiée.

MOTS CLÉS

goutte, encapsulation, gel, fluide complexe, rhéologie, impact

ABSTRACT

Dripping alginate solutions into a bath of calcium ions is a robust process to obtain gelled beads which can be used in various applications. This process relies on the ability of calcium ions to bridge the alginate chains of the droplets to form a rigid gel. The Reynolds and Weber numbers, defining the competition between inertia, viscous dissipation and surface tension forces are known to influence the final shape of the beads. Indeed inertia tends to drive the spreading of droplets upon impact with the bath while high droplet viscosity and surface tension tend to limit their extension upon impact. However, very little is known about the dynamics of the droplets shape during impact with a liquid bath. In this thesis, using a high speed camera, we study the shape evolution of alginate-ceramic suspension droplets as they impact and penetrate a bath of calcium ions. We observe that the drops first extend upon impact with the liquid surface, and then relax to a more spherical shape inside the bath, while gelling at the same time. As expected, the drops maximum elongation increases with increasing impact velocity and decreasing droplet viscosity. The effect of the calcium concentration in the bath is less intuitive. As it increases, the maximum extension of the droplets tends to decrease and the droplets tend to relax faster to a spherical shape. This relaxation is related to a syneresis phenomenon which instantaneously occurs as the droplet hits the bath: the gelled membrane in formation tends to shrink by expelling water. This phenomenon puts the outer membrane under tensile stress and therefore is the driving force of the capsule relaxation. We evidence the main obstacles to relaxation, resulting in capsules frozen in an ellipsoidal shape before reaching a perfect sphere and before being fully gelled.

KEYWORDS

drop, encapsulation, gel, complex fluid, rheology, impact